UNIVERSITÀ DEGLI STUDI DI TORINO
Department of Physics

Dottorato di Ricerca in Scienza della
Natura e Tecnologie Innovative
Indirizzo di Fisica ed Astrofisica

Cycle: XXXIII

Development of a novel solid state detector for beam monitoring in proton therapy

Doctoral Candidate:
Zahra Shakarami

Supervisor:
Prof. Roberto Sacchi

External Reviewer:
Prof. Maria Giuseppina Bisogni
Prof. Luigi Rigon

Coordinator:
Prof. Paolo Gambino

Academic years: 2018 - 2020

Università degli Studi di Torino
Scuola di Dottorato in Scienza ed Alta Tecnologia

Tesi di Dottorato di Ricerca in Scienza ed Alta Tecnologia
Indirizzo di Fisica ed Astrofisica
XXXIII Ciclo

Development of a novel solid state detector for beam monitoring in proton therapy

Zahra Shakarami

Supervisor:
Prof. Roberto Sacchi

External reviewers:
Prof. Maria Giuseppina Bisogni
Prof. Luigi Rigon

Coordinator of the Ph.D. Program:
Prof. Paolo Gambino

Academic years: 2018-2020

Acknowledgments

It has been a great honor to spend several years in the Department of Physics at the University of Torino and INFN (National Institute for Nuclear Physics, Turin Division) especially within the MoVeIT project, and its members will always remain dear to me.

I would like to express my gratitude to my experienced caring supervisor, Prof. Roberto Sacchi, who has supported me during these three years with his immense knowledge, patience, and motivation.

Prof. Roberto Cirio, an amazing director and a wise headman of the Torino group, is especially acknowledged. He has given me the opportunity to have a new interesting scientific experience in Italy, who has been supporting me and gave me a lot of valuable suggestions and motivations within these years.

My sincere thanks also go to Prof. Vincenzo Monaco, Prof. Felix Mas Milian, Dr. Anna Vignati, Dr. Simona Giordanengo, and Dr. Federico Fausti, for keeping me on track and for always being there whenever I needed your help, for allowing me to learn so much and giving me opportunities truly incredible. You have been like a second family to me, words cannot express how grateful I am.

I also would like to express my special appreciation to the UFSD group of INFN Torino, and the staff of CNAO, TIFPA, and FBK. It was a great pleasure collaborating with them. Thanks for helping and accessing their laboratories and facilities.

I would like to thank my Ph.D. committee members, Prof. Maria Giuseppina Bisogni and Prof. Luigi Rigon for their time, consideration and advice.

I am truly grateful to my lovely caring parents whose continuous uncountable sacrifices, encouragements, and supports were an unremitting source of inspiration for me. I don't know if I would be able to thank you for any words, for your true love and advice. Your prayer for me was what sustained me thus far...

To my amiable husband, Maziar, for his unquestioning support, patience, and love. You taught me there is more to life than what I feel. Thank you so much!

Thank you, my God, for everything you have made to happen in my life and for always leading me towards my best. Thank you for giving me the chance and strength to make my and my parent's dream come true.

Abstract

Proton therapy is a very attractive and promising modality in cancer treatment that relies on the depth dose distribution property known as Bragg peak. This localized and better-controlled dose distribution in comparison to X-rays, improves the therapeutic ratio while sparing the healthy tissue surrounding the tumors. The beam energy is one of the key parameters in proton therapy that defines the depth inside the patient (up to 30 cm) at which the radiation is deposited with the required clinical range accuracy of 1 mm. Range deviations alter the dose distribution, leading to under-dosage of the distal edge of the tumor or normal structure over-dosage. The beam range verification is mainly performed by measuring the integrated depth-dose profiles in water phantoms and using multi layers ionization chambers and just in the routine quality control checks.

This thesis is focused on the development and the use of the Ultra-Fast Silicon Detector (UFSD), chosen as innovative proton beam monitor. UFSDs are thin silicon sensors based on the Low Gain Avalanche Diode technology (LGAD), which should overcome the limitations of ionization chambers. They can be used for the energy check during the irradiation, and for the development of new beam monitors for future delivery schemes employing fast energy modulation systems. The prototype consists of two thin UFSDs, aligned along the clinical proton beam direction in a telescope configuration that allows to measure the time-of-flight (TOF) of proton to determine the beam energy.

It should be noticed that part of the content of this thesis is object of the Italian Patent Application No. 102021000025190 field on 2021/09/30. The first chapter provides an introduction to hadrontherapy and to the main features of such facilities. In particular, the ionization chamber as the current particle beam monitor is discussed. The second chapter describes the basic properties of silicon devices and UFSD. Moreover, the structure details of different UFSD prototypes are explained. An overview of the laboratory setups used in this thesis and the methodologies of measurement used for the UFSDs characterization are discussed in chapter three. Chapter four describes experimental measurement performed in Italian hadron therapy facilities and explains TOF and energy measurement procedures. Chapter five contains a description of the computational tool to reconstruct and analyze the wave forms acquired during the experimental measurements. Chapter six describes the simulation studies to evaluate systematic effects to optimize the TOF and energy measurement accuracy. In addition, two system calibration methods and their characteristics are introduced. Finally in the last chapter, the measured proton beam energies using TOF technique after implementing the calibration methods are presented. Furthermore, the deviation between nominal and measured energies in terms of range in water and the accuracy required for the clinical application is studied.

Contents

List of Figures

List of Tables

Chapter 1

Charged particles therapy

"X rays will prove to be a hoax."

William Thomson, The Lord Kelvin

1.1 A general overview of Medical Physics

The important effects of the concepts of the exact sciences on medicine occurred during the 17th century. Since that time, the interactions of physics and medicine were developed and it was possible for an educated person to have sufficient knowledge to make contribution in both fields. The study and use of ionizing radiation in medicine started with three important discoveries (Figure 1.1): (1) X-rays by Wilhelm Conrad Roentgen in 1895. (2) Natural radioactivity by Henri Becquerel in 1896. (3) Radium-226 by Pierre and Marie Curie in 1898. After the mentioned discoveries, atomic and nuclear physics appeared and developed. Since no person could have sufficient knowledge in both fields of medicine and nuclear physics, some physicists appeared in medical fields mainly in order to solve problems involved in medical applications of ionizing radiations. Physicists were employed as hospital physicists after the introduction of the use of radionuclides for both diagnostic purposes and for therapy.
As a consequence introducing ^{60}Co-therapy technique, accelerators, advanced nuclear medicine techniques for the improvement of radio therapeutic and medical imaging equipment, radiation dosimetry and health care, the number of hospital physicists increased rapidly. Nowadays, Medical Physics is a well established discipline covering the application of physics concepts to medicine and the medical physicist covers extensive areas

such as radiology, radiation therapy and also non-ionizing (ultrasound, ultraviolet, radio frequency and laser) radiation. During the last 20 years, physicists gave an valuable contribution in almost all field of medicine. By making use of the new computational techniques and of the high technology equipment into medicine, the role and responsibility of physicists in hospital developed increasingly becoming more and more significant in the diagnosis and treatment of diseases. At this moment, considering employment situation and working fields, two categories are identified for medical physicist. The first group are working as teachers and scientists in universities, as researchers in industrial laboratories/companies. The second one consist of medical physicists involved in a clinical environment, either employed in hospitals or as consultants to hospitals.
There are lot of international, national, regional, sub-regional organizations for medical physicists all over the world. Many journals such as Medical Physics, Physics in Medicine and Biology, Physica Medica and etc. publish Medical Physics researches in different field. Work of medical physicists directly or indirectly affects patient safety and well-being. Therefore, standards for education and professional activity are set and maintained by various professional and governmental bodies through educational accreditation and professional certification [1, 2].

Fig. 1.1: *Three important discoveries in radiation. Pictures taken from [3–5].*

With this overview, let me point out that this dissertation has been defined and implemented in the field of Medical Physics in order to improving the accuracy of proton therapy.

This chapter will outline basics of physics in the radiotherapy techniques and introduce the particle therapy. A short overview of basic principals of physical and biological aspects of charged particles therapy will be presented.

1.2 Brief history of hadrontherapy

Radiation therapy or radiotherapy is widely used among the treatment options for cancer. Radiotherapy uses high doses of ionizing radiation, generally as part of cancer treatment course to control or kill malignant cells. To prevent tumor recurrence after surgery, it may also be used as part of adjuvant therapy.
Radiation therapy is synergistic with chemotherapy, and can be used before, during, and after chemotherapy in susceptible cancers. Radiation therapy is commonly applied to the cancerous tumor because of its ability to control cell growth.
Ionizing radiation works by damaging the DNA of cancerous tissue leading to cellular death. The main goal of radiation therapy is to deliver radiation dose to target tumor while sparing the normal tissues surrounding the tumors.
When the irradiating beams are made of charged particles (protons and other ions, such as carbon, helium, neon, or silicon), radiation therapy is called hadrontherapy. In the following, heavy particle therapy term will be used as synonymous of hadrontherapy. At present only protons and carbon ions are in clinical use.
Robert R. Wilson in 1946 described some ions properties and for the first time proposed the possibility to implement ion therapy in medicine [6]. In 1954 the first patient was treated with a proton beam at Berkeley Radiation Laboratory (California). The list of particle therapy facilities in operation is available in reference [7].
The main advantage of particle therapy compared to photon and electron is the profile of depth-dose distribution. Ions have a narrow peak of the deposited dose at the end of their range, the so-call Bragg peak after William Henry Bragg who discovered it in 1903 [8], which position in the target volume depends on the particle beam energy. Based on the data collected by the Particle Therapy Co-Operative Group (PTCOG), the total number of treated patients worldwide with accelerated ions, as of 2018 was 221528. More details about the number of facilities and treated patients can be found in [9].

1.3 Interactions of heavy charged particles with matter

1.3.1 Mechanism of formation of the Bragg peak

Fast charged particles interact with the electrons and nuclei of the medium in different ways, in which the ionization of the medium is by far the dominant effect.

The energy loss for ionization in matter per unit length is expressed as $-\frac{dE}{dx}\,[\frac{MeV}{cm}]$, called stopping power. It is the basic physical quantity that determines the dose that the particle delivers in the medium. Stopping Power is described by the following Bethe-Bloch equation [10]:

$$S = -\frac{dE}{dx} = \frac{4\pi N_A}{m_e c^2}\frac{z^2}{\beta^2}\frac{Z}{A}\rho \ln\frac{2m_e c^2\beta^2\gamma^2}{I} - \text{relativistic term} \tag{1.1}$$

Where:

- $\beta = \frac{v}{c}$, v is the velocity of the particle and c the speed of light;
- N_A, is the Avogadro number;
- z is the particle charge in units of e;
- m_e is the rest mass of the electron;
- Z, A, ρ and I are the atomic number, the mass number, the density and the mean excitation energy of the medium.

As x increases, the energy decreases, thus the $\frac{dE}{dx}$ is negative. $\frac{S}{\rho}$ is defined as mass stopping power, which contains the density of the matter.

$$\frac{S}{\rho} = -\frac{1}{\rho}\frac{dE}{dx}[\frac{MeV.cm^2}{g}] \tag{1.2}$$

According to the Bethe-Bloch equation, energy lost by charged particles is inversely proportional to the square of their velocity and this explains the peak occurring just before the particle comes to a complete stop [11].

Equation 1.1 leads to a divergence as the particle velocity tends to zero. However, at very low energies comparable to the velocity of the orbital electron in the materials, there is a high probability that the projectile picks up these electrons. Therefore, the charge changes and Z has been replaced by z_{eff} (the effective projectile charge) which is sketched by the Barkas formula [12]:

$$z_{eff} = Z\left(1 - e^{-125\beta Z^{\frac{2}{3}}}\right) \tag{1.3}$$

Considering the Equ. 1.1, at not relativistic energies, as the kinetic energy of the projectile decreases along the penetration depth, the energy loss rate grows up, in particular in the last few millimeters of the particle path where it shows a much steeper rise. Finally, at the end of the path the stopping power drops because of the rapid reduction of the effective charge (z_{eff}) to very low energy values. Indeed, more energy per unit length will be deposited towards the end of its path rather than at its beginning. This effect can be expressed in the term of the relative dose (see the dose definition in section 1.4.)

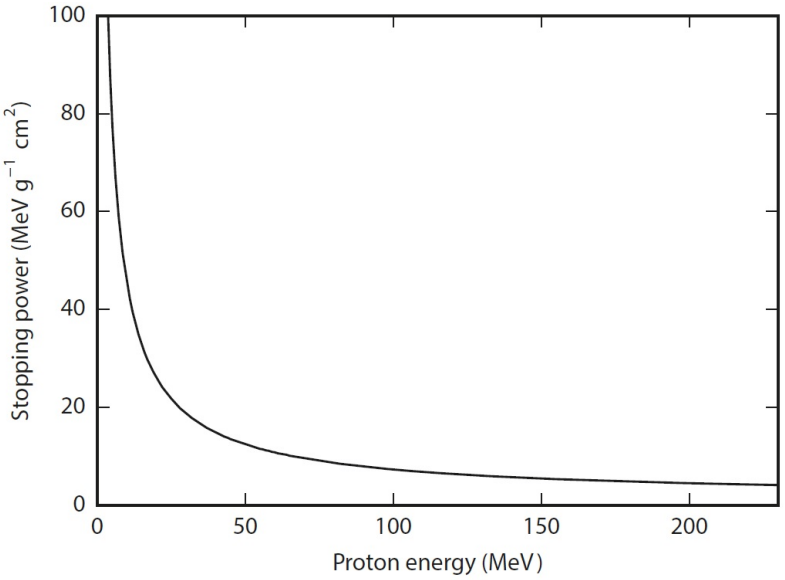

Fig. 1.2: *The stopping power of the proton in water as a function of the clinical energy range. Pictures taken from [13].*

The stopping power of protons in water in therapeutic energy range is plotted in Fig. 1.2. The stopping power increases as the charged particle's energy decreases. This cause to occurs a peak immediately before the particles come to rest.

Figure 1.3 depicts the energy losses for different types of radiation as a function of the penetration depth in water (density is similar to human body tissues). There is a build-up at the photon entrance then photons release their energy to the medium exponentially with depth, which leads to an undefined range. On the contrary, for a charged particle like proton or carbon ion, its maximum is located at the end of the track causing the Bragg peak so most of the energy is deposited near the end of the trajectory. At the very end, however, it begins to pick up electrons and the dE/dx drops [12], [14].

According to Fig. 1.3 some of the important features of the Bragg peak are [8],[15]:

- Due to the mass of carbon ion (12 times greater than proton) the Bragg peak of carbon ions is much sharper than proton peak;
- The depth in water of the Bragg peak increases with the energy of the particle;
- Another effect that varies approximately inverse to the square root of the mass is the lateral dose fall-off (called also penumbra), which depends on the multiple elastic Coulomb scattering the particle suffers as it transverses the medium; whereas the distal fall-off depends on the inelastic scattering between the particle and electrons and nuclei constituting the absorbing material.

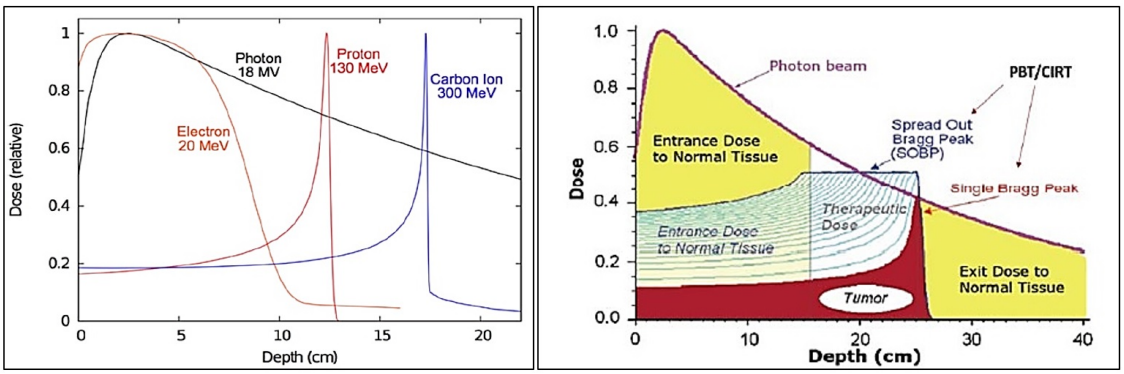

Fig. 1.3: *(Left)The depth dose distribution of Electron, Photon, Proton and Carbon ions in water. Proton and Carbon ions deposit most of their energy at specific depth that depends on their energy (Bragg peak). Photons and electrons reach the maximum dose distribution rapidly (build-up) and then decrease exponentially. (Right) Therapeutic dose delivers at the specific depth by proton and photons [16].*

In addition, the carbon ions curve in Fig. 1.3 (left) shows a tail after the Bragg peak due to carbon fragments originated by nuclear interactions with the target nuclei.

1.3.2 Dose and Linear Energy Transfer (LET)

The amount of energy which is deposited in a medium by ionizing radiation expressed per mass unit of the medium is called absorbed dose and is expressed in gray (Gy):

$$D = \frac{dE}{dm}(1\frac{J}{kg} = 1Gy) \tag{1.4}$$

Radiation dosimetry and radiobiological modeling deal with the deposited dose by the energy released along the path of the individual charged particles. A quantity of particular importance is the Linear Energy Transfer or LET.

Based on ICRU 16, the LET is a deposited energy per unit length which is closely related to the stopping power defined earlier, but the stopping power does not include the nuclear interactions. Moreover, interactions that produce delta rays with energies larger than a given threshold are sometimes excluded from the LET definition, especially when only the energy transferred in the vicinity of the primary particle is to be considered; in this case the quantity is called restricted LET.

The LET is related to the radiation quality [17] and since it strongly influences the RBE (see the RBE definition in section 1.8.) of ion beams, is a useful quantity in radiobiology. For charged particles, the LET increases when:

- the particle velocity decreases ($LET \sim \frac{1}{v^2}$),
- the particle charge increases ($LET \sim z_{eff}^2$), where z_{eff} is the effective particle charge.

The $LET(\frac{keV}{\mu m})$ is related with the dose by the following relation:

$$Dose(Gy) = 1.6 \times 10^{-19} LET \frac{F}{\rho} \tag{1.5}$$

where F is the fluence ($\frac{particles}{cm^2}$) and ρ is the density of the medium ($\frac{g}{cm^3}$).

1.3.3 Spread Out Bragg Peak

As mentioned in section 1.2, a pristine Bragg peak is rather narrow and in order to cover the volume of the tumor in depth it must be spread out. The Spread Out Bragg Peak (SOBP) is obtained by a superimposition of many pristine Bragg peaks of different ranges and energies, as shown in Fig. 1.3. The depth of the pristine Bragg peaks can be changed step by step by changing the beam energy produced in accelerators, or by inserting material in the beam path (degrader). Independently of the degrading technique used, the dose carried by each individual Bragg peak must be such that a flat SOBP is produced. The dose (D) at each depth (z_i) is a weighted (w_j) sum of the dose contributions d_i of n beams with

different energies and, thus, different peak position Z_i [8]:

$$D(z_i) = \sum_{j=1}^{n} w_j d_j(Z_i) \tag{1.6}$$

1.4 Radiobiology of charged particles

1.4.1 DNA damages

Radiation effects on biological structures at cell nucleus level are mainly attributed to DNA damages. The DNA with around 10 μm in diameter makes up roughly 5% of the cell nucleus volume. Radiations yield DNA single strand breaks and double strand breaks, where in particular, double strand breaks are considered lethal events leading to cell inactivation [18].
Two main effects can induce damage to the DNA: 1) direct; the radiation interacts directly with the DNA, ionizing and exciting its atoms (ions). 2) indirect; the DNA breaks are due to free radical produced by the incident particle in the cell environment (photon irradiations). The dose distribution of the ions in a track depends on the distance, r, from the particle trajectory [19],[20] following $1/r^2$ law.

Protons, neutrons, and even more carbon ions are considered as high-LET radiations while photons, gamma-rays, and electrons are low-LET radiations. Fig 1.4 shows the simulation of the same dose distribution delivered by low and high-LET particles in a cell, where the small circles represent biological targets and the dots represent ionizations produced along the tracks by electrons set in motion by photons or protons set in motion by neutrons. When a sensitive structure is crossed by a high LET particle track (protons), regardless of position in the cell cycle, degree of oxygenation or the repair capacity of the cell, there is a larger probability of cell death [21].

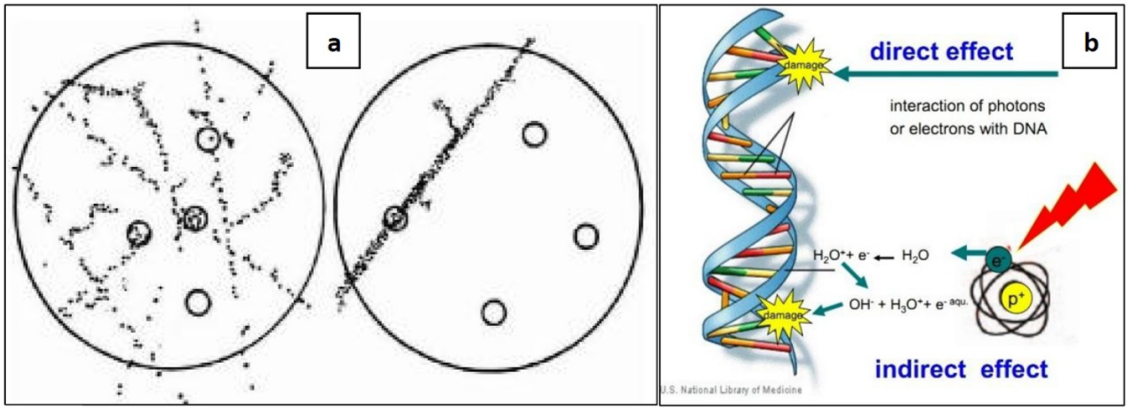

Fig. 1.4: *(a) Ionization density from photon-like low-LET particles (left) and neutron-like high- LET corresponding to the same dose particles [21]; (b) Direct and indirect effects of radiation on DNA [22].*

Since human tissue consist largely of water, the bulk of the ionization produced by irradiation occurs in water molecules and a lot of free radicals OH- are produced, which is also related to the presence of oxygen in the medium. Thus hypoxic cells are about three times more radio resistant than oxygenated cells [21]. The dose ratio between hypoxic and aerobic cells yielding the same biological effect is defined by Oxygen Enhanced Ratio (OER):

$$OER = \frac{D_{Hypoxic}}{D_{aerobic}} \tag{1.7}$$

The high LET particles indicate the advantage of a reduced OER [19].

1.4.2 Relative Biological Effectiveness (RBE)

Based on ICRU (1990) and ICRU (1997), the Relative Biological Effectiveness (RBE) is the ratio of biological effectiveness of a type of ionizing radiation (reference radiation) relative to another, given the same amount of absorbed energy. The RBE is an empirical value depending on the type of ionizing radiation, the energies involved, the biological endpoint being considered such as cell death, and the oxygen tension of the tissues or so-called oxygen effect, which is defined as follows:

$$RBE = \frac{D_x}{D_{particle}} \tag{1.8}$$

Traditionally, the gamma ($^{60}Co \sim 1.2MeV$) and X-rays (200 kV) have been considered as the reference radiation [8].
To convert a physical dose (D) into a dose that describes the biological effect, the Biological

Effectiveness Dose (BED) is defined follows:

$$BED = RBE \times D \tag{1.9}$$

The RBE of protons is typically about 1.1, which means that for a given physical dose their biological effect is not largely different than the effect of photons. This differs from the larger RBE of other heavier particles, for instance carbon ions (RBE $\sim$ 2.5) or neutrons (RBE $\sim$ 10 to 20) [21].

The RBE is shown in Fig.1.5 as a function of the LET for different types of particles. It is noteworthy to remark that the highest RBE is observed for protons and the RBE decreases with increasing particle atomic number. In the case of protons, the maximum RBE (LET more or less 25 $keV/\mu m$) is much localized in the distal part of the Bragg peak and the overall RBE of a treatment is lower than with heavier ions. For carbon and other ions with the extremely narrow Bragg peak, the high rate of energy loss towards the end of the particle range results in a dramatic increase of the LET.

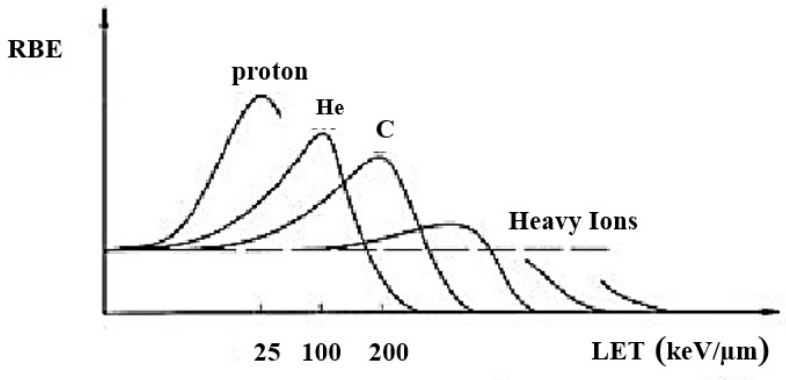

Fig. 1.5: *Comparison of RBE values for various ions as a function of LET [23].*

There is evidence of slight increase of proton RBE values which varies with depth, in parallel there are too many uncertainties such as different tissue, dose per fraction or proton energy that the RBE is typically assumed as a constant. In case of heavier ions, since the RBE increases gradually with increasing LET from the plateau to the Bragg peak region, thus the RBE variation has to be taken into account all along the ion path [19]. Fig. 1.6 illustrates current biological modeling of the RBE applied to proton and carbon ions. For carbon ions the RBE is 2.1 in the plateau region, while its values vary between 2.7 and 3.4 in the SOBP region, with a maximum RBE value in the distal part. As a

consequence, to produce a homogeneous biological-equivalent dose in the target, the physical dose calculated in the SOBP should not be flat, but decreasing with increasing depth. The biological dose for protons is 1.1 times the physical one (Equ.1.9) as shown in Fig. 1.6.

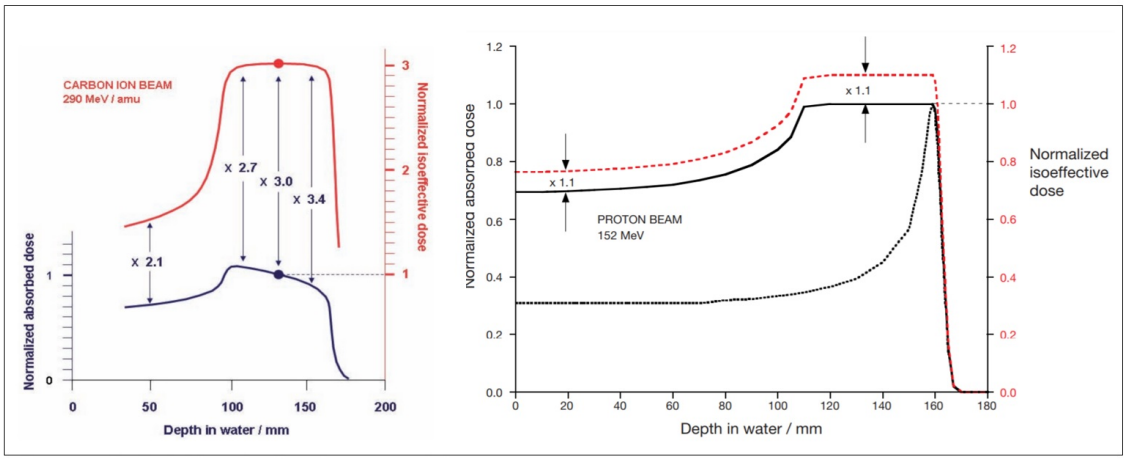

Fig. 1.6: *Biological dose modelling for carbon ions (left) and proton (right) [21].*

1.5 Hadrontherapy facilities

There are three main equipment components in a hadron therapy facility: (1) particle accelerator with energy selection system, (2) beam transport system and (3) beam delivery system.

To distribute the dose in depth an accelerator is used to increase the charged particle energy to the clinically used values (70 to 250 MeV for protons and 120 to 400 MeV/u for carbon ions). The beam energy produced by the accelerator must be sufficient to reach the deepest tumors. Cyclotrons and synchrotrons are the accelerators currently used in proton therapy and only synchrotrons are available to accelerate carbon ions in clinics. The choice of accelerator type depends on several aspects such as treatment method, price, local conditions, available expertise and available space. Notice that, with both machines, good clinical results are obtained.

The main duty of beam delivery system is to spread the beam in lateral and longitudinal directions, using passive or dynamic (active) methods. A brief description of these parts is presented in the following.

1.6 Basic physics of charged particles accelerator

The physical process involved in accelerator and beam transport design is described by the Lorentz force law:

$$\vec{F} = q(\vec{E} + \vec{v} \times \vec{B}) \tag{1.10}$$

The electric field E can be used to increase the energy of the particle of charge q, and the magnetic field B to modify the trajectory.

In case of an electric field, the force is in the direction of the electric field. Therefore, the charged particle is accelerated in its direction of motion (v), and the particle energy increases when E is in the same direction of v.

In the case of a magnetic field, the force is perpendicular to both directions of the magnetic field and the velocity. This force does not accelerate the particle in this direction, but adds a force transverse to the initial direction, which bends the particle's path without changing the its energy. If a particle with a unit charge and momentum p (in GeV/c) is bent in a magnetic field B (in kilogauss) a radius of curvature of ρ (in meter) is determined by:

$$B(kG)\rho(m) = 33.356p(GeV/c) \tag{1.11}$$

The technology of delivering a charged particle with the appropriate energy to a patient, involves accelerating the particles, bending and focusing the beam of particles in the direction of the target in the patient [8]. A collection of particles within a small range of position, angle and velocity is defined as a beam [24].

1.6.1 Cyclotron

The cyclotron is a compact accelerator that delivers a high intensity, continuous beam of constant energy. Since the energy is fixed, to set the beam energy to the desired value the degrader is required. Figure (1.7) shows the scheme of a cyclotron with the following major components:

- a proton source located into the center of the cyclotron, in which hydrogen gas is ionized and from which the protons are extracted;

- a radio frequency (RF) system to provide strong electric field consisting of two or four electrodes (often called “Dee”) which are connected to an RF generator;
- a strong magnet that limits the particle trajectories into a spiral-shaped orbit allowing them to be accelerated repeatedly by the RF voltage [11];
- an extraction system which guides the particles that have reached the maximum energy from the cyclotron into a beam transport system.

The beam is injected into the center of the cyclotron and accelerated each time when it crosses the electric field. A radio-frequency alternating voltage applied across the gap between the two “dees” -shaped cavities- alternately attracts and repels charged particles.

When the proton beam leaves the electric field region (the gap between dees), and enters to the magnetic field region (dees) is bent 180 degrees and reenters the electric field region at the correct time to be accelerated in the opposite direction. Thus, the particles are accelerated going from one dee to the another and they do not experience any electric field so long as inside dees. When the beam reaches the gap , the polarity of the electric field is reversed at the exact time to ensure acceleration. At the end of acceleration, the particle reaches the outer radius and is extracted from the cyclotron and directed to the treatment room.
The RF system ensures the synchronization of the electric field with the path of the charged particle at the angular frequency ω of the electric field defined by the cyclotron equation:

$$\omega = qB/m \tag{1.12}$$

where q and m are the charge and mass of the particle, and B is the magnetic field of the cyclotron magnet.

A limitation in the design of a cyclotron is related to the size and weight of the magnet which scales with the strength of the magnetic field. Accelerators based on superconducting magnets partially overcome the problem by enabling higher magnetic fields and thus a smaller size. The cyclotrons for hadrontherapy with relatively few adjustable parameters produce a beam with a uniform intensity and fixed energy value. The relative simplicity and the limited dimensions of the cyclotron compared to a synchrotron, make it the preferred choice for proton facilities. The availability of single extraction energy is the main drawback in a cyclotron.

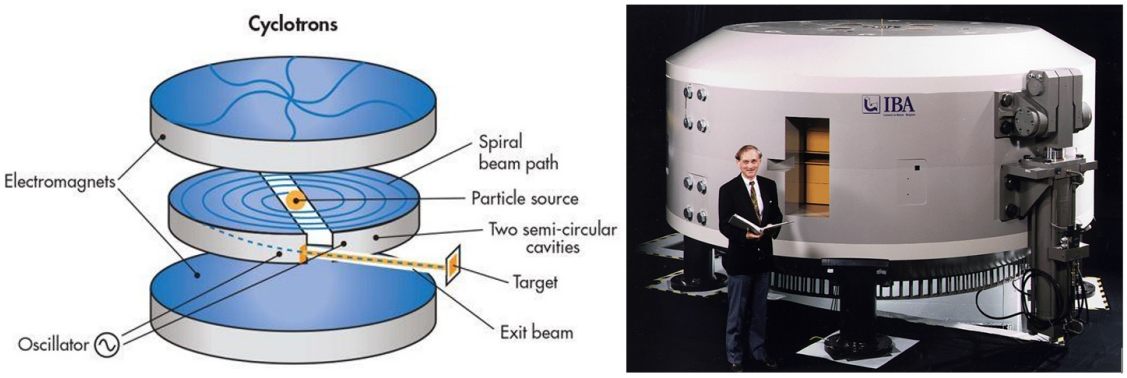

Fig. 1.7: *Diagram of the beam trajectory and structure of cyclotron on the left side, and a clinical cyclotron in the right side [25], [26].*

1.6.2 Synchrotron

The synchrotron is a circular accelerator, in which the accelerating particle beam travels around a fixed closed-loop path. In contrast to the cyclotron, which uses a constant magnetic field and an electric field with a constant frequency, in the synchrotron both the magnetic field and electric field frequency are increased synchronously with the energy of the circulating particles. This enables to accelerate particles while keeping their path inside a circular ring. The synchrotron allows the particles to be accelerated up to the desired energy before extraction occurs, without any loss of intensity. The charged particle path in a synchrotron is shown in Fig 1.8.

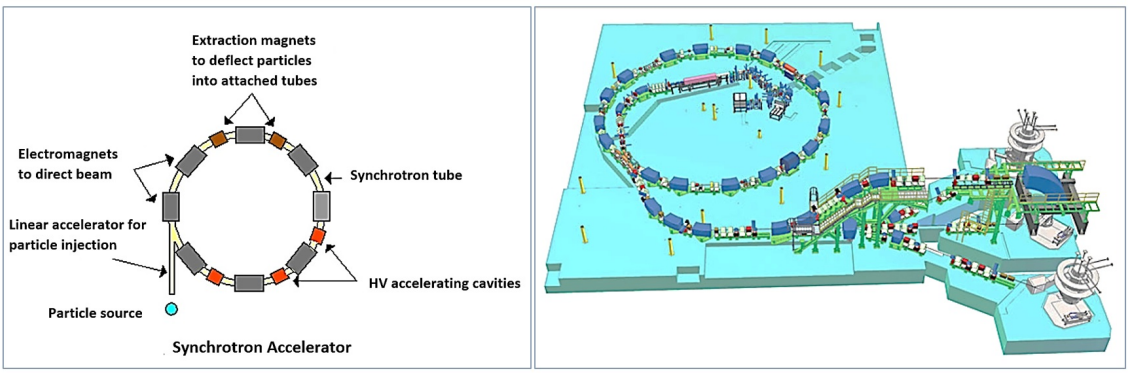

Fig. 1.8: *Layout of a synchrotron showing the simplified operation, the beam trajectory and structure of a synchrotron accelerator on the left side, and technical drawing of the CNAO clinical synchrotron in the right side. The sources, the lines of pre-acceleration and injection are located inside the ring [27], [28].*

The acceleration procedure of a synchrotron occurs in cycles which called "spills", and each spill includes the following steps:

- a bunch of particles is injected in the main ring of the synchrotron. These particles are produced by a source and pre-accelerated to few MeV using a linac;
- the beam circulates in the ring frequently through the accelerating structure until obtaining the desired energy, typically between 70-250 MeV for protons;
- a beam extraction follows, which should be as slow as possible for accurate dose applications. The required extraction time is typically 0.5 to 5 seconds which depends on the extracted beam intensity (see Fig.1.9. left). Schematically, the slow extracted beam would look like Fig. 1.9 right;
- going back to the initial situation, eventually with deceleration and dumping unextracted particles.

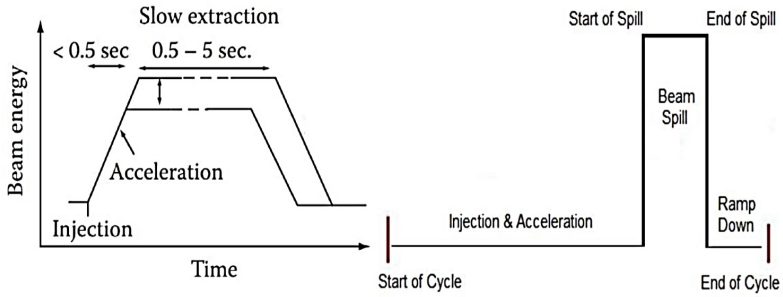

Fig. 1.9: *Typical spill from a synchrotron. Left: The injected particles are accelerated to the desired energy and slowly extracted; Right: Time structure of the beam delivery in one spill.*

A synchrotron generates pulsed beams with variable energies. The energy of the extracted beam can be varied from one cycle to the next in steps of a few MeV.

1.7 Treatment Planning System

The Treatment Planning System (TPS) is a software that helps the radiologist to simulate the dose distribution in the patient and to find the optimal beam configuration to achieve clinical dose prescriptions (Fig. 1.10). TPSs are the heart of radiotherapy systems and

the key to improved patient outcomes. Once image data sets, provided by computed tomography (CT), are loaded and the tumors identified together with the delineation of the target and surrounding organs, the beam configuration and the prescription of the desired effect, the systems develops a complex plan for each beam path as to how the therapy system will deliver the radiation. The software also calculates the expected dose distribution in the patient's tissue, including variables such as the penetration depth of the energy level into the tissue, which is influenced by the type of tissue that the beam lines hit (e.g. bone or lung vs. muscle).

Based on this information and prescriptions for the desired dose at the target site and the maximum tolerated dose to other organs, it performs a minimization procedure (called "inverse planning") to determine the treatment parameters. The TPS task is completed when it has found the set of radiation intensities, energies and directions required to best fulfill the prescription.

The TPS looks for the solution in an iterative manner: Starting from an initial hypothesis about the radiation intensities, the program calculates the particles spectra for each point of interest and estimates the corresponding biological effect; if the result is in accordance with the prescription, the TPS can stop the execution and return the information about the prescribed beams to the physician; otherwise, the program must vary the radiation intensities accordingly and repeat the evaluation of the biological effect until the specifications are met or the maximum number of iterations is reached.

These treatment plans can also be modified to compensate for the reduction in tumor size as treatments progress.

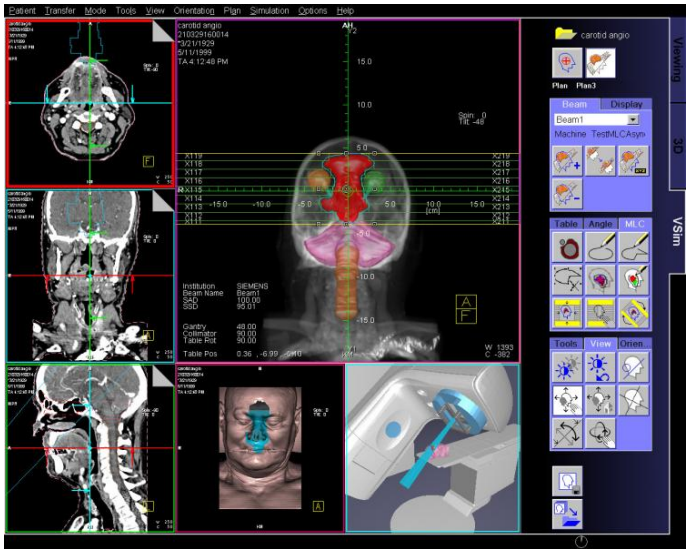

Fig. 1.10: *Treatment Planning System (TPS) software interface [29].*

1.8 Beam Delivery Techniques

The Beam Delivery System (BDS) is the last part of the radiation therapy machine before the tumor being irradiated. This part is used to control the beam conditions and to assure that the dose distribution follows the prescription. The beam exiting from the accelerator is well described by a 2D Gaussian function calculated as a function of particle type, energy, depth and type of material traversed by the vacuum exit window. The transverse and longitudinal initial dimensions have a typical FWHM (Full Width at Half Maximum) of less than 10 mm, which is certainly smaller than the size of a typical tumor, which can normally vary between 1 and 20 cm.
In principle, the narrow, pristine beam extracted from the accelerator (the so-called pencil beam) with a fixed energy and direction cannot cover the irregular shape of the tumor volume without adjustments.
There are two classes of techniques used to adjust the beam conditions and to correctly distribute the dose to the tumor volume after prescription of the TPS 'scattering technique' and 'scanning technique'.

1.8.1 The passive scattering technique

The first class of dose distribution methods uses passive elements to spread out the original beam, which consists of absorbers, collimators and range modulators, to generate the correct SOBP and adapt the dose distribution to the lateral portion of the tumors (Fig. 1.11).
In the scattering method, the beam is passed through one or more scattering foils of material with a high atomic number Z. The beam diameter is increased to match to the maximum lateral tumor cross section by sending the beam through this scattering system followed by a patient specific collimator. The disadvantage of passive delivery techniques are the need for patient-specific elements and the generation of secondary particles in the nuclear interactions of the beam with the passive elements.

1.8.2 The active beam delivery technique

Active beam delivery or dynamic beam scanning [30] is a method of achieving the desired dose distribution by moving the beam laterally over the target using magnets while dynamically varying the energy of the beam to change the penetration depth.
In the scanning method whole the tumor cross section is 'actively' scanned by a pencil

beam of less than 1 cm in cross section. This scanning is done in steps and the applied 'spot' dose is varied per step ('spot scanning'), whereas, if it is performed by continuously shifting the beam along lines in the tumour, during which the beam intensity is varied to deliver the correct dose along the line ('continuous scanning') (Fig. 1.11).

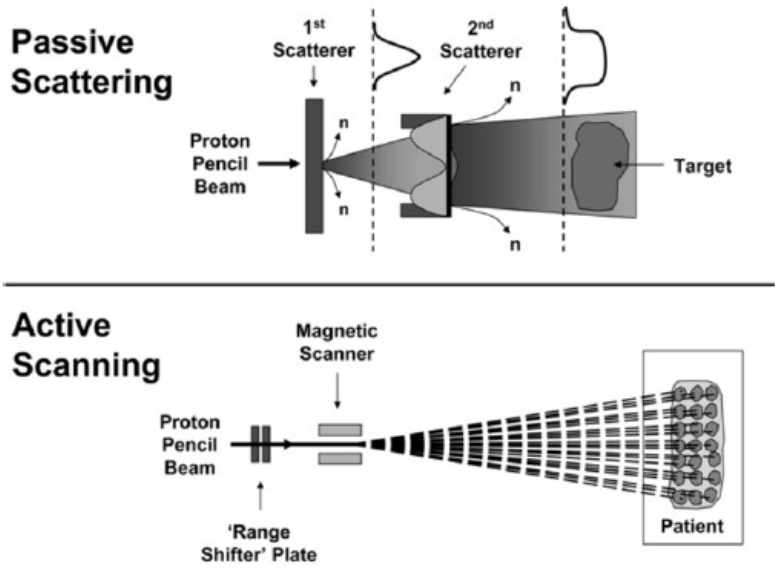

Fig. 1.11: *Passive scattering versus pencil beam (active) scanning [31].*

An example of active system is depicted in Fig. 1.12.The volume to be irradiated is divided into several layers called slices. Each slice is covered by a grid of individual elements called voxels or spots. Each spot is characterized by the coordinates in the transverse plane, fixed depth (corresponding to the single energy) and number of particles. Each slice is irradiated with a fixed energy beam, which is moved in a transverse direction by a pair of scanning magnets to apply the required dose to each spot on the slice. These parameters were determined before starting the irradiation by a TPS to achieve the desired dose distribution [32].
The main task of the BDS is to deliver the dose according to the prescription given by the TPS, in the form of a map of the dose to be delivered in each region of the target.

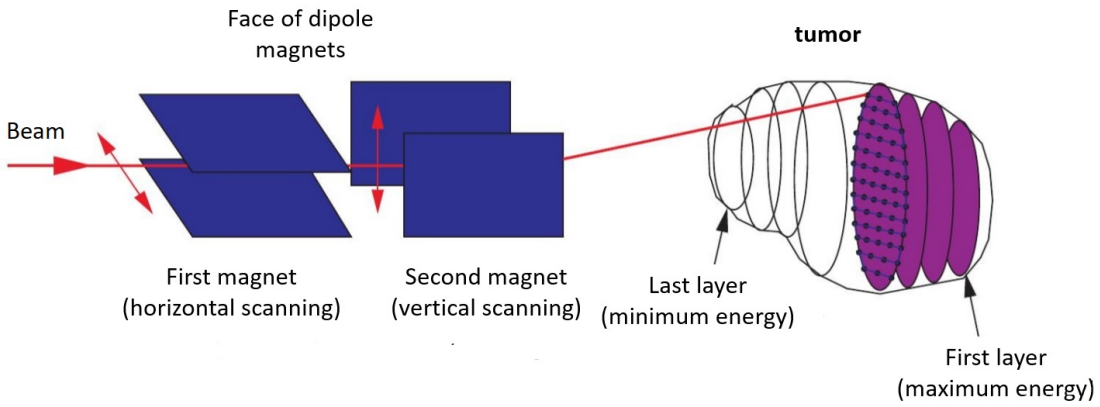

Fig. 1.12: *Scheme of an active scanning: the tumor volume is divided in slices, and each isoenergetic slice is covered by a grid of spots. During irradiation the beam is guided by a pair of scanning magnet in the horizontal and vertical directions and the beam range is adjusted by changing the beam energy through the accelerator [33].*

The process of changing energy is achieved with different methods. In the case of a synchrotron, an energy change between two accelerator spills can be achieved, whereas in a cyclotron-based machine an absorber for energy degradation followed by an energy selection system must be used [8].
The beam is moved from one spot to the next, using a pair of magnets positioned perpendicular to each other and to the beam direction and driven by fast power supplies. The particle fluence for each spot is measured and the beam is switched to the next spot when the intensity for one position has reached the expected values.

The advantages of the active beam delivery technique can only be achieved by positioning the pencil beam and precisely monitoring the number of particles delivered to each point using a fast and accurate monitoring system that is fully integrated into the beam delivery system.

The disadvantage of such a beam delivery system is its greater operational complexity due to the management of the scanning magnets and the control of the beam position. Moreover, the tumor position must be known with high precision (of the order of 1 mm) in order to achieve the required precision in the dose shaping process. The problems occur especially when the tumor moves due to the patient's breathing and heartbeats. Nowadays both of these dose delivery methods are used in the clinic [11, 8, 34–37].

1.9 Dose Delivery System

The accuracy of the dose distribution achieved with the pencil beam scanning technique is based on a precise online measurement of the beam position and the number of particles delivered to each spot. The dose delivery system (DDS) must control the scanning system located at the end of the extraction line, which consists of two power supplies connected to two identical dipole magnets for horizontal and vertical beam deflection.
Once the required number of particles is delivered to one spot, the DDS has to change the magnetic currents to move the beam to the next spot. In addition, the DDS has to be interfaced to the accelerator controller such that after completion one iso-energetic slice, the beam quickly is stopped and a new energy value required for the treatment of next slice is provided.

1.9.1 The particle beam monitors

The accurate and reliable beam monitoring is crucial to deliver the dose as prescribed and to make it possible to meet the requirements of the treatment plan. This leads to development of specific, precise and reliable detector for beam monitoring [38–40].

The most commonly used beam monitoring detectors are based on gas-filled ionization chambers (ICs). For example, Figure 1.13 shows the monitoring system of CNAO [42], which consists of five parallel nitrogen-filled ionization chambers mounted at the nozzle at the end of the beam line, about 0.5 m from the isocenter. The number of delivered particles, the beam transversal position and dimension can be measured by using these five parallel plate ionization chambers. This monitor chambers are included in two independent steel boxes: BOX1 and BOX2 (Fig. 1.13 a and b). The main characteristics of ionization chambers are briefly described below:

- 2 Integral chambers (INT1 and INT2) to measure the beam flux at high rate read out (1 MHz) with great accuracy and stability; the anodes are made by a kapton foil covered by a thin aluminum layer and the sensitive area is $24 \times 24\ cm^2$; for safety reason one of the two particle measurements is redundant ;
- 2 strip segmented chambers to measure the beam position with a precision of 100 μm every 100 μs through the evaluation of the center of gravity. Their anodes are

made by kapton foils covered by 128 aluminum strips (1.55 mm wide and pitch 1.65 mm); the difference between the horizontal (Strip Y) and the vertical (Strip X) strip chambers is the strip arrangement (90 degree rotation to each other). The two chambers can also be used to measure the number of particles integrating the counts of all the strips;

- A pixel ionization chamber (PX) as redundant detector allows for an independent measurement of the beam position and dimension with a accuracy of 200 μm. The anode is segmented in 1024 pixels (32×32 pixels). Each pixel has a pitch of 6.6 mm and the total sensitive area of the monitor is $21.1 \times 21.1 cm^2$.

The high voltage (HV) for the nitrogen gas-filled ICs is set at 400 V and the gap between the electrodes is 5 mm. The total water equivalent thickness of these chambers is measured by beam irradiation to be approximately 0.9 mm. The intermediate material budget by the beam detector is distributed over a length of about 20 cm and is the main contributor for the lateral beam dispersion. To minimize the effect, the boxes are installed approximately 70 cm from the patient entrance [44, 45].

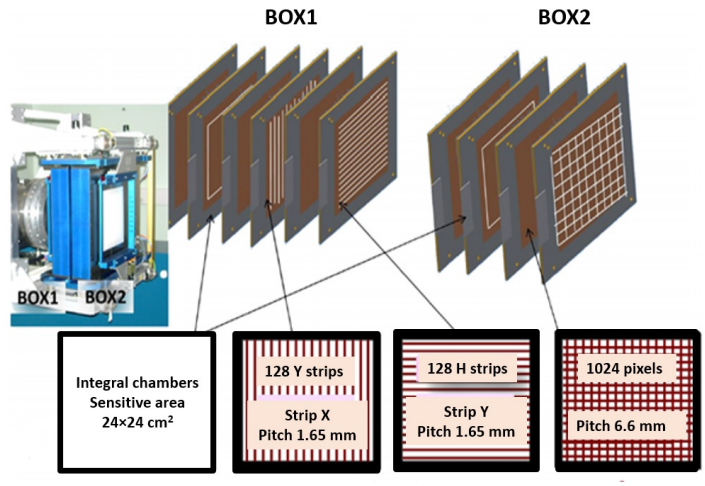

(a)

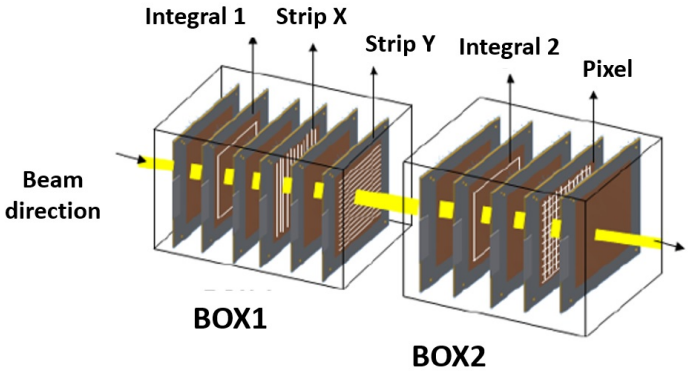

(b)

Fig. 1.13: (a) The components of the ionization chambers of the dose delivery system. (b) Detail of the electrode segmentation for beam detectors (BOX1 and BOX2). Pictures taken from [42–44].

1.9.2 Advantages and drawbacks of ionization chambers

There are several advantages for the ICs due to their limited complexity such as robustness , simple design and operation, and limited material budget (less than 1 mm water equivalent thickness). In addition, the ICs have not shown any signs of performance degradation due to radiation and aging effects even after several years of irradiation.

Nevertheless, ICs suffer from several limitations. Gas-filled detectors measure the charge generated in the gas, which depends not only on the number of particles, but also on the particle energy and the environmental parameters. In order to determine the number of particles which are delivered to any given point, the relevant information on which the

dose depends should be known. The beam energy must be known in advance and the effect of temperature and pressure dependencies must be corrected. Periodic calibration procedures are required to take these effects into account and to guarantee the reliability of the ICs in clinical practice.

Another limitation of ionization chambers is their limited sensitivity. Due to the low ionization charge production in gases, the minimum number of particles that an IC can detect is limited to the order of a few thousands. In addition, the charge collection time is relatively long (in the order of hundreds of microseconds), so that their response is quite slow.

These two limitations of ICs prevent their use in treatment modalities where a limited number of particles must be delivered to each spot, or where fast position changes are required.

Fast treatment modalities are required to treat moving organs with the so called "re-scanning technique", where the dose painting is repeated several times with reduced doses, to mitigate the interaction effects due to the combination of patient movements and beam position changes.

In the future, advanced irradiation modalities are required to be more accurate, faster and more sensitive. For instance, adaptive radiotherapy, 4-D treatments based on the tracking of the tumor position by following its changes with a movable beam, is already used in clinic with dedicated linear accelerator such as Cyberknife and Vero Sterotactic Body Radiotherapy [46]. The extension of such delivery modalities in charged particle therapy requires novel developments, particularly in faster scanning magnets, and more precise monitoring detectors with improved speed, sensitivity and spatial resolution.

In general, the fast beam delivery strategies have shown the trend to improve accuracy, shorten treatment times and increase the patient throughput for the future radiotherapy approaches.

We will describe in the following section how the limitations of gas-filled detectors could be overcome by a new type of monitoring devices based on solid state detectors.

1.10 Aim of thesis

The limitations of gas-filled detectors as monitoring devices in charged particle therapy such as limited sensitivity, dependence of the measurable number of particles on the beam energy and environmental parameters, the poor position resolution and slow response times were discussed in the previous section. To overcome these limitations, a new approach for the beam monitoring is required.

As mentioned earlier, the aim of either classical X-ray radiotherapy or advanced hadron therapy, exploiting protons or heavy ions, is to deliver the prescribed dose of radiation to the malignant tumor cells, while minimizing the side effects in the normal tissues. Technological development such as proton therapy enable to deliver the radiation dose better conformed to the tumor and thereby improve the treatment outcome. The great potential of the proton beam is depicted in Figure 1.3.

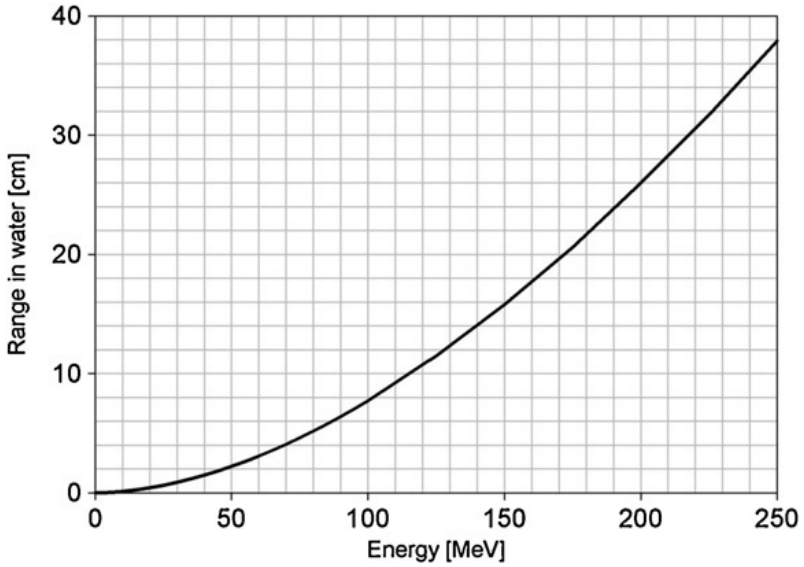

Fig. 1.14: *Range of a proton beam in water based on the continuous slowing down approximation as a function of proton energy [47].*

Beam energy is a key parameter in particle therapy, defining the depth inside the patient at which the therapeutic radiation is deposited (range).Figure 1.14 shows the range of monoenergetic proton beams in water. The range can be retrieved from the PSTAR table (National Institute of Standards and Technology)[48] or with the Bragg-Kleeman rule [49], as:

$$R = N.E^{\beta}[cm] \tag{1.13}$$

with N, proportionality factor [g/cm^2 MeV] that is approximately proportional to the square root of the effective atomic mass of the medium $\sqrt{A_{eff}}$, and β, an exponent factor of the kinetic energy (E), dimensionless. The values of N and β defined by the International Commission on Radiation Units and Measurements (ICRU), respectively equal to: 0.0023 g/cm^2 MeV and 1.75 [50]. With an undershoot of the proton range the distal edge of the tumor will not receive the intended dose (Figure 1.15). Clinically, the acceptable uncertainty in the measured range is 1 *mm* in water.

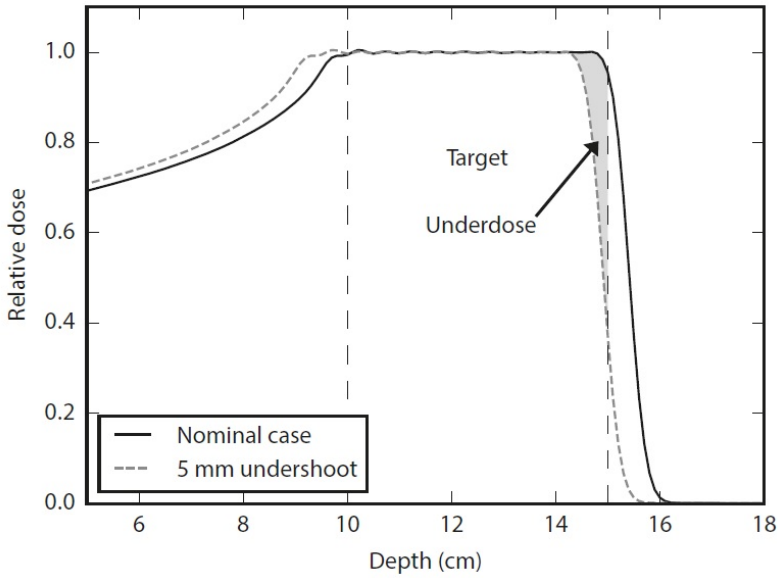

Fig. 1.15: *The effect of a range uncertainty on the depth-dose distribution of a therapeutic proton beam. This case was designed to deliver the maximum dose at a depth of 10 cm to 15 cm [13].*

In this thesis the new proton beam monitor based on solid state detector is studied. In particular, segmented silicon detectors are considered as an alternative to ICs to monitor the therapeutic proton beam. The use of silicon detectors to measure the energy of therapeutic proton beam with high accuracy (less than 1 mm range in water), in a wide range of beam energies (typically between 60 and 250 MeV) and at high fluxes (the therapeutic flux ranges from 10^8 to 10^{10} p/cm^2·s) is investigated.

The energy of proton beam is determined using time of flight (TOF) technique. The deviations over the measured TOF will affect the measured range of the particles. The maximum acceptable error on TOF to keep the range value inside the clinical limit (1*mm* in water) is depicted in Fig. 1.16. At the therapeutic proton energies (60 MeV to 230 MeV), the TOF precision is limited by the required resolution of the energy measurement, which ranges are from about 0.5 MeV for 230 MeV protons energy to 1 MeV for 60 MeV

protons energy. For instance, in case of 1 m distance between the sensors with 500μm uncertainty, using the error propagation on the Equ.6.2, the maximum acceptable errors on the TOF ranges are from 50 ps at 60 MeV to 4 ps at 230 MeV and these limits are more stringent for reduced flight distances.

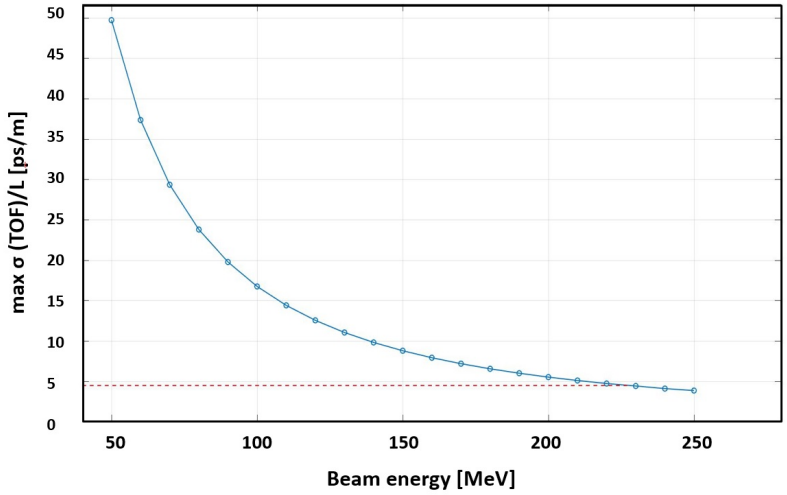

Fig. 1.16: *Maximum acceptable error on ToF per unit distance to measure the energy with an uncertainty corresponding to less than 1 mm error in the beam range in water. The NIST database [48] was used for the energy/range mapping.*

Ultra Fast Silicon Detectors (UFSD) are the choice for the proton beam energy measurement studied in this thesis. In the next chapters structure details and procedure of energy measurement will be described.

Chapter summary

Present chapter gave an overview of basic principles of physical and biological aspects of charged particles therapy. The physics of particle accelerators and different dose delivery methods were summarized. The current beam monitors in particle therapy facilities, their advantages and drawbacks were described. Finally, the main idea of this thesis was expressed in the last section.

Chapter 2

Ultra Fast Silicon Detectors

> "I took a course in speed reading course ... and I was able to go through read War and Peace in twenty minutes. It's about Russia."
>
> Woody Allen

As mentioned in the previous chapter, the main goal of this work is to investigate the use of silicon detectors to measure the therapeutic proton beam energy using TOF technique with high accuracy (less than 1 mm range in water), in a wide range of beam energies between 60 and 250 MeV. To achieve this goal, we need a detector that can quickly measure the energy of particle beams. Such a device could be used for regular quality assurance (QA), for checking the beam energy during irradiation, or even for implementing future adaptive dose delivery schemes with fast energy modulation. Accordingly, the Medical Physics Group of the University of Turin and the INFN Turin have developed a prototype detector that measures the TOF of protons to determine the proton beam energy.

In this chapter, the design and technical details of the dedicated silicon sensors for proton beam energy measurement are described.

2.1 Silicon properties and semiconductor physics

All semiconductors are crystalline solids characterized by an energy band structure. For any of them there is a forbidden energy region in which states cannot exist. Energy regions

or energy bands are permitted above and below this energy gap: the upper bands are called the conduction bands, while the lower ones are valence bands.
At 0 K temperature, all the states in the valence band are occupied and all the states in the conduction band are empty, thus the material behaves like an insulator. As the temperature is raised, electrons acquire thermal energy and some of them acquire enough energy to make a transition from the valence into the conduction band. An electron which obtains enough energy to jump in the conduction band leaves an empty location in the valence band called hole. The separation between the energy of the lowest conduction band and that of the highest valence band is called the bandgap Eg.
Fig.2.1 shows the band structure in solids where the size of band gap determines whether the material is classified as a semiconductor or an insulator. In the absence of thermal excitation, in both insulators and semiconductors the valence band is completely full and the conduction band completely empty. Under these situation, theoretically, neither would show any electrical conductivity [51].
The electron in the conduction band can be made to move under existence of an applied electric field. In this condition, the hole, representing a net positive charge, will also tend to move, but in a direction opposite that of the electron. Electrons will always be drawn preferentially in an opposite direction to the electric field vector, while holes move in the same direction as the electric field.
At room temperature and under normal atmosphere the value of the bandgap is 1.14 eV for highly pure Silicon, as one of the most common semiconductor. This value decreases for highly doped materials and with increasing temperature. When the silicon is doped with a trivalent impurity such as an element from group III of the periodic table (acceptors) "p-type" material can be formed with an excess of holes. If, a doping is performed with type V atoms (donors) "n-type" materials with an excess of conducting electrons is produced.

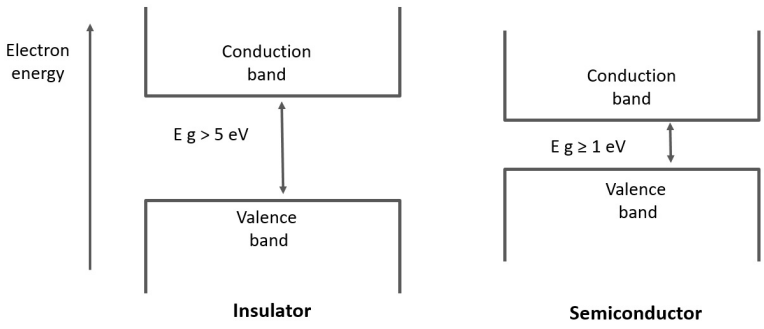

Fig. 2.1: *The band structure in solids. The difference in band gap energy in semiconductor and insulator.*

A p–n junction is a boundary or interface between two types of semiconductor materials, p-type and n-type, inside a single crystal of semiconductor. A silicon detector is based on p-n junctions, where a large depletion region free of conductive charges is formed by applying the external biasing at the interface between the two differently doped zones.

Similarly on how ion-electrons pairs are produced in a gas detector, in a silicon detector the depletion region is the active volume where hole-electron pairs are created by the ionization of the crossing particles. A charged particle crossing the sensitive volumes ionizes the material along its track thus creating electron-hole pairs (e-h) which are collected respectively toward the n++ contact (electrons) and p++ contact (holes) (Fig. 2.2). This induced charge is proportional to the energy loss by the charged particle.

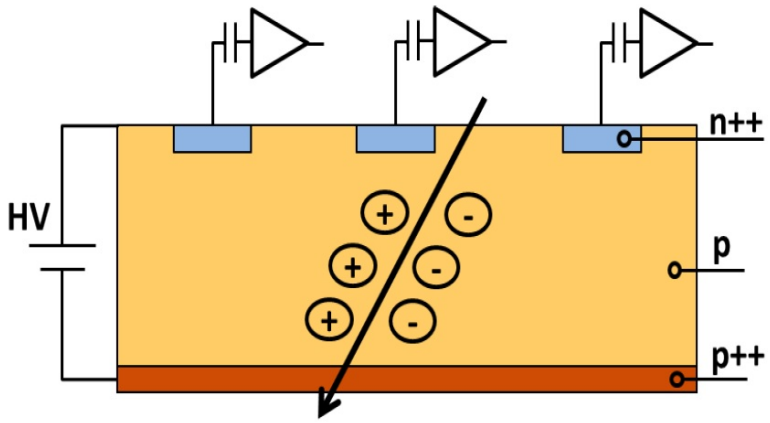

Fig. 2.2: *Basic operational principles of a Silicon detector. An external bias voltage polarizes inversely the p-n junction, creating a large depleted volume. When an incident charged particle crosses the sensor, it creates electron-hole pairs whose drift generates an induced current in the electronics.*

Silicon detectors are built with a plenty of p-n junctions with the electrodes segmented in strips or pixels, and employed for particle tracking in charged particle and nuclear physics applications [52].

An example of a silicon microstrip detector is depicted in Fig. 2.3, it consists of highly doped p-type (p+) strips implanted on a n-type planar substrate, and a n+ backplane electrode. The n substrate is fully depleted by applying a positive voltage on the n+ electrode with respect to the strips. An ionizing particle penetrating through the fully depleted slice generates electron-hole pairs which migrates along the electric field generated by the bias voltage and induce a charge signal on the aluminum strips. In this example strip structures

have a direct aluminum-p+ contact (DC-coupling), but the aluminum electrodes which are separated by a thin SiO2 capacitive layer (AC-coupling) also are used.

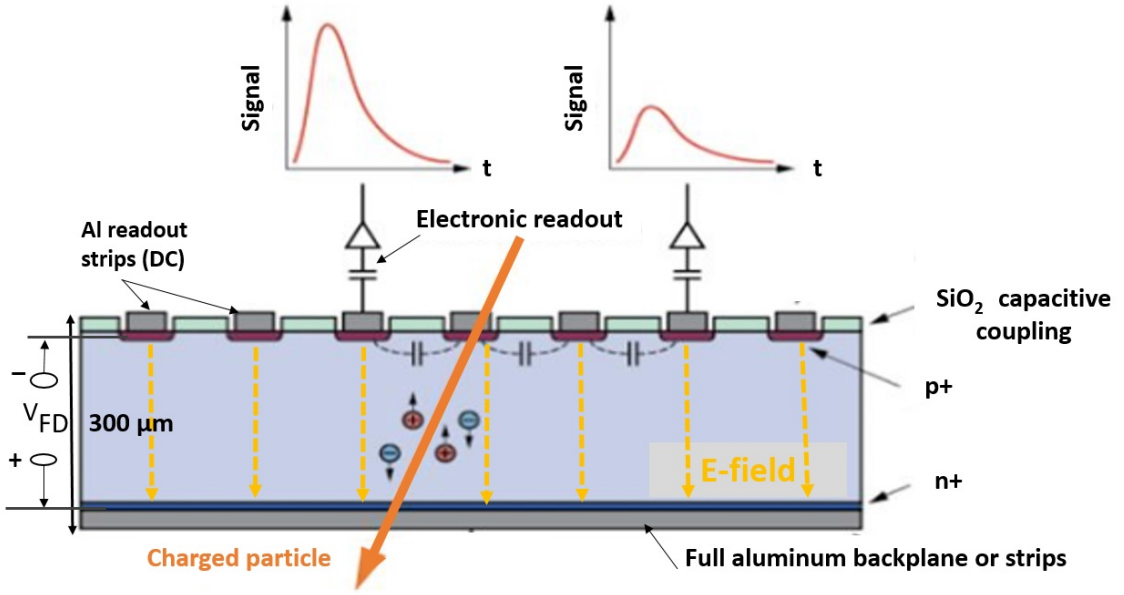

Fig. 2.3: *Charge formation by ionizing particle passing a multi strip silicon detector. In this case only every* 3^{rd} *is connected to an electronics channel. The charge from the intermediate strips is capacitive coupled to the neighbor strips. Picture taken from [53].*

In a typical strip detector, the thickness of the depletion region is about 300 μm to produce enough charge to be detectable by the readout electronics, which contains a charge-sensitive amplifier collecting the signals from each strip. Depending on the applied bias voltage, the typical collection time of electrons and holes is of about 6 to 10 ns. This time is short enough to detect single particles even at high fluxes, if the detector is correctly segmented.

The prominent advantage of semiconductor detectors is the smallness of the ionization energy. This value for both silicon and germanium (as the most common semiconductor material) is about 3 eV, while to create an ion pair in typical gas-filled detectors the required energy is about 30 eV. Thus, for the semiconductor case, the number of charge carriers is 10 times greater than gas filled detector in the same deposition of energy inside the detectors. Moreover, considering the much higher density of silicon with respect to a gas, the charge produced by an ionization particle in a thin silicon layer is high enough

to be measurable for a single particle. This effect leads to increase the attainable energy resolution.

2.2 Ultra-Fast Silicon Detectors

Charge multiplication phenomena in gases and solids are based on the avalanche process which is triggered by a charge moving in large electric fields and leads to impact ionization with an amplification (gain) given by the average number of final particles produced by one particle. In semiconductors this effect is used to detect photons in Avalanche Photon Detectors (APD) [54] with gain of the order of 100's and Silicon Photon Multipliers (SiPM) [55] with a gain of about 10^6. This high value of gain allows achieving very good signal to noise ratios and time resolution [56, 57], while some pitfalls remain such as the difficulties in electronic readout due to the high number of required channels, a variation of the breakdown voltage with temperature which affects in gain and photodetection efficiency and requires calibration test and monitoring of temperature [58]. Two major drawbacks of SiPMs are still the cross-talk between neighboring photo-cells and the after-pulsing which have been dramatically reduced in recent years scientific collaborations [57, 59].

Low-Gain Avalanche Diodes (LGAD) design is based on a modification of the doping profile where an additional doping layer of p+ dopant (Boron or Gallium) is placed on below the n++ electrode to limit the multiplication volume.
In distinction to those applications, Ultra Fast Silicon Detectors (UFSDs) are based on LGADs with a gain of 10-20. The gain factor is defined as the ratio of the charge produced in the LGAD detectors over the charge produced in a similar diode without gain layer. The typical thickness of UFSDs are 35 to 80 μm and a support wafer of about 300 μm can be removed in applications where the reduction of material thickness is important. A simplified drawing for a traditional n-in-p silicon detector and LGAD are shown in Figure 2.4.

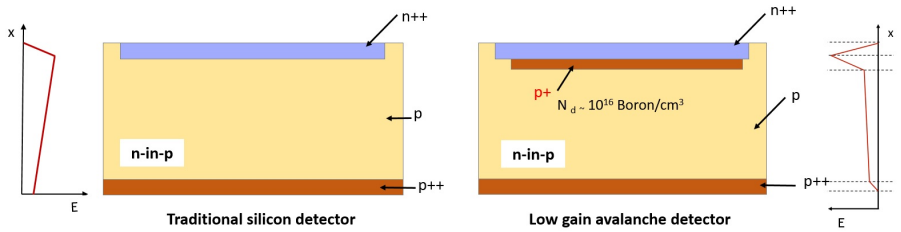

Fig. 2.4: *Left: traditional n-in-p silicon detector. Right: LGAD design, with the introduction of a thin p+ layer below the junction.*

The resulting doping profile is characterized by a large increase of the doping concentration in the immediate vicinity of the junction, which in turn generates a large electric field.

The electric field in LGAD is therefore clearly divided into two different zones: the drift volume with rather low values of the electric field and a thin multiplication zone located within a depth of a few micrometers with very high field ($E \approx 300 kV/cm$). The implants need to be shaped to allow high bias-voltage operation without breakdown. In the n-in-p LGAD design, electrons drifting towards the n++ electrode initiate the multiplication process. While, in the p-in-n design the multiplication is initiated by the holes drifting towards the p++ electrode. Since the multiplication mechanism starts for electrons at a lower value of the electric field than what is necessary for holes multiplication, the n-in-p design offers the best control over the multiplication process.

The intensity of the local electric field and the level of charge gain can be adjusted by changing the depth and doping concentration of the additional p+ layer to obtain a uniform multiplication mechanism across the electrode. Therefore the choice of a suitable electric field is a critical point in the development of LGAD sensors. The electric field must be large enough to achieve charge multiplication and sufficiently small to prevent breakdown. Below the breakdown voltage, the gain increases with the applied bias voltage.

The detection of charged particles instead of photons has the advantage of a much larger initial signal, with an average of 73 electron-hole pairs in one micrometer by a minimal ionizing particle (MIP), which allows to use the lower gain values in the order of 10-20.

The main advantage of LGADs is that they provide an enhanced signal with a fast rising edge in thin detectors (a few tens of microns) with a noise level similar to that of a conventional silicon sensor of the same geometry. This leads to fast detectable signals

of very short time duration (1-2 ns) and a time resolution of about 30 ps in 50 μm active thickness [60]. As the properly thinned down thickness reduces the multiple scattering effects, this guarantees a reduced perturbation of the beam and allows concurrently accurate measurements of time and space in segmented sensors.

The university of Torino in collaboration with INFN Torino division, has optimized thin LGAD detectors, called Ultra Fast Silicon Detectors (UFSD), to enhance simultaneously the space and time resolutions with respect to traditional silicon sensors [61]. An outstanding time resolution of 16 ps has been measured with thin UFSD detectors [62]. These detectors were selected for the purpose of this dissertation. In the following LGAD and UFSD terms will be both used, as synonymous of thin silicon detectors with moderate internal gain.

2.3 Where are the UFSDs produced?

During the previous years, Fondazione Bruno Kessler (FBK, Trento) produced simple pads and small UFSD with a limited number of pixels or strips for R&D purposes. All these structures were designed in collaboration with INFN of Torino, based on Technology Computer Aided Design and Sentaurus (TCAD) simulation tool. These productions were carefully tested in laboratory and in test beams from the Torino group, in order to assess their timing performance and radiation resistance [63]. Moreover in 2017 first prototypes of UFSDs have been produced also by Hamamatsu Photonics K.K. (HPK, Japan)[64].

Further, different front-end alternatives were used for the readout of these sensors, based on simple passive boards for the sensor mounting and high voltage (HV) distribution coupled to external amplifiers, to dedicated ASIC chips optimized for timing measurements [65].

Since 2015, the medical physics group of Torino University in collaboration with INFN Torino has studied the performance of UFSDs to investigate possible medical applications, in particular for beam monitoring in charged particle therapy.

In 2016 the research group joined a collaboration of several INFN institutes to prepare a project on advanced radiobiological studies and measurements, which was financed by INFN Commissione Scientifica Nazionale 5 (CSN5). In this collaboration, the Torino group proposed the development and construction of two beam monitoring prototypes

based on UFSD sensors, to be used in hadron therapy radiobiological experiments, as described in the following section.

2.4 MoVeIT Project

The MoVeIT project (Modeling and Verification for Ion beam Treatment planning) [66] is a multidisciplinary collaboration of the Italian National Institute for Nuclear Physics (INFN) and Italian hadron therapy facilities (Fig. 2.5).
The project started in 2017 with the aims of studying and translating researches in charged particle therapy into clinical outcome, developing innovative treatment planning systems, integrating new biological models to consider the impact of different effects, such as target fragmentation, Relative Biological Effectiveness and intra-tumor heterogeneity. To validate these new models, dedicated devices for beam characterization and monitoring in radiobiological and clinical irradiations were proposed. The UFSD technology was a good choice to build a first prototype of proton beam monitor based on solid state detector.

Prior to the start of the MoVeIT project, the medical physics group in Turin was investigating the possibility of using silicon detectors based on LGAD technology for beam monitoring. Several tests with simple pads on therapeutic proton beams already were carried out to investigate the behavior of these detectors in the harsh environment of a clinical treatment facility.

The optimal design choice for energy beam detector working at the high particle fluxes of a proton therapeutic beam (10^9 to $10^{10} p/(cm^2.s)$) would require thin sensors with a very fine segmentation. Simulations were performed to understand the possible designs and related problems.

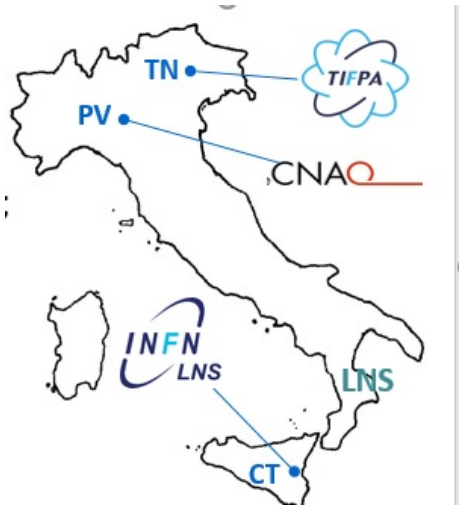

Fig. 2.5: *The Italian hadron therapy facilities in collaboration with MoVeIT project.*

Due to the complexity and cost of the pixel base design detector, for MoVeIT project beam monitor prototypes were proposed based on sensors segmented in strips. In addition, a detector capable of measuring the energy of clinical proton beams using TOF techniques should face several challenges, such as the very good time resolution and radiation hardness. Moreover, the design and technology of the sensors should guarantee their suitability for clinical use in terms of minimal perturbation of the beam, radiation resistance (one year of clinical proton irradiation in a single treatment line equals approximately $10^{15} p/cm^2$) and energy measurement within a time frame of sub-seconds to allow the online beam qualification. Given the larger cross section of strips relative to pixels, the prototypes were designed for a maximum fluence rate of $10^8 p/(cm^2.s)$ above which the signal pileup would start to be an important effect to be considered, especially for the monitoring of the total number of protons delivered to the target.

Based on the mentioned requirements, and achievements by the UFSD collaboration, different UFSDs designs were proposed. More details follow in the next sections.

2.5 The MoVeIT sensor prototypes

2.5.1 HPK production

HPK, in 2017, completed its first production of UFSD sensors,called ECX20840.This production consists of 16 high-resistivity p-type wafers, of physical thickness 150 μm and two active thickness, 50 and 80 μm. four different doping conditions have been implemented; the four gain doses are indicated in table 2.1 with numbers from 1 to 4, where 1 corresponds to the lowest and 4 to the highest one. They were contained a variety of pad structures, notably single pads of area $\sim 0.8\ mm^2$ and 2×2 pad arrays with each pad $3 \times 3\ mm^2$ (Fig. 4.4 bottom). The laboratory characterization of HPK sensors has been performed by UFSD group of INFN Torino, and the promising 4 pads detectors were selected for the first therapeutic proton beam energy measurement at CNAO (Fig.4.4). For all the details about UFSDs produced by HPK, we refer the interested reader to [67–69].

Table 2.1: ECX20840 production by HPK (2017).

Wafer #	**Active thickness [μm]**	**Dopant**	**Doping condition**
1/2	50	Boron	1
4/5	50	Boron	2
7/8	50	Boron	3
10/11	50	Boron	4
13/14	80	Boron	1
16/17	80	Boron	1
19/20	80	Boron	3
22/23	80	Boron	4

2.5.2 UFSD2

Two special LGAD strip structures were designed in Turin using the software tool TCAD Synopsys Sentaurus [70] expressly for the MoVeIT project (Fig.2.6). The thickness of active volume in both designs are 50 μm to keep the signal duration below 2 ns, and the sensors are segmented into strip to ensure sufficiently fine segmentation and to limit the pile-up effects (section 4.4) at the design particle rate. The area of the p+ layer under each strip is 2 mm^2 and the expected capacitance of each channel is about 7 pF. The total thickness of the sensors, including the underlying handling wafer, is about 550 μm In previous structures, this capacitance value has shown to provide an adequate noise level when coupled to the readout electronics.

The first design contains 20 strips with a pitch of 216 μm, with each strip 15 mm long (named "MoVeIT short strips"). The second design features 30 strips, 30 mm long, with a pitch of 146 μm (named "MoVeIT long strips") (Fig 2.6).

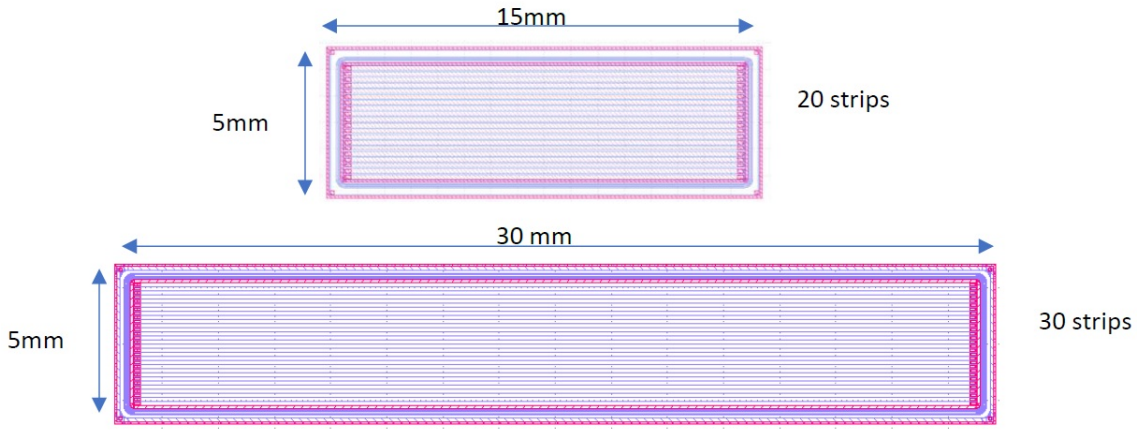

Fig. 2.6: *MoVeIT strip structures. Top (short sensor segmented in 20 strips), bottom (long sensor segmented in 30 strips).*

The MoVeIT structures were included in multi-project, called UFSD2, wafers depicted in Fig.2.7 and produced at Fondazione Bruno Kessler (FBK, Trento) in 2017. 18 wafers were produced with different doping modalities in order to study the optimal strategy in terms of radiation resistance, each wafer containing 8 long strip and 8 short strip sensors. One sensor of each of the two designs was also produced without adding the gain layer in order to measure directly the gain by comparison.

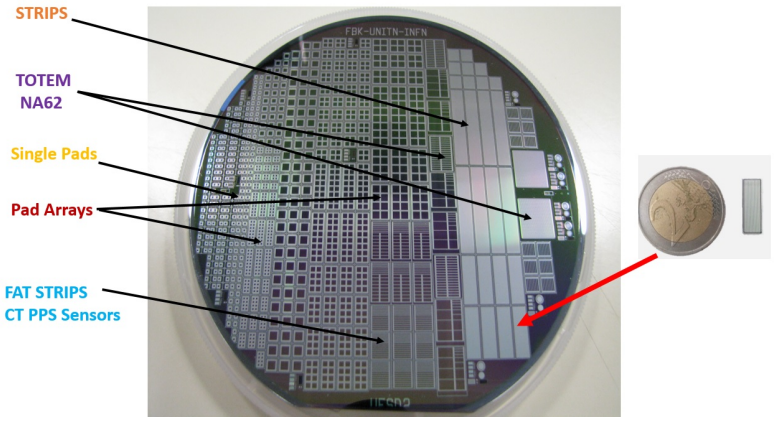

Fig. 2.7: *Wafer includes different sensors (left), MoVeIT short strips (right).*

The list of different doping alternatives used in each wafer is shown in Fig. 2.8. Boron or Gallium with different doses were implanted as p+ gain layer, different thermal cycle resulting in low or high diffusion of the implanted acceptors, and in some wafers the implantation of a dose of carbon was added. The expected gain value of the MoVeIT strips is about 10.

UFSD2				
Wafer #	Dopant	Gain dose	Carbon	Diffusion
1	Boron	0.98		Low
2	Boron	1.00		Low
3	Boron	1.00		HIGH
4	Boron	1.00	Low	HIGH
5	Boron	1.00	HIGH	HIGH
6	Boron	1.02	Low	HIGH
7	Boron	1.02	HIGH	HIGH
8	Boron	1.02		HIGH
9	Boron	1.02		HIGH
10	Boron	1.04		HIGH
11	Gallium	1.00		Low
12	Gallium	1.04		Low
13	Gallium	1.04		Low
14	Gallium	1.04		Low
15	Gallium	1.04	Low	Low
16	Gallium	1.04	HIGH	Low
17	Gallium	1.04		Low
18	Gallium	1.08		Low

Fig. 2.8: *Table summarizing the doping parameters adopted for each wafer in the FBK production of UFSD2.*

Fig. 2.9 shows a detail and the corresponding the cross section view of UFSD2. Guard rings are n-implants that enclose the active area and have the same polarity of the n-electrode. Guard rings protect the n-electrode collecting charges produced in the periphery of the sensors, reducing the current flowing in the electrode and avoiding the collection of charges which come from the outer part of the sensor and would increase the noise.
Another important part is the n-deep or JTE (Junction-Termination-Extension) that is basically a region of n-Silicon placed at the end of the gain layer volume. Such structure is used to contain the field lines in the active volume and avoiding to collect charges outside it [71]. The JTE tends to create an inter-strip zone where the charges are not multiplied due the absence of the gain layer. The "no gain zone" between two gain layers has a nominal width of 66 μm for both short and long strips structures produced for MoVeIT.

This generation of MoVeIT structures called “UFSD2” and dedicated to particle counting of therapeutic proton beams is extensively described in [72].

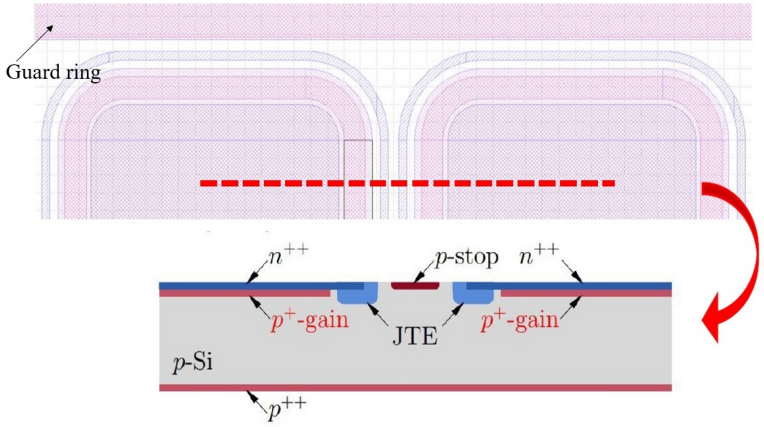

Fig. 2.9: *Two strips in the UFSD2 structure with cross section.*

2.5.3 UFSD3

A third design of MoVeIT structures, added to a later UFSD3 production, were designed for the proton beam energy measurement and were produced by FBK in 2018. UFSD3 sensors contain 11 strips, 2.2 mm^2 active area each, 540 μm strip width and 4000 μm strip length with a pitch of 590 μm. The total thickness of UFSD3 is 550 μm (50 μm active thickness + 500 μm handling wafer). The first strip of this sensor is without gain layer to study the gain factor. In order to use a laser beam to perform tests in laboratory, there are optical windows in the upper metal layer in first, tenth and 11th strips. Fig 2.10 shows a picture of a UFSD3 wafer and a zoom of the MoVeIT strip sensor.

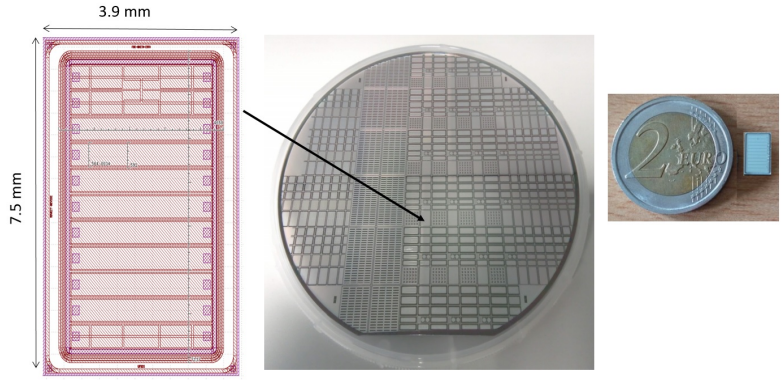

Fig. 2.10: *MoVeIT sensor dedicated for energy measurement and wafer includes different sensors .*

Similarly, in UFSD3, 20 wafers were produced with different doping modalities in order to study the optimal strategy in terms of radiation resistance. Boron with different doses was implanted as p+ gain layer , different thermal cycle resulting in low or high diffusion of the implanted acceptors, and in some wafers the implantation of a dose of carbon were performed (see Fig. 2.11). The nominal width of "no gain zone" in UFSD3 is 51 μm.

UFSD3				
Wafer #	Dopant	Gain dose	Carbon	Diffusion
1	Boron	0.98		Low
2	Boron	0.96		Low
3	Boron	0.96	A	Low
4	Boron	0.96	A	Low
5	Boron	0.98	A	Low
6	Boron	0.96	B	Low
7	Boron	0.98	B	Low
8	Boron	0.98	B	Low
9	Boron	0.98	C	Low
10	Boron	1.00	C	Low
11	Boron	1.00	D	Low
12	Boron	1.02		HIGH
13	Boron	1.00		HIGH
14	Boron	1.02	A	HIGH
15	Boron	1.00	A	HIGH
16	Boron	1.02	B	HIGH
17	Boron	1.02	B	HIGH
18	Boron	1.04	B	HIGH
19	Boron	1.02	C	HIGH
20	Boron	1.04	C	HIGH

Fig. 2.11: *Table summarizing the doping parameters adopted for each wafer in the FBK production of UFSD3.*

Both UFSD2 and UFSD3 strip sensors were tested in laboratory and with proton beams. In parallel, a batch of LGAD pads have been irradiated with protons and neutrons at high fluxes to evaluate their radiation resistance.

Chapter summary

Chapter 2 reviewed the physics, features and advantages of traditional semiconductor detectors and explained the charge formation by ionizing particle passing a multi strip silicon detector. The ultra fast silicon detectors as a new technology based on LGAD was described and different aspects of their properties were extensively presented. The MoVeIT project in which this thesis was done, was introduced. Two different UFSD prototypes with all the related structure details were described.

Chapter 3

Laboratory characterization of the MoVeIT sensors

> "A scientist in his laboratory is not a mere technician: he is also a child confronting natural phenomena that impress him as though they were fairy tales."
>
> Marie Curie

This chapter describes the part of the work performed within this thesis for a preliminary study of the properties of the MoVeIT strip sensors described in the previous chapter. First, a set of measurements were intended to characterize the behavior of each channel, using static measurements performed with a probe station and a multichannel analyzer. In a second step, the signal produced by a pico-second laser and the gain level of the sensors have been studied. Therefore, the most promising strip sensors have been tested with therapeutic proton beams, to characterize their behavior in a realistic environment.

3.1 Laboratory setup

The setup used for the sensor characterization consists of the following components:

- Probe station with card holder
- Source/Measurement Unit (SMU)

- Multi needles Probe card
- Switching matrix
- National instruments LabVIEW control software

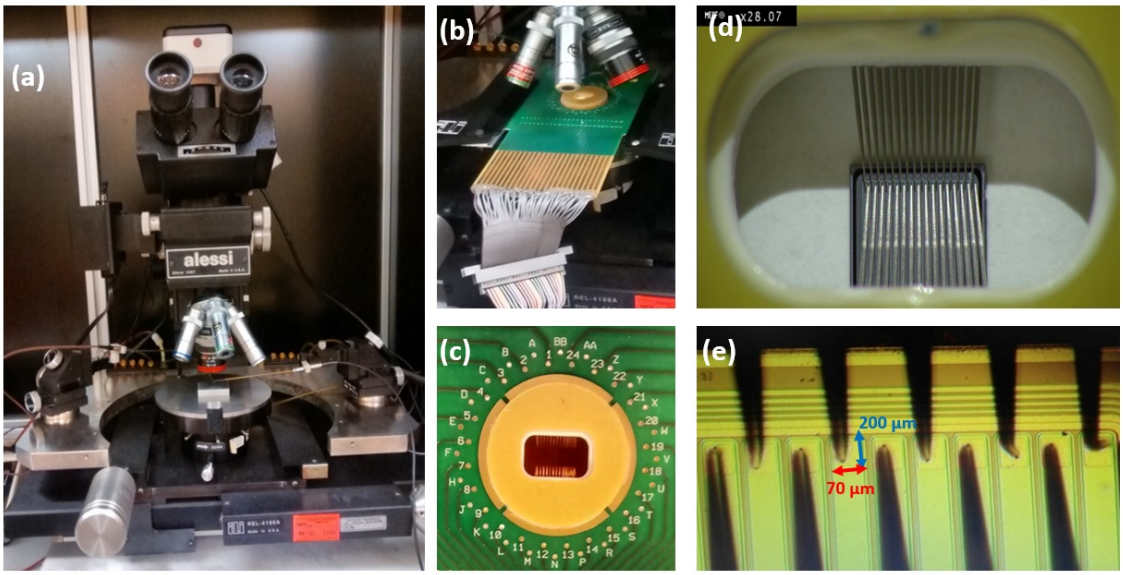

Fig. 3.1: *(a) probe station with an optical microscope, (b) probe card, (c) Zoom on the needles part, (d) needles in contact with strip UFSD, (e) zoom showing the orientation of needles and their contacts on the strip pads.*

3.1.1 Probe station and SMU unit

All the measurements were performed with a probe station (Fig. 3.1) connected to a source/measurement unit (SMU) (Fig 3.2). In particular, it allows obtaining I(V), C(f) and C(V) curves, fundamental to understand the UFSD properties. The probe station is the instrument shown in Figure 3.1(a).

Fig. 3.2: *Left: Keysight Technologies Source/Measurement Unit (SMU), Right: switching matrix.*

This station is provided with an optical microscope with three different magnifications, a video camera to visualize the device on a screen and a support structure called chuck. The device under study (DUT) is positioned on the chuck and it is kept still with the help of a vacuum pump. In order to perform characterization measurements, it is necessary to polarize the sensor: a potential difference is generated on opposite sides of the DUT using the chuck and the dedicated probcard. The chuck and the needles are then connected with triaxial cables to the modules of SMU, shown on the left side of Figure 3.2, through a switching matrix unit.

The SMU is a Power Device Analyzer / Curve Tracer, model Keysight B1505A [73], including of a single box solution used to provide the HV to the sensor and measure currents and capacitance from the contacts of the probe station pins. The SMU Analyzer is equipped with three modules:
• High Voltage Source Monitor Unit B1513C (HVSMU), with a range up to 3000V and 8mA;
• Medium Power Source / Measure Unit B1511B (MPSMU), with a range up to 100V/0.1 A and a minimum measurement resolution of 10 fA / 0.5 μV;
• Multi Frequency Capacitance Measurement Unit Module B1520A (MFCMU), with a frequency range from 1 kHz to 5 MHz and an AC signal level of amplitude up to 250mV.

The device enables precise $\mu\Omega$ resistance measurements and provides 10 μs fast pulses for transient measurements. Moreover, the SMU can be programmed to generate a ramp of bias voltages and to measure the current and capacitance for each V_{bias} value automatically saving the results in files or in graphs.

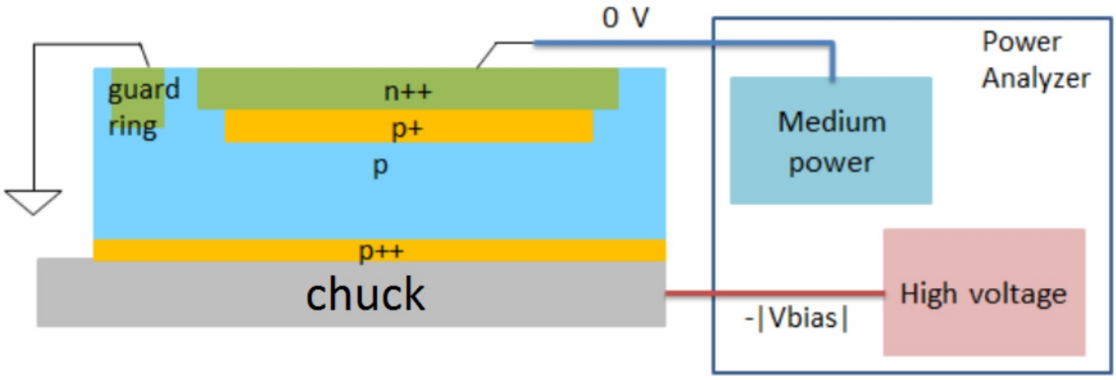

Fig. 3.3: *scheme of the probe station connections to a single pad.*

Figure 3.3 depicts the connections of the one sensor channel: a high negative voltage is provided by the HVSMU module to the p++ backplane of the sensor through its connection with the chuck of the probe station, while the sensor guard ring is connected to ground. The n++ electrode is connected to the MPSMU monitor unit.

The information on sensor parameters such as depletion voltage, leakage currents, sensor gain and breakdown voltages are provided by the measurements of the current as a function of the bias voltage (I-V curves). In addition, the measurement of the capacitance as a function of the bias voltage (C-V curves) gives important information on the doping profiles.

The probe station was enclosed in a black metal box to avoid the noise due to electromagnetic interference and light impinging on the sensor. All the measurements were performed at room temperature and using a matrix unit and a multi-needle probe card. The temperature effects on the UFSD performances were investigated in the UFSD group of INFN Torino and results show as the temperature decreases, the gain and drift velocity increase, the sensor leakage current decreases, and the breakdown voltage moves to lower sensor bias values [74].

3.1.2 Probe card and matrix unit

A dedicated probe card and a switching matrix module were used to test all the strips of each sensor, automatically. A switching matrix consists of a series of inputs and outputs which connections between the inputs and outputs can be made by closing one or more relays. While the number of inputs on a switching matrix is fixed, the number of outputs is usually determined by the number of cards installed in the matrix mainframe. A matrix unit (Keithley 7002) [75] (Fig. 3.2 right) was used to connect the SMU to a multi needle probe card which was used to probe all the strips of a sensor and automatically analyze all the channels one after the other.

A specified LabVIEW [76] software was used to configure the matrix unit, synchronize the matrix unit with the SMU operations, collect and save the I-V or C-V curves measured for each strip. In order to accurately measure the current from the connected strip, the remaining strips are grounded especially the ones on the edge of the sensor.
Two customized probe cards were produced, with the geometry of the needles corresponding to the number and pitch of the contacts of the two types of strip sensors. They are

passive printed circuit boards (PCB) with multiple needles with tips of a few μm to ensure a good connection to the sensor pads with the smallest contact area (Fig. 3.1(c,e)).

The probe cards for the long and short strip sensors in UFSD2 have 32 and 22 needles, respectively. The probe card for the UFSD3 sensors has 13 needles. The two extra tips with respect to the number of strips are used to connect the guard ring to ground. The electrical connection between the needles and the input channels of the matrix unit was guaranteed through a flat cable (Fig. 3.1(b)).

3.1.3 IV curves

I-V curves were extracted for each strip by measuring the two currents (one current from the strip, the second one from the backplane) as a function of the bias voltage. These curves allow to determine the value of the full depletion voltage, to investigate the presence of superficial currents. Moreover, the breakdown voltage can be derived from I-V curves (above this voltage value an avalanche starts to be produced in the sensor).

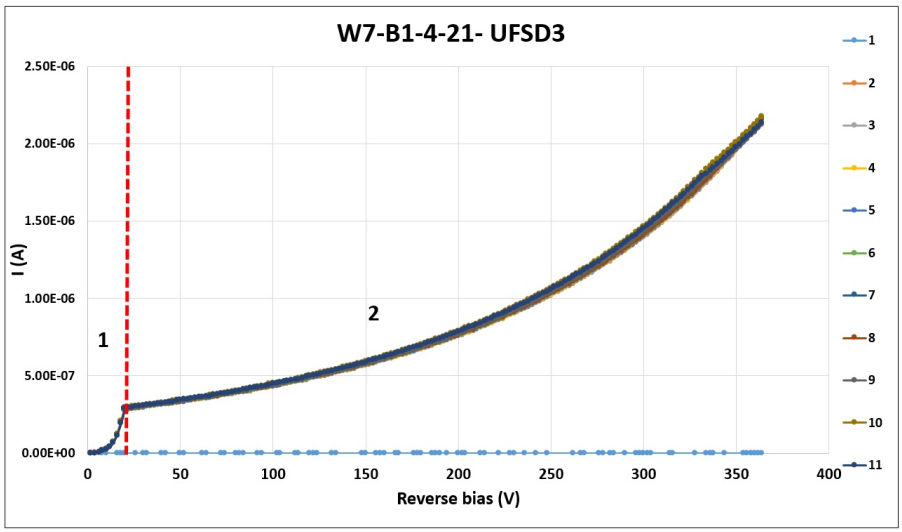

Fig. 3.4: *Example of I-V curves of each of the 11 strips of UFSD3 sensor. The red dash line indicates the full depletion voltage, the current increases with the square root of the applied voltage in the first region and increases slowly with the V_{bias} until it reaches the breakdown voltage.*

Figure 3.4 shows an example of I-V curves of UFSD3 wafer no.7 (Fig. 2.11) for each of the 11 strips. The typical I-V curve for the strip is composed of two regions separated by a "knee". The surface current is measured below 20 V; between 20 and 30 V the current

shows a rapid increase "ankle" due to the depletion of the gain layer and $\sim$ 5 V later (knee) flattens due to the depletion of the bulk; above 30 V sensors are fully depleted and the exponential growth of the dark current is due to the relationship between gain and the reverse bias [60, 77]. Above the full depletion voltage the current increases slowly with the V_{bias} until it reaches the breakdown. These measurement were performed to identify abnormalities in strips to select only sensors with uniform behavior for the proton beam irradiation. The lowest I-V curve in Fig. 3.4 refers to strip number one which is without gain layer: for these strips or sensors, the current is approximately independent of the bias voltage.

For the other UFSD strips with gain layer, the current increases with the bias voltage due to the multiplication of the minority charges thermally produced in the sensor bulk which depends on the electric field in the gain region. The comparison of the slopes of I-V curves from sensors with gain with respect to the sensors without gain layer and the same geometry provide an indicative value of the gain factor. This measurement has not been performed in this study: a more precise value of the gain factor was instead obtained by comparing the output signals from sensors with and without gain, using laser pulses to emulate the effect of particle crossing or with real particles.
Fig. 3.5 shows an example of I-V curves collected for two different sensors of UFSD2 with and without gain layer of wafer no.4 (Fig. 2.8) containing 30 strips. Similarly, in UFSD2 the different behaviour between sensor with gain and without gain layer is obvious.

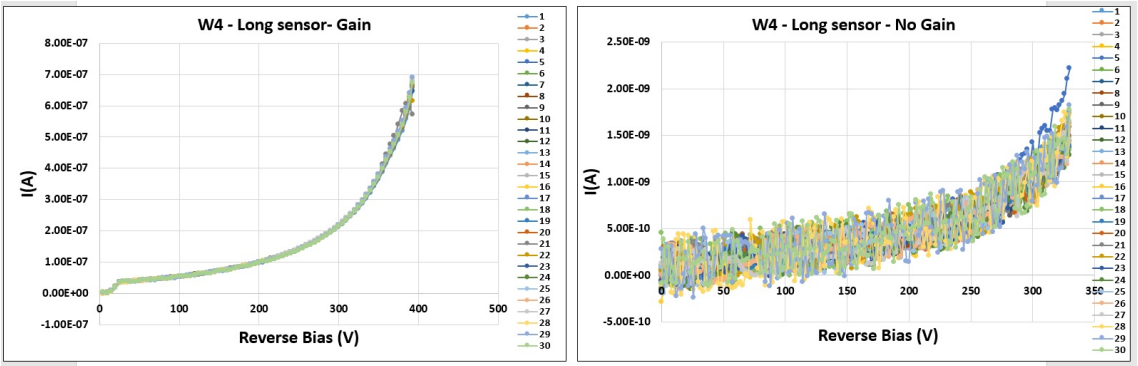

Fig. 3.5: *Example of I-V curves for long sensors of UFSD2 (dedicated for particle counting). The long sensor with gain layer (left), the long sensor without gain layer (right).*

To study the behaviour uniformity of UFSD3, the currents of all the I-V curves for each wafer were evaluated at bias voltage 300 V and reported in Fig. 3.6, where the location of

the sensor in the UFSD3 wafer is also displayed to show possible non-uniformities of the gain layer implant on the wafer surface.

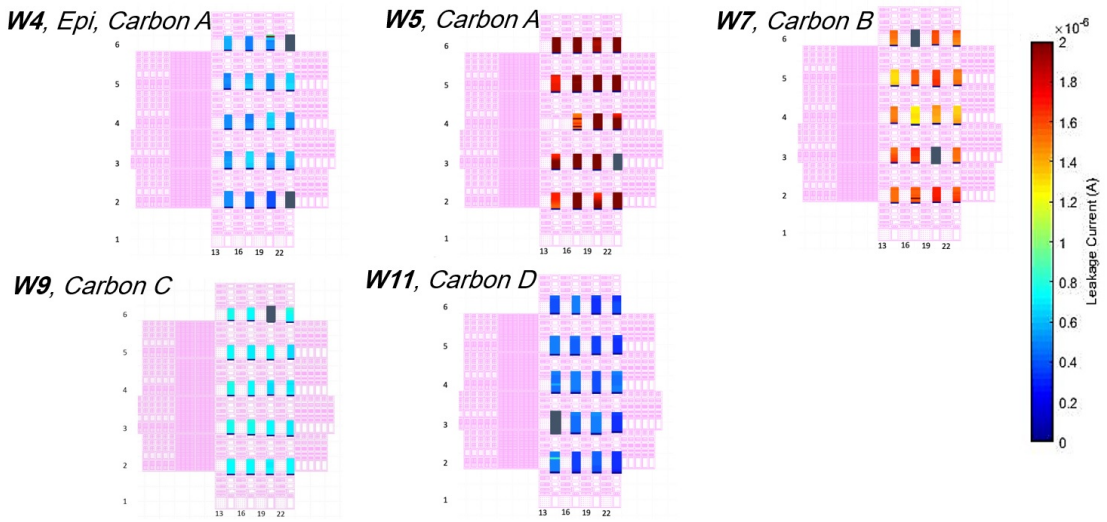

Fig. 3.6: *Uniformity study of MoVeIT UFSD3 sensors at bias voltage 300 V. 7 sensors out of 100 were broken and are indicated in gray color.*

Due to the advantages of the thin sensor (see sec. 2.2), we selected 20 sensors from different wafer of UFSD3 prototype and sent them to Aptek company in U.S [78] to remove most of the thickness of the underlying handling wafer. Starting from a thickness of 600μm, the thickness of 12 sensors was reduced to 120μm and 8 sensors to 70μm thickness. The distribution map of sensors selected for thinning is shown in Fig. 3.7.

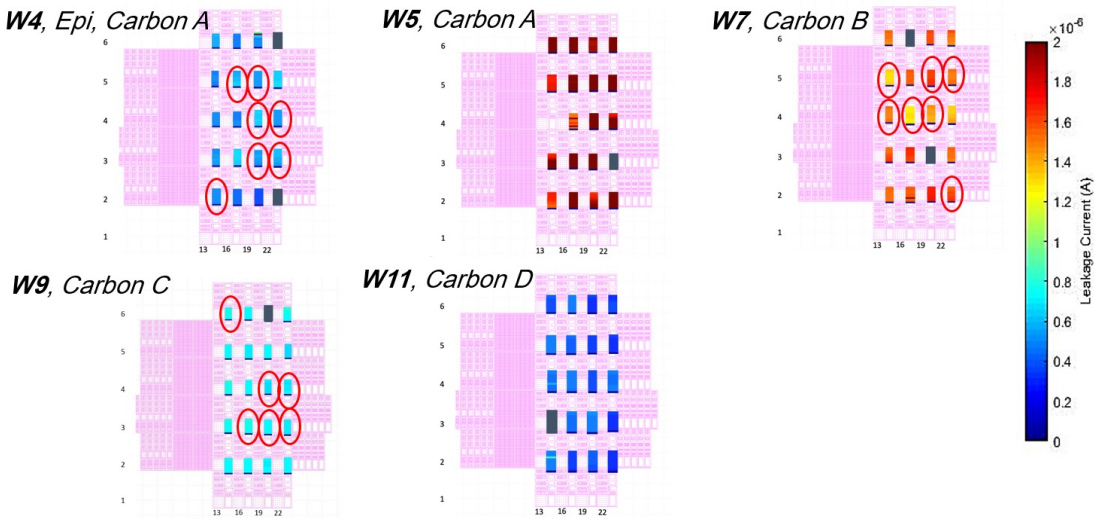

Fig. 3.7: *The 20 sensors from different wafer as marked in red circles were selected to be thinned.*

A microscope picture of the backside of UFSD3 before and after thinning emphasizes the removal of the backside metallization layer, see Fig.3.8 .

Fig. 3.8: *The view of the back side of UFSD3 under the microscope before and after thinning which emphasizes the removal of the metallization layer.*

Due to very small thickness (70 μm and 120 μm) and fragility of the thinned sensors, to measure the I-V curves of thinned sensors, we used the air pump for placing the sensors on the chuck in the probe-station. The examples of I-V curves comparison before and after thinning for two thickness (70 μm and 120 μm) are shown in Figs. 3.9 and 3.10. The break down voltage results reduced for all the thinned sensors from about 450 V to 330-370 V. Fig.3.11 shows an example of thinned sensor which seems damaged during the thinning process. In comparison with the sensor performance before thinning, it is clear that all the strips show different behavior as function of bias voltage and their performance are not properly.

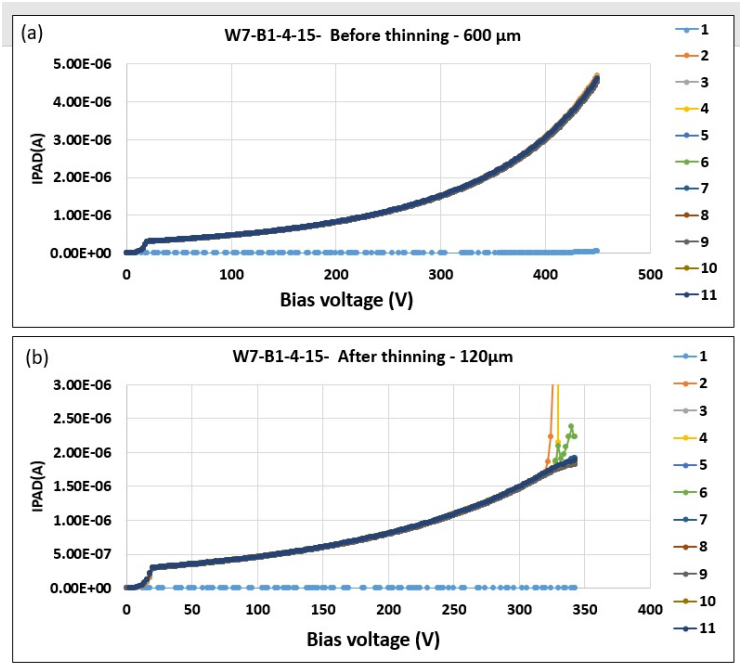

Fig. 3.9: *Example of IV curve of a sensor selected from wafer 7, before (a) and after (b) thinning. The total thickness of UFSD was* 600μm *and was thinned in this example down to* 120μm.

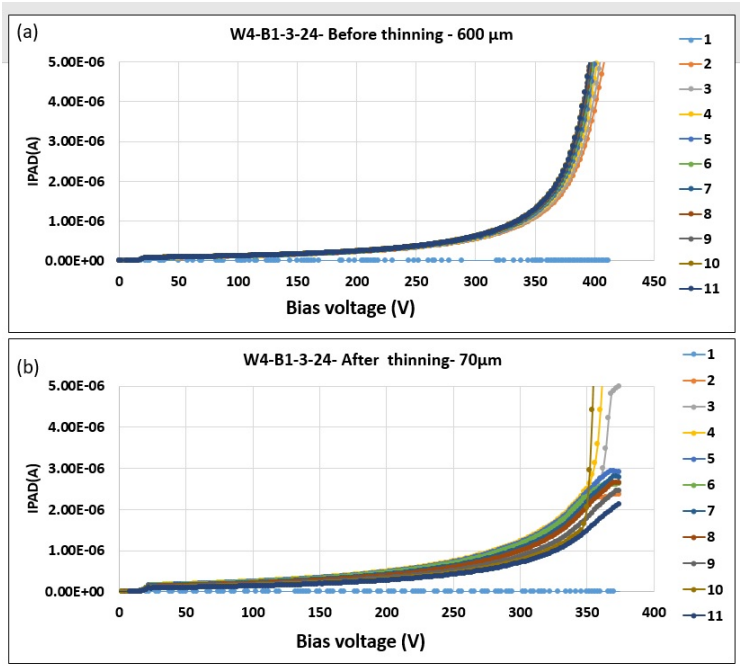

Fig. 3.10: *Example of IV curve of a sensor selected from wafer 4, before (a) and after (b) thinning. The total thickness of UFSD was* 600μm *and in this example was thinned down to* 70μm.

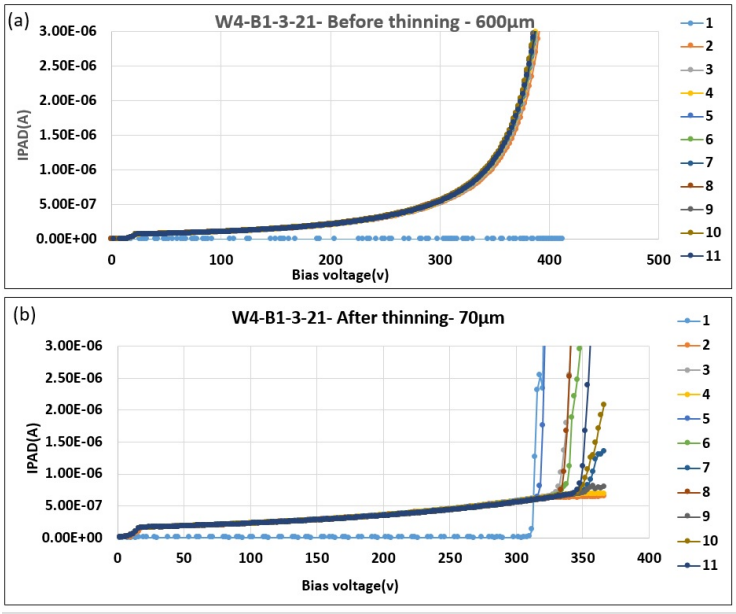

Fig. 3.11: *Example of IV curve of a damaged sensor during the thinning process, before (a) and after (b) thinning. The total thickness of UFSD was* 600µm *and was thinned in this example down to* 70µm.

All the I-V curves of the 20 thinned sensors were evaluated at bias voltage 300 V. The map of thinned sensors uniformity study indicated that 2 sensors out of 20 were broken (3.12). According to the laboratory measurements of thinned sensors and comparison with the sensor functionality before thinning, the best ones were selected to be irradiated with a proton beam.

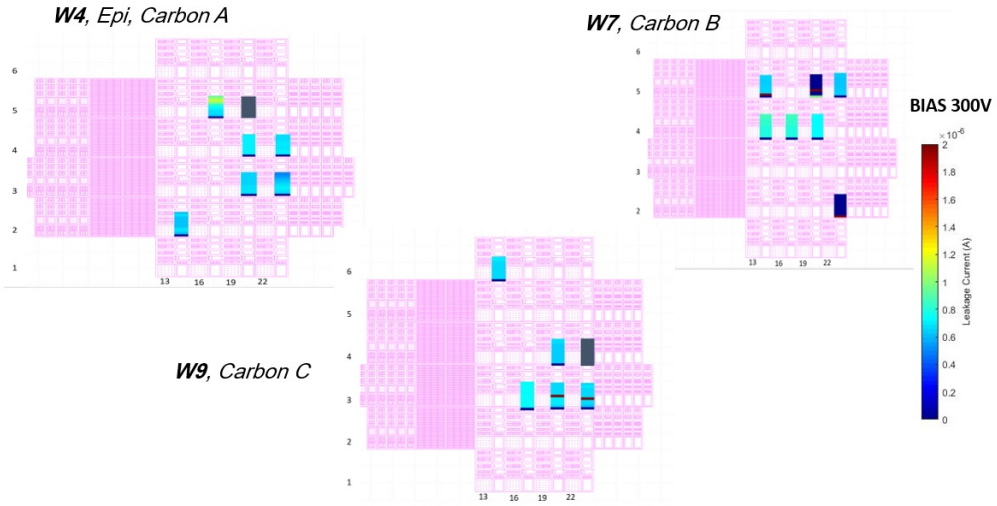

Fig. 3.12: *Uniformity study of MoVeIT thinned sensors at bias voltage 300 V. Two sensors out of 20 were broken during thinning and are indicated in gray color.*

3.1.4 C-V curves

Another laboratory test is the strip capacitance as a function of the applied polarization voltage. The procedure to evaluate C-V measurements involves the application of DC bias voltages across the sensor capacitance while making the measurements with an AC signal. Generally, for these measurement AC frequencies from about 10 kHz to 10 MHz can be used.

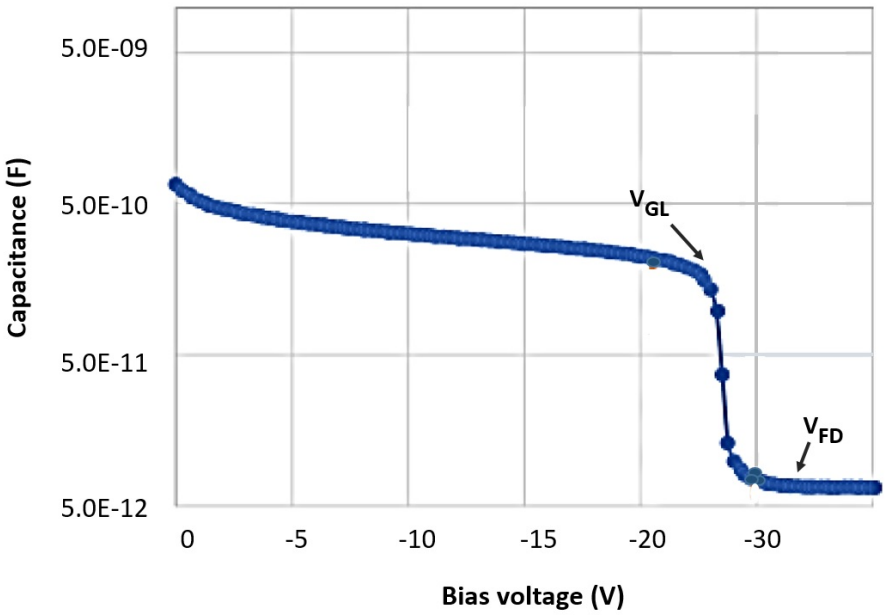

Fig. 3.13: *C-V curve for a sensor from wafer no.4 UFSD3.*

The capacitance of several strips as a function of V_{bias} was measured at 10 kHz AC signal. Figure 3.13 is an example of strip sensor C-V curve.
The C-V curve allows to determine precisely the value of the depletion voltage and to estimate the doping profile. The relation between capacitance, the acceptors density N_A and the bias voltage V_{bias} for a sensor of active area A is given by:

$$C = A\sqrt{\frac{q\varepsilon\mu_h}{2V_{bias}}.N_A} \tag{3.1}$$

where q, ε, μ_h are the electron charge, the silicon permittivity and the holes mobility respectively. Moreover, a capacitance drop (knee) at few ten volts, this knee corresponds to the depletion voltage V_{GL} of the gain layer, which is proportional to the active doping

concentration N_A and to the square of the width W of the gain layer implant.

$$V_{GL} \propto \frac{qN_A}{2\varepsilon} W^2 \tag{3.2}$$

The full depletion voltage V_{FD} of the device occurs when the capacitance becomes constant. Equations 3.1 and 3.2 indicate that the capacitance of a sensor is proportional to the inverse of the depth. In addition, it is noticeable that the Bias voltage V_{bias} is proportional to the doping concentration. The higher the doping concentration is, the higher will be the depletion voltage.
The ideal C-V characteristic of a standard p-n junction diode is a $\frac{1}{\sqrt{V_{bias}}}$ curve, which becomes constant when the sensor is fully depleted and the capacitance reaches a constant value:

$$C = \varepsilon \frac{A}{d} \tag{3.3}$$

Thus, from the measurements, the depletion voltage can be defined as the voltage value at which the capacitance becomes constant. The doping concentration of the bulk can be determined using the depletion voltage value which is extracted from the C-V curve and the sensor thickness.

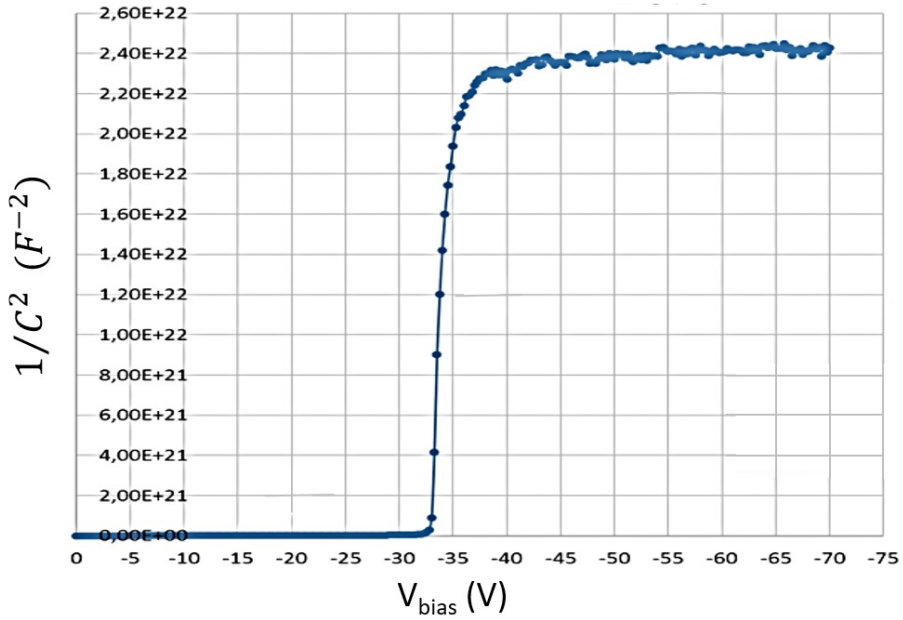

Fig. 3.14: $\frac{1}{C^2}$ *as a function of the bias voltage.*

As indicated in Fig. 3.14, there are three different part in C-V curve ($\frac{1}{C^2}$ as a function of V_{bias}). When the inverse bias voltage starts to increase, the first region to be depleted is the

gain layer: this region is fully depleted at few tenths of volts. The depletion voltage of the gain layer (knee) is proportional to its doping concentration: it is possible to compare the doping concentrations of different devices simply evaluating their gain layer voltageV_{GL}. When the gain layer volume is fully depleted, the bulk depletion begins, which is the second region of the C-V curve. Full depletion of the bulk is reached in a few volts, although it is thicker than the gain layer, but its doping concentration is much lower.

The profile of the acceptor doping concentration N_A can be determined from $\frac{1}{C^2}$ as a function of V_{bias} curve. The dependence of $\frac{1}{C^2}$ and V_{bias} from Equ. 3.1 for $V_{bias} < V_{dep}$ is given by:

$$\frac{1}{C^2} = \frac{2V_{bias}}{q\varepsilon\mu_h A^2} \cdot \frac{1}{N_A} \tag{3.4}$$

and when the detector is fully depleted, it reaches a constant value.
By Equ. 3.1 to 3.4, the acceptor concentration as a function of the depth in the strip was estimated and an example of results from this analysis is shown in Figure 3.15.

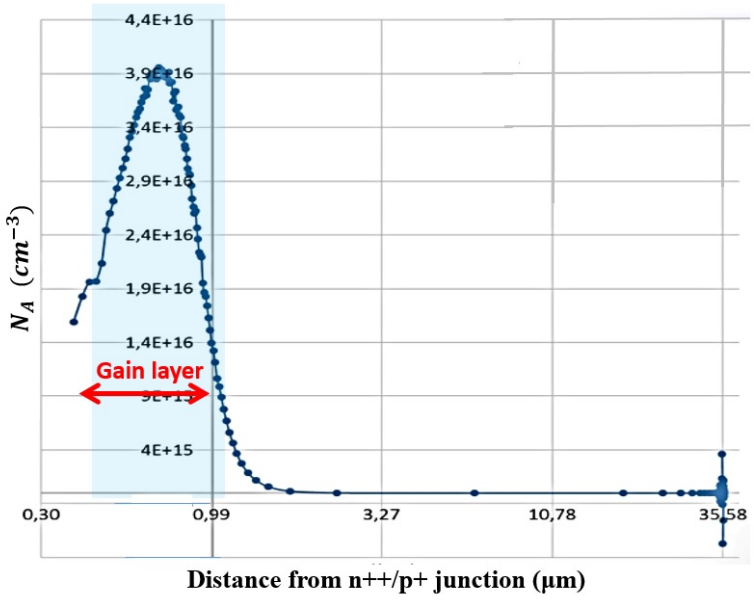

Fig. 3.15: *Doping profile, acceptor doping concentration as a function of the sensor depth.*

The peak which extends up to 1-2 μm inside the sensor correspond to the p+ gain layer implanted below the n++ electrode. The flat region indicates the dopant concentration of the sensor bulk, while the last little peak at the end of of curve is the dopant concentration of the p++ electrode in the backplane. The values of dopant concentration which were

measured in laboratory were compatible with the design values expected after implantation. I was involved to all the sensors characterization procedure during the first year of my PhD and I did the laboratory measurements for both UFSD2 and UFSD3. Given the number of wafer, sensor and strip in each prototype, I performed characterization and analysis of 120 sensors from UFSD2 and 120 sensors from UFSD3 (5160 strips in total).

3.2 Readout for signal shape acquisition

Based on the previous characterization, sensors were sorted according to their functionality within a range of bias voltages where they were supposed to have a gain value of about 10 with acceptable dark current and quite far from the breakdown limit. Sensors with strange behavior, low reliability, or anomalous strips were rejected.

A passive custom board was already designed by INFN Torino to test the first UFSD produced for timing applications. This board (shown in Fig. 3.16) is designed in order to distribute the bias voltage produced by a HV power supply to the sensors and to connect up to 2 channels to external amplifiers. To readout accurately the signal shapes avoiding long recovery times and tails, these custom board were coupled to external broadband amplifier produced by Cividec [79], which are low-noise current amplifiers with an analog bandwidth of 2 GHz and 40 dB gain.

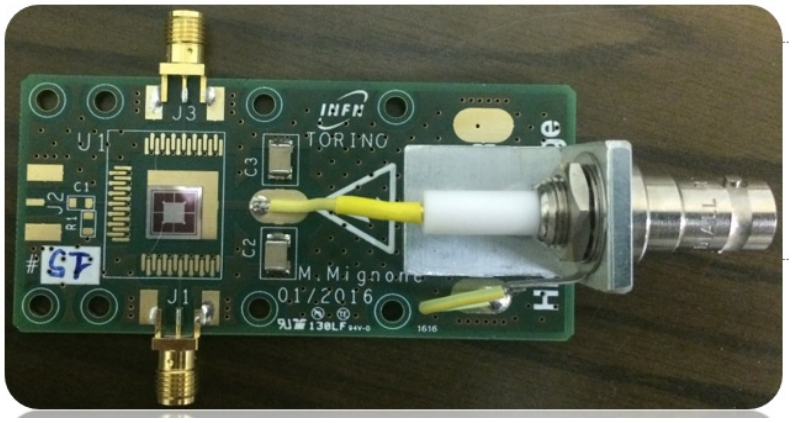

Fig. 3.16: *Two channels passive board made by INFN Torino. In this case at most 2 pads from 4 pads UFSD can be connected.*

Within the RD50 collaboration a characterization technique called Transient Current Technique, or TCT, has been tuned and largely used to study the harmful effects of radiation

in Si [80]. In our tests we used the TCT setup to look at the amplitude of the signal. In TCT a fast pulsed laser is used to emulate the crossing of a particle. The induced current is amplified and time resolved using a wide band oscilloscope. We can infer information of the doping, electric field and charge collection efficiency of the detector by studying the shape of the induced current.

A fast-pico-laser (PiLas) [81] provides fast pulses (few tens of ps) at 1060 nm wavelength. Since infrared waves can pass the silicon detectors, they generate the same signals which are generated by charged particles in this situation.

The laser pulse was distributed through an optical fiber and focused with a lens mounted at the end of the fiber to a small spot of less than 10 μm. The laboratory setup (Fig 3.17) was composed of:

- Picosecond laser (PiLas) by Advanced Laser Diode Systems with controller EIG2000DX, wavelength 1060 nm, simulating a MIP
- Oscilloscope (LeCroy, with a maximum sampling capability of 40 Gs/s)
- Power supply (Keithley 2410)
- Cividec amplifier 40dB

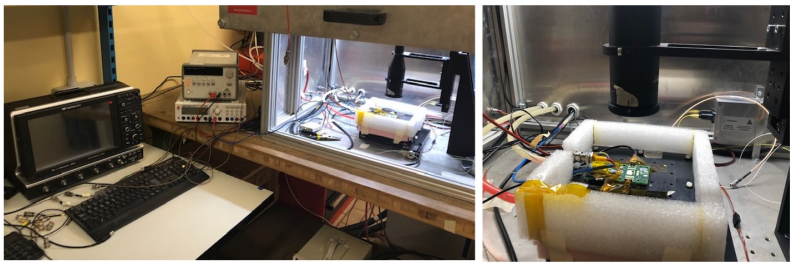

Fig. 3.17: *Transient Current Technique (TCT) setup, consist of picosecond laser, oscilloscope, power supply, Cividec amplifier (Left) and zoomed view of UFSD bonded on the custom board (Right).*

The presence of an optical window on the top metal layer of the sensor is required to avoid laser reflection. The UFSD2 sensors produced for the MoVeIT project have a continuous metallization contact covering all the strip area that do not allow to use a laser beam perpendicular to the sensor to inject a charge. Therefore the laser beam was injected from the detector edge, parallel to the strip. Fig. 3.19 was obtained by using this arrangement.
In UFSD3 production instead optical windows were designed in first, tenth and eleventh

strips. Fig. 3.18 depicts a typical signal from a UFSD which was collected with the oscilloscope in coincidence with a laser pulse. The laser light was splitted in two parts and one was sent to the reference diode used as a reference to determine the amplitude for the laser pulse.

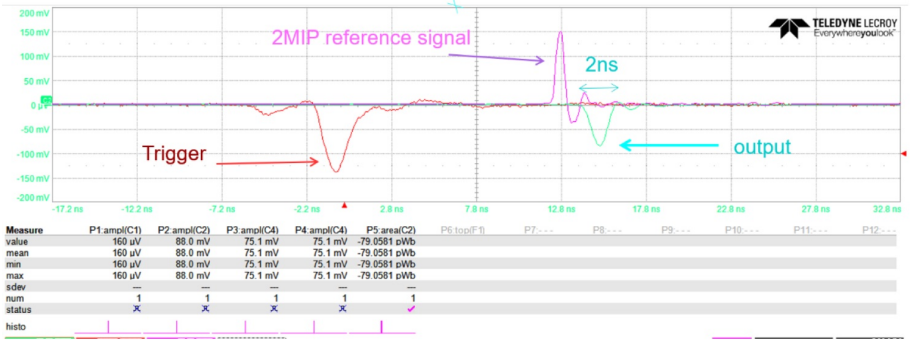

Fig. 3.18: *A oscilloscope screenshot showing the amplified signal from a UFSD (green), reference diode (pink) and the laser trigger signal (red).*

3.3 Measurements with laser pulses

The laser was used to estimate the gain of the sensor defined as the ratio of signals from sensors with gain and without gain with the same geometry and same bias voltage as a function of the hit position between a pair of strips.

Two adjacent strips with gain layer of a UFSD2 sensor and two adjacent strips without gain layer have been connected to the same active board with internal amplifier and the output signals were readout with an oscilloscope.
A laser spot diameter of less than 8 μm was moved with 2 μm steps in both the directions orthogonal to the strip length, and the amplitude of the output signal for fixed laser pulses was measured for each spot position. The results are shown in Figure 3.19, where the vertical position indicates different depths in the sensors below the strip contact, while the horizontal position covers two strips and the interstrip region. The enhanced signal from the two strips is clearly visible, while the signal in the dead region between two strips is strongly suppressed.
The bottom part of the figure shows the signal amplitude on the horizontal position for a fixed depth in the sensor. The blue and black curves are the signal amplitudes measured with two strips with gain, whereas the green and red lines are the amplitudes from two strips of a similar sensor without gain.

The distance from the two signals obtained at half maximum is 60 μm, which is in agreement with the results expected from the TCAD simulation in the design. Due to the diffusion of the laser beam inside the sensor and also the geometry of the laser shooting parallel to the strips, a little amount of cross talk is visible.

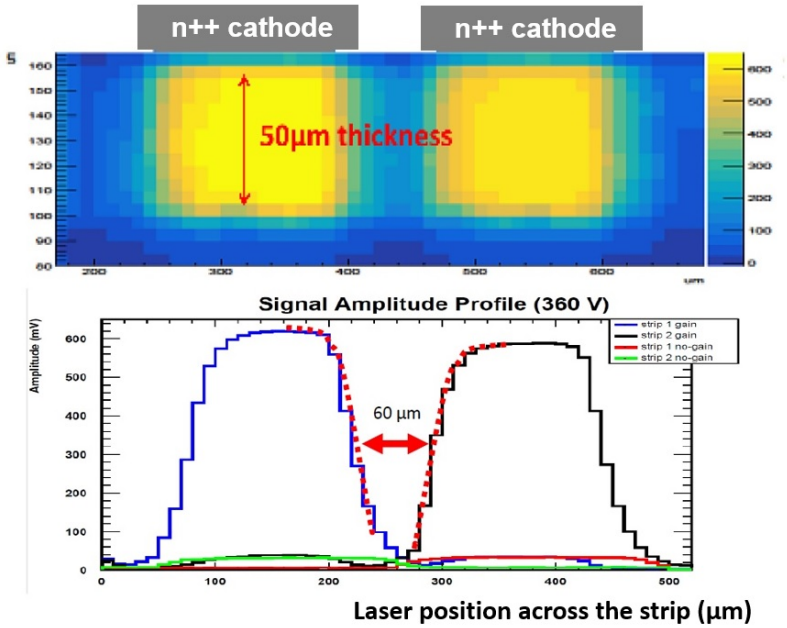

Fig. 3.19: *Top: 2D dependence of the signal amplitude measured as a function of the position in two orthogonal directions orthogonal to the strip length for a sensor with gain. Bottom: a profile of the signal amplitude for a fixed vertical position for the two strips of a sensor with gain (blue and black) and for a similar sensor without gain (red and green).*

The gain factor of the UFSD sensor is defined as the ratio of the output signals from the two sensors (one with gain and another without gain layer) at the same operating parameters. The gain factor as a function of the bias voltage using the TCT test was measured for UFSD2 sensors and the results are shown in Fig.3.20. The gain factor increases with the bias voltage, and the nominal value of 10 is obtained with a bias voltage of about 320 V.

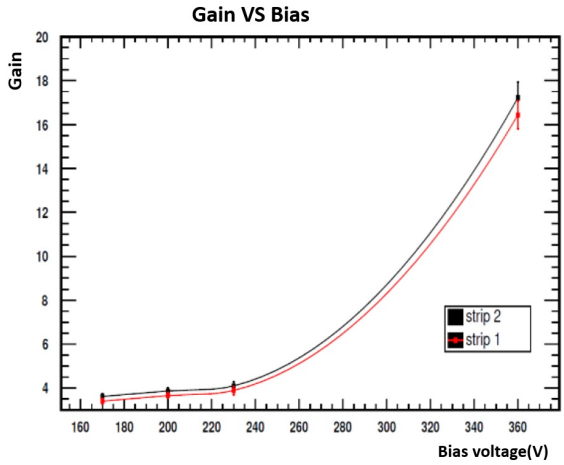

Fig. 3.20: *Gain value of two neighboring strips in function of the bias voltage.*

3.4 Radiation resistance of UFSD structures

In order to test the UFSD radiation resistance, some of the UFSD structures produced in the same wafers of the MoVeIT strip sensors have been irradiated with neutrons up to a fluence $\Phi_n \approx 3 \times 10^{16} n/cm^2$ (Ljubljana) and with high energy protons up to $\Phi_p \approx 9 \times 10^{15} p/cm^2$ (CERN). The effect of radiation on the performance of structures from different wafers produced with alternative doping modalities have been studied by our colleagues in Torino working on UFSD development [82].
Both neutrons and protons cause a reduction of gain in the LGAD sensors, due to "acceptor removal" mechanism and simultaneously the creation of defects and traps in the sensor bulk. These two effects are parameterized by the following equation [82]:

$$\rho_A(\Phi) = g_{eff}\Phi + \rho_A(0)e^{-c\Phi} \tag{3.5}$$

where Φ is the irradiation fluence in cm^{-2}, $\rho_A(\Phi)$ is the acceptor density in cm^{-3}, g_{eff} a constant (0,02 cm^{-1}) and c is a coefficient parameter describing the acceptor removal mechanism. The parameter c depends on the initial acceptor density $\rho_A(0)$ and on the type of irradiation.

The density of active acceptors in the gain layer can be measured from C-V curves as described in section 3.1.4. The main results are summarized in Fig.3.21 (proton irradiation) and Fig.3.22 (neutron irradiation). In both cases, the fraction of active acceptor density

$(\frac{\rho_A(\Phi)}{\rho_A(0)})$ is reported as a function of the fluence for sensors from different wafers. The lines in the figure are fits to the data according to Eq. 3.5.

Based on these results, it comes out that a higher gain reduction is observed when Gallium dopant is used as acceptor with respect to Boron. In both the cases the addition of carbon in the gain layer improves the radiation resistance. Additionally, a thermal cycle with low diffusion is helpful in improving the radiation resistance. In general, narrower and more doped gain implants have a higher resistance to the radiation dose (more details in [74, 83, 84]). However, it should be mentioned that the loss of gain can be partially recovered by increasing the reverse bias voltage, as shown in Fig. 3.20. The carbon dose A (Fig. 2.11) is currently the dose that maximizes the gain layer radiation hardness. To conclude, a fluence up to $10^{15} p/cm^2$ can be tolerated before degradation of the sensors starts to show up. This would correspond to more than 1 year of operation in a clinical environment. Since the carbonated gain layer holds the possibility of designing silicon sensors with gain with enhanced radiation resistance, the UFSD group of INFN Torino plans to further investigate the property of the carbonated gain layer by producing gain layers with several carbon doses, to optimize the radiation resistance of the LGAD design. They are confident that their findings, also can be successfully implemented in other silicon sensors with gains such as SiPM and APD.

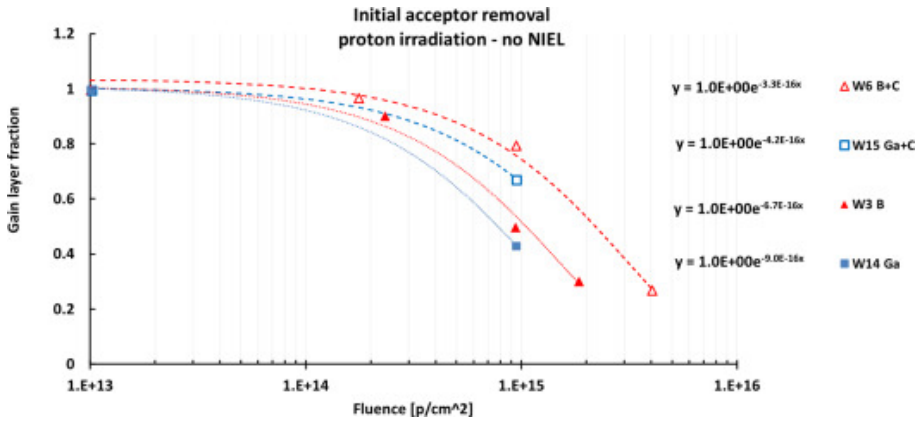

Fig. 3.21: *Fraction of gain layer still active as a function of proton irradiation [85].*

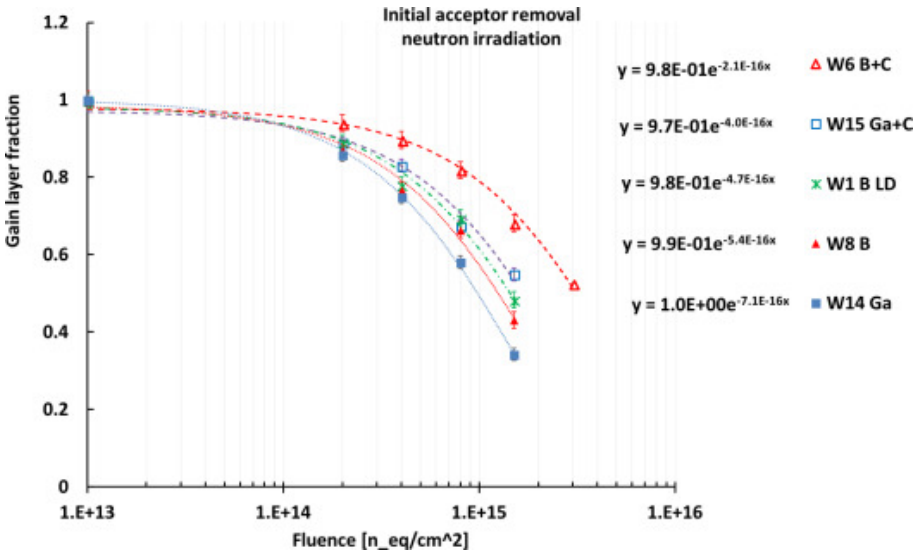

Fig. 3.22: *Fraction of gain layer still active as a function of neutron irradiation [85].*

Chapter summary

This chapter comprised of characterization of the MoVeIT strip sensors in laboratory. The laboratory setup and all the steps to evaluate the electrical properties of UFSD2 and UFSD3 sensors as function of bias voltage were explained. A passive custom board in order to distribute HV inside the sensor for timing application was introduced. The TCT laser beam set up was outlined probing the internal structure of UFSD, information of the doping, electric field, charge collection efficiency of the detector and their gain value. The effect of radiation on the performance of structures from different wafers produced with alternative doping modalities was given. Based on the laboratory characterization, the most promising strip sensors were selected to test with therapeutic proton beams, to characterize their behavior in a realistic environment.

Chapter 4

The beam test in proton therapy facilities (CNAO and TIFPA)

"A rare theorist turned experimentalist."

Willis Lamb,
Nobel prize winner in physics, 1955

The present chapter describes the characterization of the therapeutic proton beam by the TOF technique using the UFSD detectors. The experimental measurements were carried out at two proton therapy facilities in Italy. All the equipment and test setup are explained first, followed by the description of the data acquisition procedure, the TOF measurement and identification of real coincidence signals. At the end of this chapter the proton energy determination is reviewed with particular focus on the related parameters.

4.1 Beam characteristics of CNAO and TIFPA

In Italy, there are three charged particle therapy facilities: CATANA (Centro di AdroTerapia ed Applicazioni Nucleari Avanzate, Catania), CNAO (Centro Nazionale di Adroterapia Oncologica, Pavia) and TIFPA (Trento Institute for Fundamental Physics and Applications, Trento)(Fig. 4.1). The silicon strip sensors described in the previous chapters were tested with therapeutic proton beams of the CNAO and TIFPA.

Fig. 4.1: *The proton therapy facilities in Italy and summary of their features.*

At CNAO, a synchrotron is used to accelerate particles to treat tumors with a full active delivery system [86]. This synchrotron provides a beam energy range 120 to 400 MeV/u for carbon ions (C^{+6}) and 60 to 250 MeV for protons (p), corresponding to a range in water between 3 cm and 27 cm, selectable with 0.1 cm steps. In order to provide whole volume irradiation, several beam energies have to be shot providing monoenergetic spills in a periodic sequence (Fig. 1.9).

The period of the synchrotron is between 4 and 5 seconds, with an approximate spill length of 1.5 sec, and the inter-spill time needed to set up the machine magnets for the following beam. The accelerator can provide a maximum of 4×10^8 C^{+6} or 10^{10} protons per spill, leading to a maximum beam current on the patient of 0.38 nA and 1.6 nA respectively. The corresponding beam fluence rate for protons is between 10^9 and $10^{10} p/cm^2 s$ depending on the FWHM and extraction settings and between 4×10^7 and 4×10^8 for carbon ions [42].
The spot position is accurate within ± 1 mm over the whole 20×20 cm^2 scan field; homogeneity in a uniform squared field was measured to be within $\pm 5\%$ for both particle types at any energy [87].

There are four beam transport lines that guide the beam into one of the three treatment rooms (Fig.4.2). Two rooms are equipped with a single horizontal fixed beamline, while in the third one, horizontal and vertical fixed beamlines are available. Each room includes the beam nozzle with monitor chambers, the patient positioning, and the immobilization system [88]. An additional beamline is available from 2020 to distribute the beam in an experimental room.

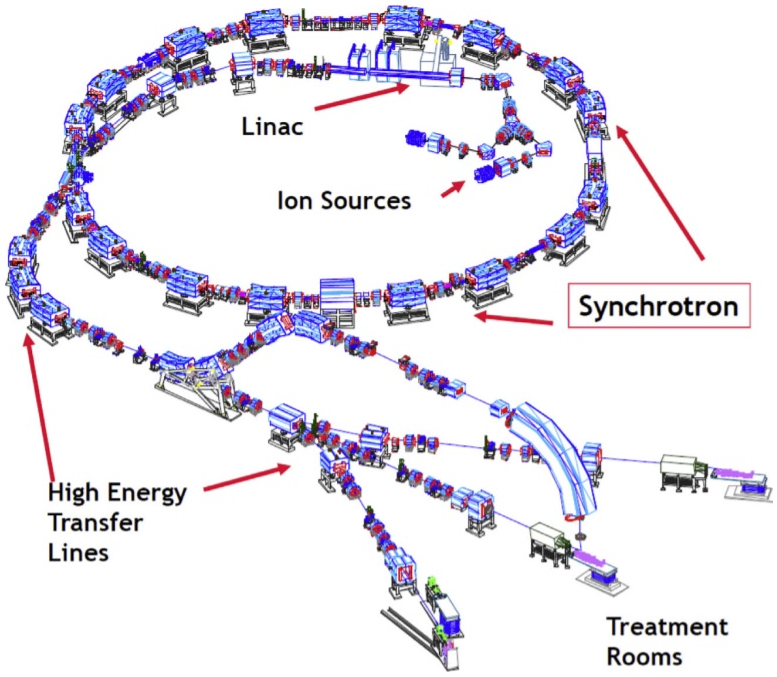

Fig. 4.2: *Scheme of the CNAO beam delivery, with the beam distributed in three treatment rooms. The beam line to the experimental room is not shown in the picture [88].*

Another Italian treatment facility is the Proton Therapy Center at Trento (TIFPA) [89], built by the commercial IBA [90], and based on a Proteus 235 cyclotron, which accelerates protons at an energy of 228 MeV (Fig. 4.3). Shortly after the cyclotron exit, a coarse energy selection is carried out by a rotating degrader of different thicknesses and materials, and a magnetic energy selection system to provide the desired energy down to the minimum value of 70 MeV.

There are two treatment rooms equipped with rotating gantries and an experimental room which is totally dedicated to research [91]. The beam cannot be shared simultaneously among the different rooms and can only be requested alternately in either the gantries or the research area.

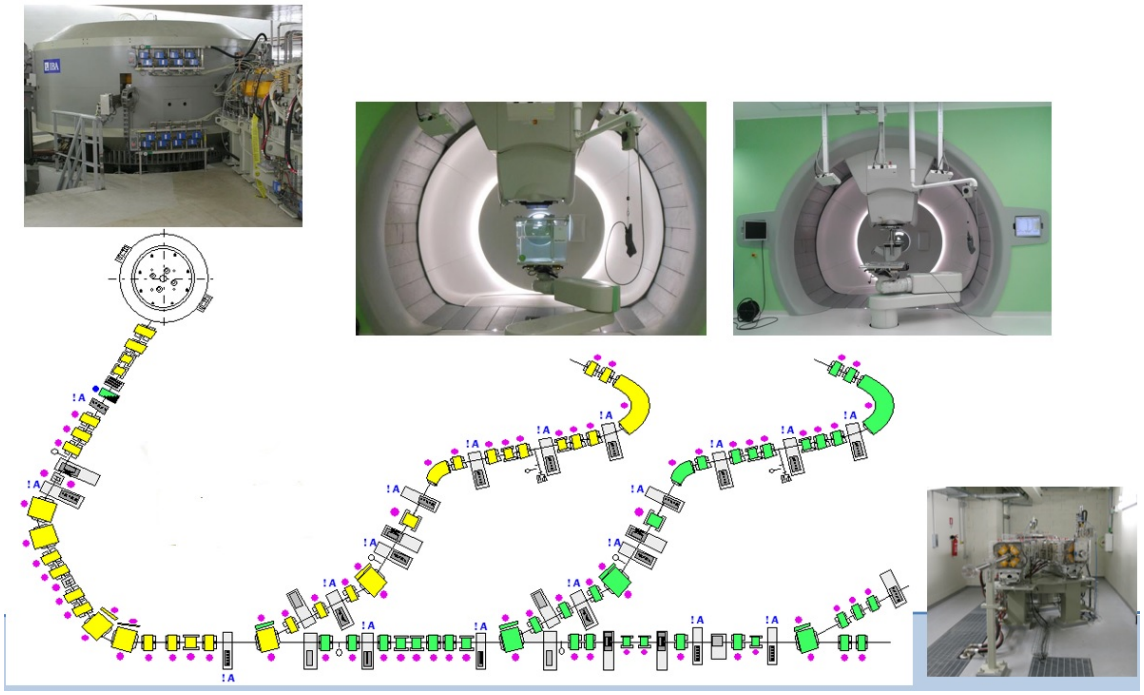

Fig. 4.3: *Trento proton therapy center (TIFPA) [92].*

Different beam intensities in a range between 1 and 320 nA can be requested and the corresponding maximum beam rates scale accordingly. The maximum particle rate depends on the beam energy, ranging from $3.8 \times 10^6 p/s$ at 70 MeV, up to $2.3 \times 10^8 p/s$ at the largest energy for a cyclotron extraction current of 1 nA. The proton beam current is modulated by a 50% duty-cycle square wave, with a 100 ms period.

This cyclotron also provides low beam intensities, with rates 10^1 up to $10^5 p/s$ which are required for a broad spectrum of experiments. To this aim, the accelerator works in an operational regime that is different from the standard clinical one. In fact, such low intensities are obtained by exploiting the so-called accelerator "dark current", achieved by decreasing the high voltage of the accelerator source below the threshold used for standard operations. We refer the interested reader to[86, 88, 42, 91] for more details about the beam line in CNAO and TIFPA.

4.2 Beam test description

As reported in chapter 3 , the MoVeIT sensors were designed, produced and tested in the laboratory. After analysis of the performance of the sensors under laboratory tests, the best ones were selected in order to be irradiated by proton beam at hadron therapy centers.

As depicted in Fig. 4.4, for the TOF measurement, a telescope prototype was assembled for the first tests using two UFSDs (named S1 and S2 in the following) manufactured by Hamamatsu Photonics, HPK (Japan). Each sensor was segmented to 4 pads $3 \times 3mm^2$ and with a total thickness $230\mu m$ (80 μm active thickness and 150 μm physical support). The two UFSDs were fixed on general purpose High Voltage (HV) distribution boards, where only one out of the four pads was connected to the output on the board. The HV was applied to each sensor by connecting the board to an external power supply, independently for each sensor[93].

A low-noise current amplifier [94] characterized by an analogue bandwidth of 2 GHz and a 40 dB gain was used for the two signals of the sensors. These amplified signals were acquired using $16+1$ channels digitizer desktop module [95]. The digitizer features 12 bit signal sampling at 5 GS/s, with one ADC count corresponding to 0.24 mV, and 1024 samples stored for each trigger corresponding to a waveform of 204.8 ns duration.
Some quantities are defined in the present dissertation as follows.

- 1 sample = 0.2 ns
- 1 event = 1024 samples (204.8 ns) stored by digitizer

An optical link connects the digitizer with a PC through a CAEN PCI CONET A2818 Controller [96], which allows to transfer data at 80 MB/s which is 3 times faster than an alternative USB connection. A custom modified version of the CAEN software Wavedump [97] was used to configure the working parameters, to control the acquisition and to provide an asynchronous software trigger as soon as the previous event was collected and saved on disk. The conversion time of the digitizer (110 μs) and the time needed to transmit and store the data ($\sim 500\mu s$) limit the acquisition rate to about 1 kHz.

Referring to Fig. 4.4, the mechanical structure for the TOF telescope contains a rigid horizontal support whit 10 grooves on its surface to fix the position of S2 precisely via locating pins. In addition, two motorized stages are used to remotely move S2 in two orthogonal directions.

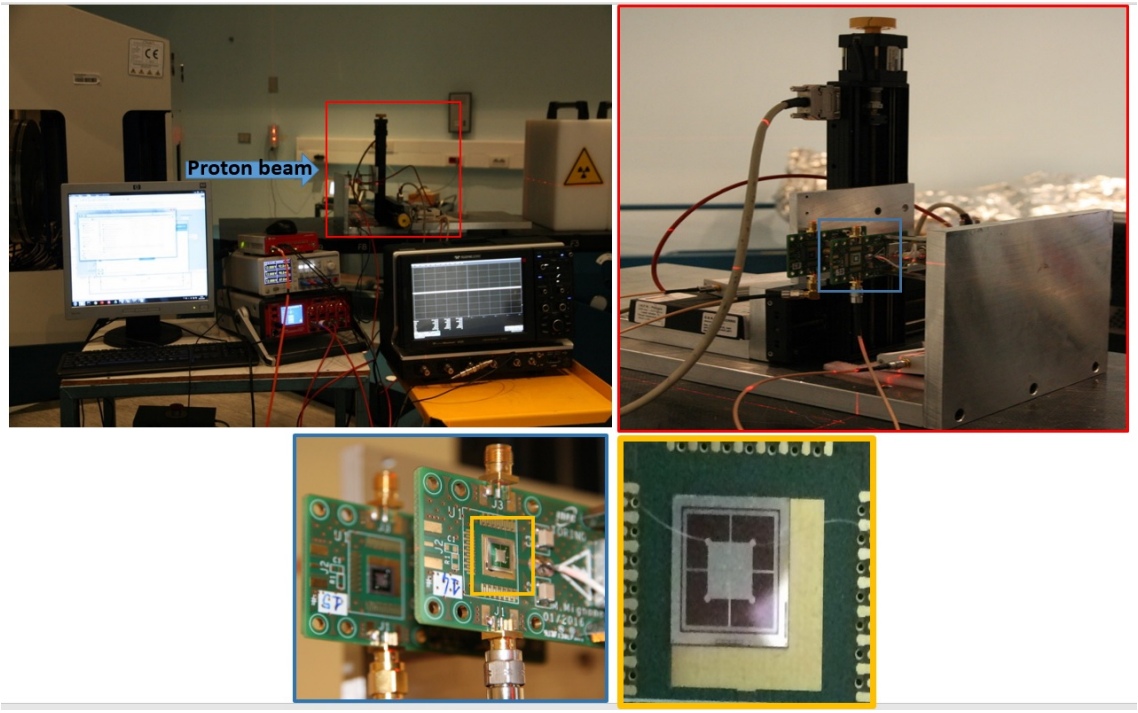

Fig. 4.4: *The setup of data acquisition from a beam test conducted at CNAO. Top) All the connections of electronic read out, the blue arrow points out the beam direction. The focus on the telescope structure. Bottom) The sensors bonded on the two dedicated HV passive board, and the Hamamatsu sensor made of 4 pads* $3 \times 3mm^2$ *and 80* μm *active volume thickness.*

4.2.1 The beam test at CNAO using pad sensors

To evaluate the sensitivity of the ToF method to measure the proton beam energy, the telescope structure was irradiated in a clinical treatment room of the CNAO facility. To obtain the TOF, several tests using different proton beam energies and different distances between sensors were performed. Five proton beam energies were used (58.9, 77.6, 103.5, 148.5, 226.1 MeV) at a beam fluence rate of $5 \times 10^8 ps^{-1} cm^{-2}$.
These energy values, defined as nominal energies, where extracted from the PSTAR dataset of the National Institute of Standards and Technology [98] from the five water equivalent depths (respectively: 30, 49, 82, 155, 320 mm) measured at the isocenter of CNAO during the commissioning with a maximum deviation $< \pm 0.15mm$ [87].
For each energy, the two sensors on the telescope were positioned at four different distances of approximately (7, 37, 67, 97 cm). The distances were measured using a ruler which was not very accurate. The actual distances will be obtained from the calibration procedure explained in section 6.2.
For each distance d, at the first, the sensors alignment was performed using the laser beam

in treatment room which indicate the isocenter position and the beam path. The S1 was positioned at isocenter, then, using the movable stage, the S2 transversal position was repeatedly changed remotely by user. The movements covered a grid of positions with a 0.5 mm step. In order to identify the best alignment, the S2 position was used where the maximum number of coincidence signals among all the grid positions was found. The procedure to calculate the number of coincidence signals will be described in the following sections. Figure 4.5 shows an example of the best detector alignment, achieved for the grid position (1,1).

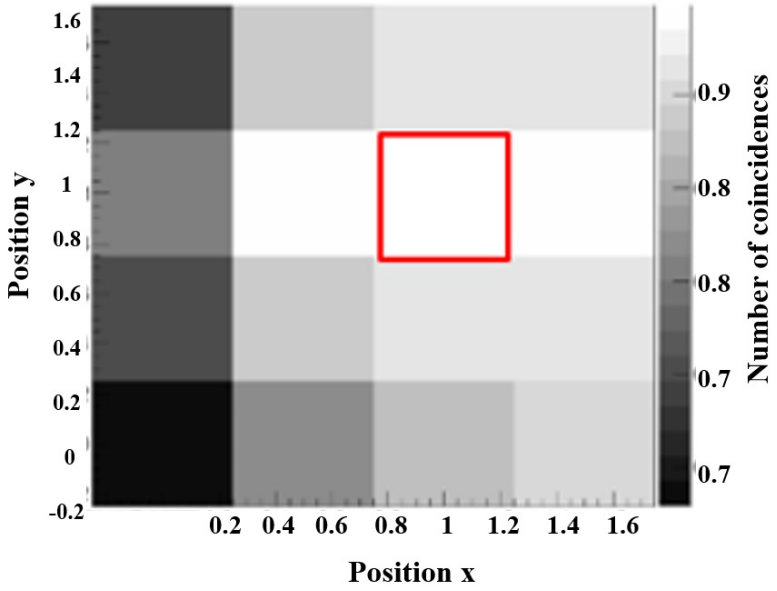

Fig. 4.5: *The grid of coincidence signals from scanning S2 to find the best sensors alignment. The position (1,1) achieved the maximum number of coincidences. Positions are expressed in mm.*

After the alignment, the sensors were irradiated at that specific distance with all the mentioned energies. In each run, from 5000 to 15000 waveforms were acquired from the digitizer, corresponding to a total acquisition time of around $3-9$ *s* respectively. In fact, with increasing the sensors distance, the beam irradiation time was increased to compensate for the lower efficiency.
The proton beam energy was extracted from the measured TOF value. To this aim, several systematic effects and a system calibration approach (described in sections 6.1 and 6.2) were considered. Finally, the measured proton beam energy was compared with the nominal one.

4.2.2 The beam test at TIFPA using thinned strip sensors

The same experimental setup described for CNAO was used for the clinical proton beam energy measurement at TIFPA. All the steps such as data acquisition and analysis, the applied system calibration and comparison of the results were repeated in the same way as the beam test at CNAO.

For the beam test at TIFPA, two thinned UFSD3 sensors described in Chapter 2 were mounted on the telescope structure and two strips per sensor were bonded on the HV distribution boards as for the CNAO test. Five nominal proton beam energies were considered (70-228 MeV) at a beam fluence rate of $10^6 - 10^{10} p/cm^2.s$. For each considered energy, the two sensors on the telescope were positioned at three different distances (27, 67, 97 cm). Pictures of the beam setup is shown in Fig. 4.6.

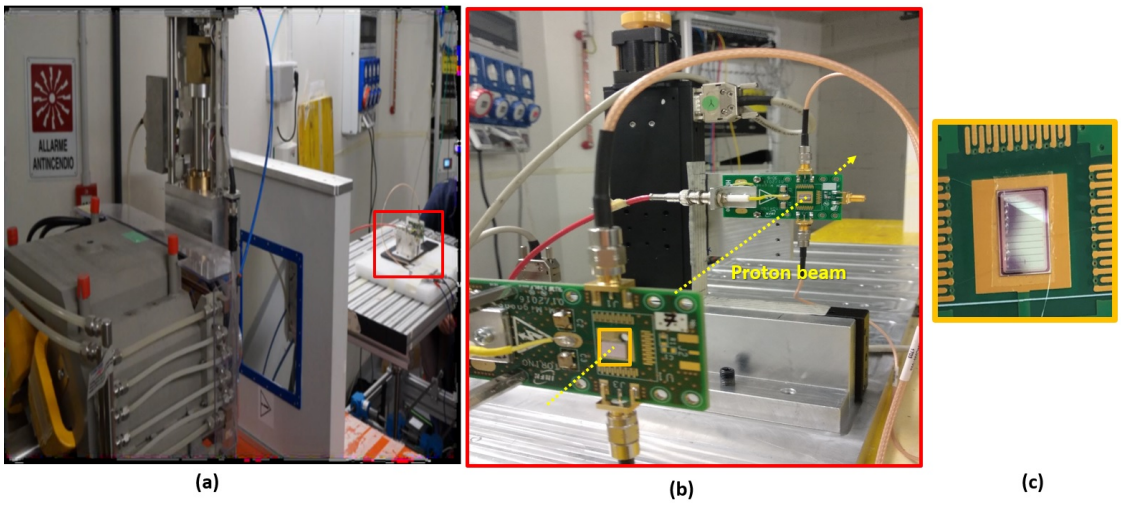

Fig. 4.6: *The setup of data acquisition from a beam test conducted at TIFPA. a)The telescope structure with two sensors to obtain the TOF. b) The focus on the telescope structure. The sensors bonded on the two dedicated HV passive board. c) The thinned UFSD3 segmented to 11 strips with total thickness* 120μm *and* 50μm *active thickness.*

4.2.3 The beam test at CNAO using thinned strip sensors

The last experimental measurement was done in CNAO using the thinned UFSD3 where the data read out using the final front end board reading out the 8 central strips of sensor (Fig. 4.8). This configuration (8+8 strips) allows reducing the time needed to align the sensors and the acquisition time to collect the required statistics, also speeding up the process of the beam energy evaluation. A dedicated readout board with amplifier has been designed to allow the reading of eight strips in the final sensor (Fig. 4.8).

The two sensors on the telescope were positioned at the distances (460 and 1060 mm). For each distance the sensors were irradiated with the proton beam energy 62.28 MeV, 147.72 Mev and 226.91 MeV, at a beam fluence rate of $5 \times 10^8 p.s^{-1}.cm^{-2}$.
The 8+8 channels connection to the digitizer, the movable stage for the S2 transversal movement and the rigid horizontal support with the corresponding grooves for setting the S2 position are shown in Figure 4.8.

The 8+8 signals acquired by the digitizer are internally divided in two groups. Each group is composed by a DRS4 chip and one ADC, able to store and digitize up to 9 signals in 1024 samples with 12 bit of resolution [95]. The Analog to Digital conversion of the data stored in the two chip DRS4 should start synchronously. However, a time jitter was observed between the two groups, which lead to unexpected peaks in the time difference Δt distribution histogram(Fig. 4.7,left). To overcome this problem, four channels of each sensor were connected to the same group of digitizer, thus, instead of 64 combination, 32 combination of strips only were considered for data analysis (Fig. 4.7,right). The final double Gaussian is thinner than in the left side case, obtaining coincidences only between 4.9 ns up to 5.1 ns and the maximum of the peak is located in the expected value of 5 ns. 32 combination is explained in better detail in chapter 6.

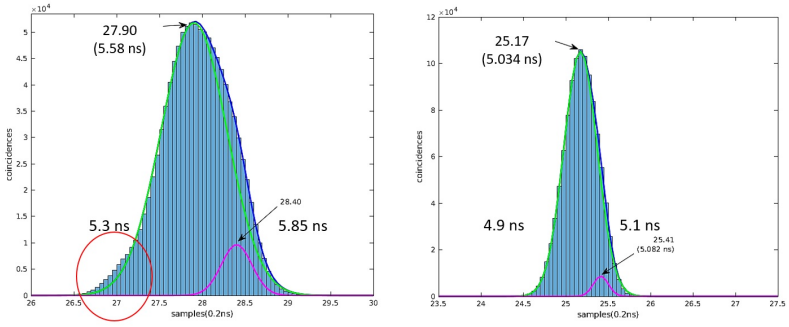

Fig. 4.7: *Time synchronization issues in the digitizer for 5 ns of delayed signal and the software trigger. Left: channels connected to different group of digitizer. Right: channels connected to the same group of digitizer.*

Fig. 4.8: *The setup of data acquisition from a beam test performed at CNAO. (a) General view of all setup, the yellow arrow shows the beam direction, (b) The telescope of the sensors in distance 1060 mm, (c) The digitizer with 16 readout channels to collect the data from 8+8 strips, (d)the front-end read out board, and (e) the thinned sensors segmented to 11 strips.*

4.3 Time of flight measurement

In the TOF technique, the particle kinetic energy is determined from the particle arrival time to the detectors set at a specific distance. TOF technique is a method which has been applied in various Nuclear and Particle physics fields. Examples are the keV-energy ion range measurements in Elastic Recoil Detection Analysis [99], proton residual energy after transmission through the target volume in proton therapy [100], and investigation on the quark-gluon structure of matter for the HERMES experiment in the HERA particle accelerator [101]. Moreover, TOF is well known as a technique to determine the ion composition in space plasmas [102] and space applications [103].

In this study, the TOF technique is used to determine the therapeutic proton beam energy. The difference between the calculated proton energy and the nominal one provided by the hadron therapy centers will be reported in terms of range deviation.

When one particle crosses S1 and S2, at the times t_1 and t_2, with known distance L between S1 and S2 and $\Delta t = t_2 - t_1$, the velocity can be calculated as:

$$v = \frac{L}{\Delta t} \tag{4.1}$$

Similarly, the particle kinetic energy can be calculated by Equation 4.2 .

$$K = E_0 . \left(\frac{c\Delta t}{\sqrt{c^2 \Delta t^2 - L^2}} - 1 \right) \tag{4.2}$$

where c is the light speed and E_0 is the rest mass of the proton.

In this chapter the method to obtain the TOF from arrival time of protons to sensors during data acquiring in CNAO and TIFPA will be described. Two approaches to measure TOF from the arrival times stored during the signals processing will be presented.

4.4 Identification of coincidence signals

During the irradiation of UFSDs, the signals from channels of the sensors were amplified by a CIVIDEC amplifier and acquired with a digitizer. Figure 4.9 shows an example of 200 samples corresponding to 40 ns waveforms from the digitizer acquired in one of tests conducted at CNAO at energy 103.5 MeV and distance 7 cm between the detectors. The peaks are in coincidence if they are separated by an amount of time approximately similar to the TOF obtain from Equ. 4.2, where the consider distance and proton energy putting in the formula. We were always choosing time windows of 10 ns to classify peaks as possibly coincident.

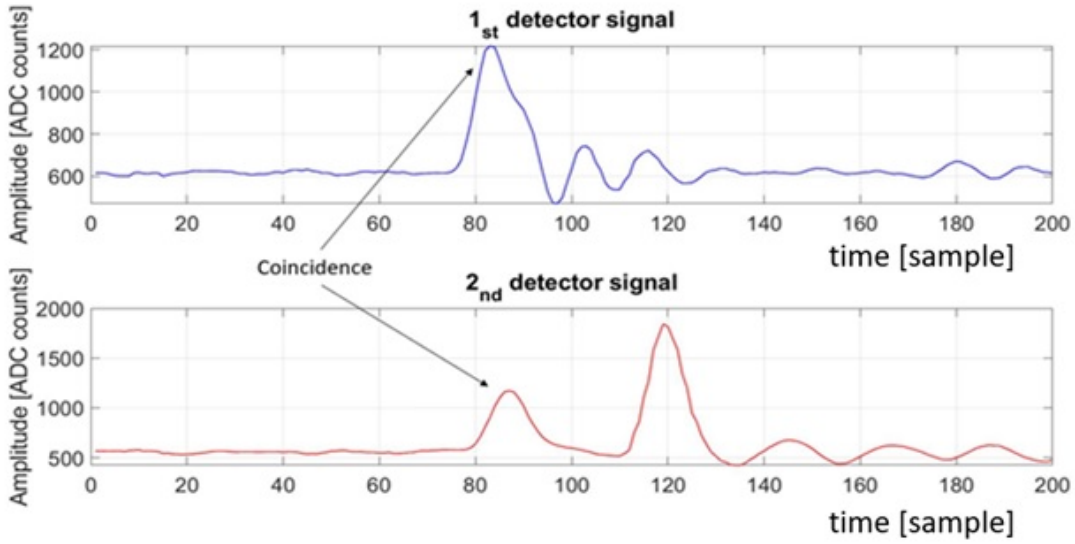

Fig. 4.9: *200 samples (40 ns) acquired from a test conducted at CNAO at 103.5 MeV. 7 cm of distance between the two detectors. The arrows indicate two peaks generated by the same proton crossing the two detectors (coincidence peak).*

As mentioned before, the signals acquired by digitizer were used to extract the coincidence signals and consequently to obtain the TOF. These raw signals need to be transformed by subtracting the baseline due to the setup of digitizer.
The most repetitive value in the signals was recognized as a baseline and was subtracted from all signals amplitudes of the waveforms collected by digitizer. A threshold value was defined to optimize the separation of the signal of protons from noise [104], and once the signal overcome this value, the peak was detected. An example is reported in Figure 4.10 where the threshold has been set at 200 ADC counts.

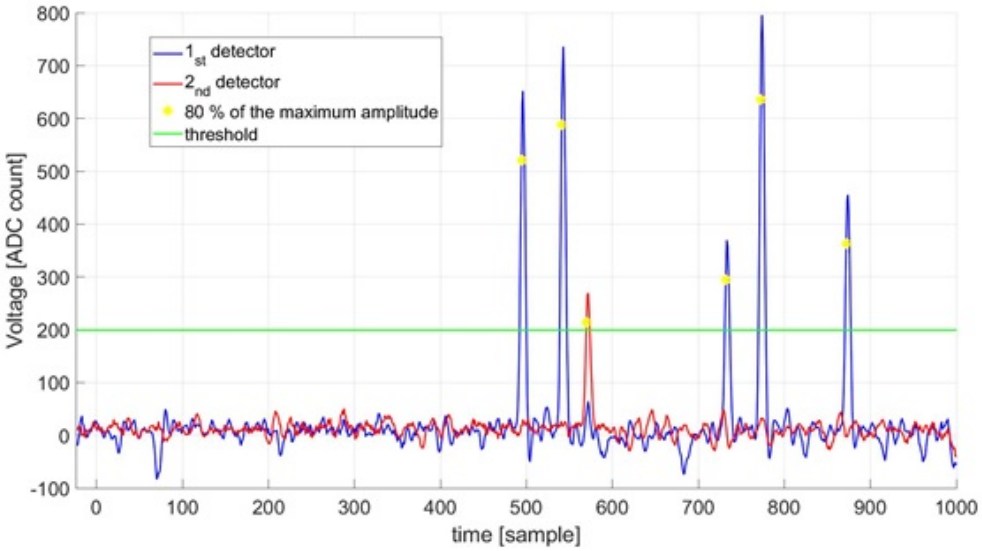

Fig. 4.10: *One event of the data acquired at TIFPA, with beam energy 182.8 MeV and 970 mm distance between S2 and S1.The yellow star marks the point of the 80% of the maximum amplitude of each peak.*

Due to the statistical nature of the energy deposition process, amplitude fluctuations were observed in the signals, which follow the Landau distribution described in section 5.1. The time distribution of the particles in each detector mainly depends on the beam structure and beam energy (see Fig. 4.15 and 4.16). Referring to the Bethe-Bloch formula (Equ.1.1), the average signal amplitude of the peak depends on the beam energy, therefore, the smaller the energy the larger the amplitude of the peaks.
To minimize the dependence of the measured time on the signal amplitude, the Constant Fraction Discriminator (CFD) algorithm was applied to reconstruct the time of arrival t_i of each discriminated signal i [74].
In the CFD method, the arrival time is determined when the amplitude reaches a percentage of the maximum value of the peak. The CFD method reduces the time walk effect, defined as the effect that consists in bigger signals overcoming a given threshold earlier than smaller ones (Figure 4.11).

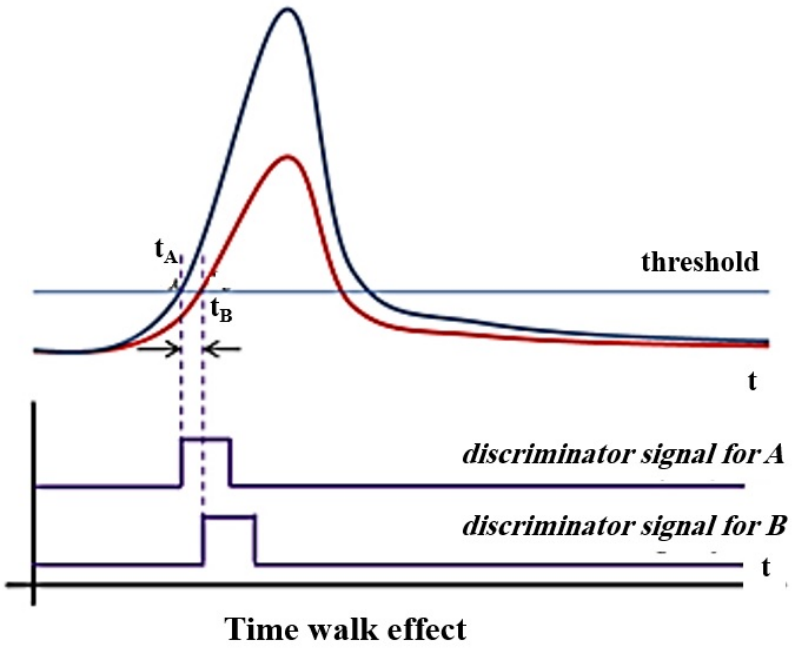

Fig. 4.11: *Two peaks with different amplitudes crossing the defined threshold at different times (time walk effect, due to the physics of signal formation).*

In this framework, the value of the fraction of the maximum amplitude of the signal was set at 80% to allow the time calculation even in the presence of partially overlapping peaks (Figure 4.10, the yellow marks). It should be noticed that the most probable value of the peak amplitude increases by lowering the beam energy because of the larger energy loss in silicon. Thus, the signals shown in Fig. 4.14 (related to the 228 MeV beam) in comparison with the signals in Fig 4.10 (related to the 182.8 MeV beam) are examples of the smallest peak amplitudes among the signals acquired during the test at CNAO, with the fluctuations due to the statistical nature of the charge production in silicon.

There are two problems during reading the signals: pile-up and jitter. When different protons cross the detectors in the same time or in a time interval smaller than pulse time duration, pile-up of the two peaks can occur. In this situation there is a peak during the fall of the previous one. Figure 4.12 presents an example of pile-up.
The jitter term is related to the time uncertainty caused by the early or late firing of the comparator due to the presence of noise on the signal itself or in the electronics. It is directly proportional to the noise of the system [74]. Figure 4.13 focuses on the jitter effect on a peak over the threshold that affects signal. Both pileup and jitter give rise to the appearance of multiple peaks very close in time.

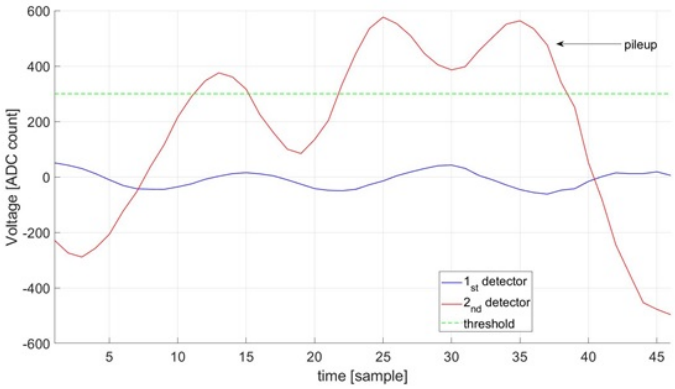

Fig. 4.12: *An example of pileup condition in the signal of the second detector.*

We distinguished pile-up from jitter using the second derivative of the waveform. When there was overlap of two pulses and the difference between concave down of first pulse and concave up of the second pulse was one sample it was identified as jitter. In cases the difference was ≥ 2 samples, this pulse was identified as pile-up and was rejected.

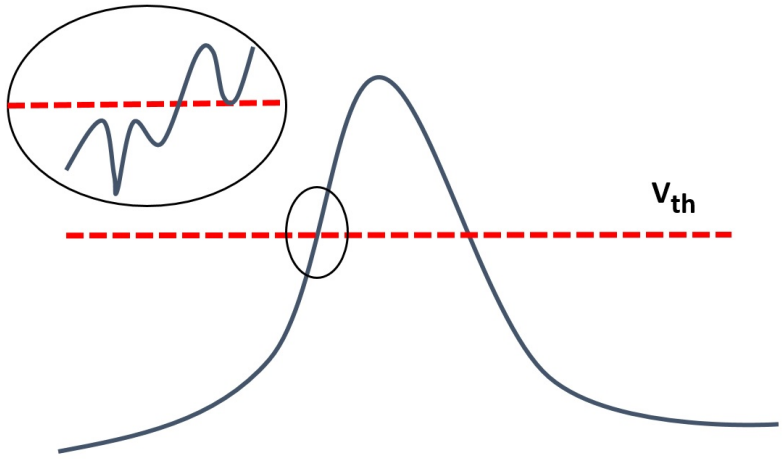

Fig. 4.13: *The effect of noise on signal knows as Jitter effect.*

4.5 The mean time difference Δt_{mean} measurement

The first step to determine the average time difference Δt_{mean} was the measurement of t_1 and t_2, the exact time which the proton passed the S1 and S2. For each proton signal in S1, the related coincidence signal generated by the same proton passing through S2 should be identified.

The data analysis was performed using the MoVeIT tool(chapter 5), where all the functions for data reading, processing, and the output were implemented.
In order to identify the coincident signals, for each peak in the first sensor, a search for all possible coincident hits in the second sensor is performed. Within a search time window (10 ns corresponding to maximum flight distance) the hits in the second sensor with a time of arrival compatible with the estimated time difference are identified. Then the time difference between the two arrival times $(\Delta t = t_2 - t_1)$ for each of the candidate coincidence signals was stored for later analysis.

An example of the signals acquired during the measurement test at CNAO is depicted in Figure 4.14. The coincidence signals of protons passing through both sensors and also single signals without a coincidence can be observed.

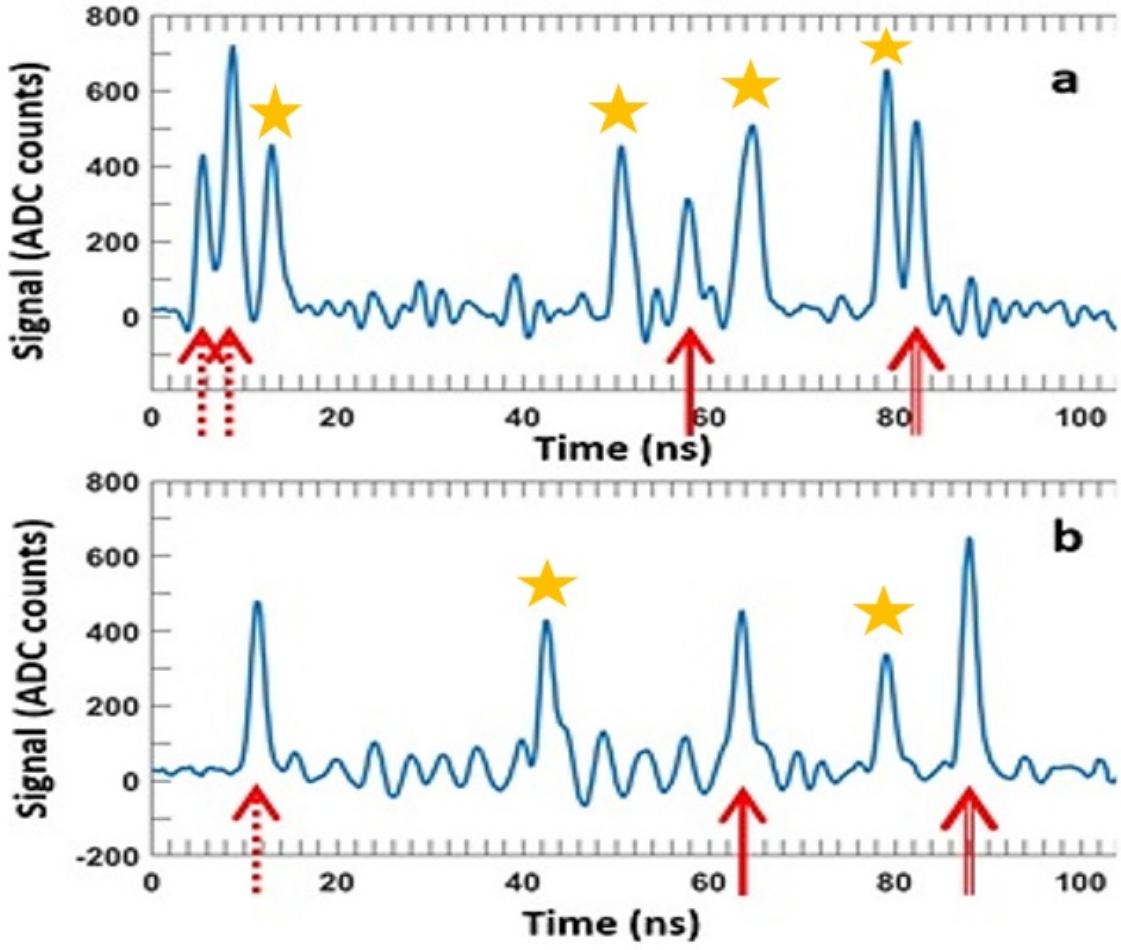

Fig. 4.14: *Example of two waveforms: a) from S1 and b) from S2 as acquired with the CNAO proton beam at 228 MeV and 97 cm distance between the two sensors of the telescope. Arrows of the same type in (a) and (b) point out the possible coincidence signals in the two sensors. The yellow stars point out the signals with no matching signal in the other sensor.*

For each peak over threshold in S1, a list of peaks in S2 within the selected time window was saved. Thus, for each peak in S1 with arrival time t_1, a list of $\Delta t_i = t_{2_i} - t_1$ was saved , where t_{2i} is arrival time of the i-th possible coincidence peak in S2.
Example of the histogram of the time difference Δt for all the possible coincidence peaks of two sensors obtained from measurement tests in TIFPA and CNAO is shown in Figure 4.18.

The difference between the Δt histograms is related to the different time structure of the beam provided by the accelerators (sec. 4.1). An example of time distributions of signal peaks identified when the two UFSDs were irradiated with protons at CNAO is shown in Fig.4.15. Due to the spill time (about 1 s) and inter-spill time of about 4 s in CNAO [106] in comparison with the acquisition time of 1000 events (205 μs) the continuous wave forms is observed in CNAO and results coincidence peaks all over that combinatorial background.

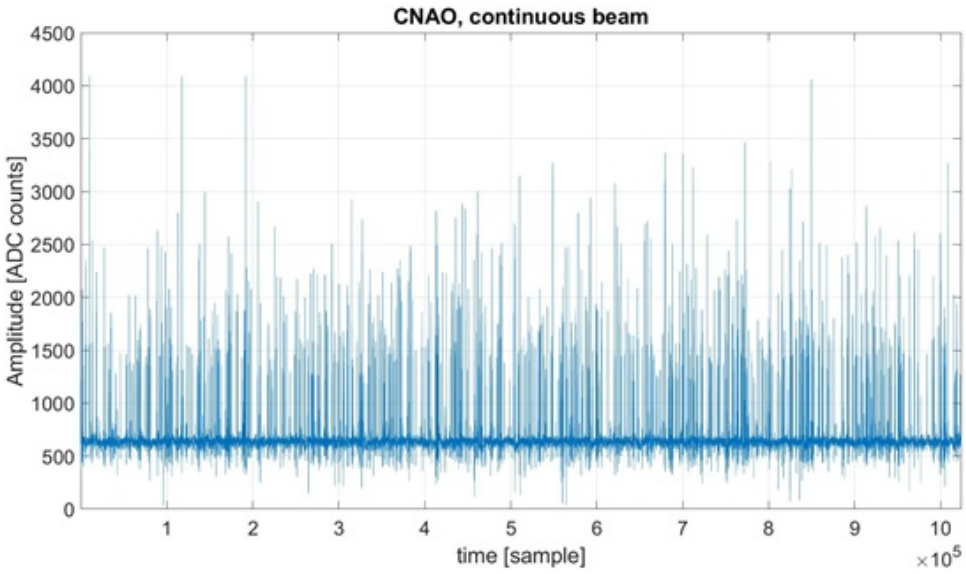

Fig. 4.15: *The continuous signal of 1000 events acquired in CNAO.*

The time distribution for TIFPA is shown in Fig. 4.16. This periodic structure correspond to a beam irradiation occurring periodically with a period of 20 ms and a duty cycle of 50 % [91]. The proton extraction is synchronous with the cyclotron revolution or RF, and the protons are always provided in a short time interval with respect to the RF phase. The radiofrequency at which the particles are emitted is about 100 MHz with period of 10 ns. Consequently, every 5 ns (25 samples), there are particles coming from the accelerator. This can be observed in Fig. 4.18, where the coincidences are spread over

an interval of about 20 samples (around 4 ns). Enlarging the considered time window for the TIFPA, further peaks are visible due to the 10 ns period radiofrequency (Fig. 4.17). Those secondary peaks entirely rely on combinatorial background. It leads to the shape of the histogram of the coincidence signals in TIFPA (Fig. 4.18)
These two plots (Fig. 4.15 and 4.16) were obtained by stitching together 1000 waveforms with all the deadtimes in between.

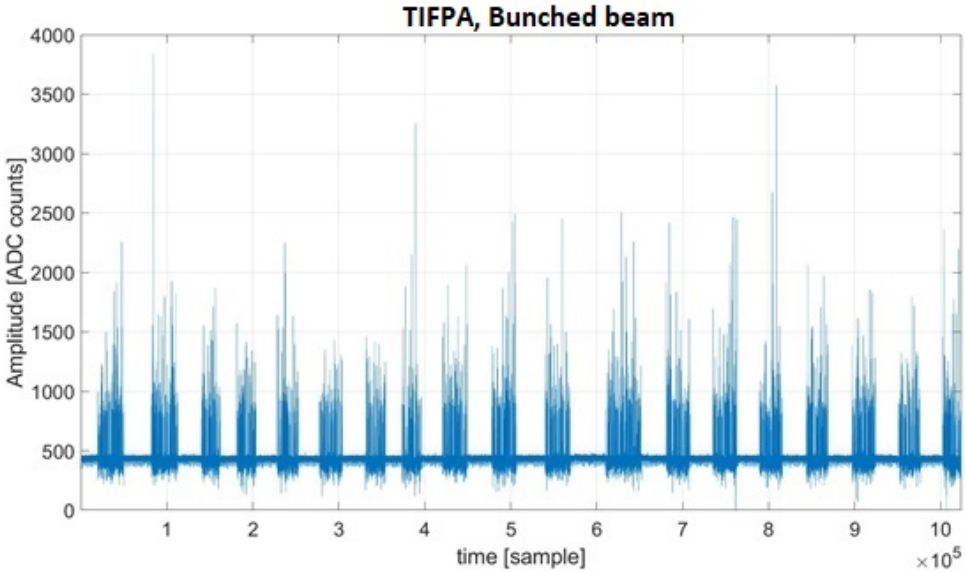

Fig. 4.16: *The bunched signal of 1000 events acquired in TIFPA (first detector). The signals between two successive bunches, are below the threshold.*

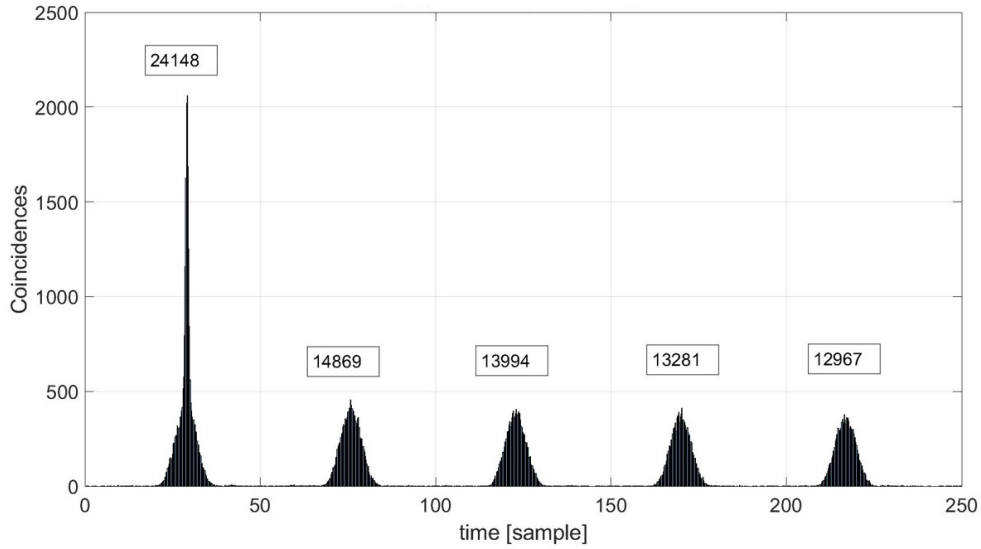

Fig. 4.17: *Radio frequency peaks in signals acquired in TIFPA, with the relative number of coincidences collected.*

Based on Figure 4.18, background of false coincidences (almost flat for CNAO and causing the widening at the base of the peak in TIFPA) must be statistically subtracted. To this aim, two method were developed to statistically subtract the false coincidence signals and obtain the time difference Δt value: 1) 3-sigma method, 2) second Gaussian method. It should be considered that the error over the TOF will affect the proton beam energy measurement (section 4.6).

The first step in both methods was performing a fit with the sum of two Gaussians over the histogram of Δt, it is shown in Figure 4.18 red curve, resulting in a Gaussian curve of the peak and a second Gaussian curve of the background. After doing the double Gaussian fit, the two mentioned methods were applied on the histogram as follows.

4.5.1 Method 1 (3-sigma method)

In this method, an interval of 3-sigma ([-1.5 sigma; 1.5 sigma]) around the maximum of the histogram (Gaussian curve of the peak fit in first step) was identified and a single Gaussian fit was implemented over this interval. The Figure 4.18 is an example of implementation of the 3-sigma method and Figure 4.19 shows the zoom of single Gaussian fit on CNAO histogram. The width of the peak in the distribution of the time difference values (Δt), as shown in Figure 4.19 allows the estimation of the time resolution for the single crossing as $\sigma_{\Delta t}/\sqrt{2}$. Depending on the radiation energy time resolutions for the single crossing were found between 75 ps and 115 ps. These values are in good agreement with the results from other measurements for sensors with a thickness of 80 μm [60]. For sensors with a thickness of 50 μm, the time resolution for the single crossing were found between 48 ps and 97 ps for 1 m flight distance.

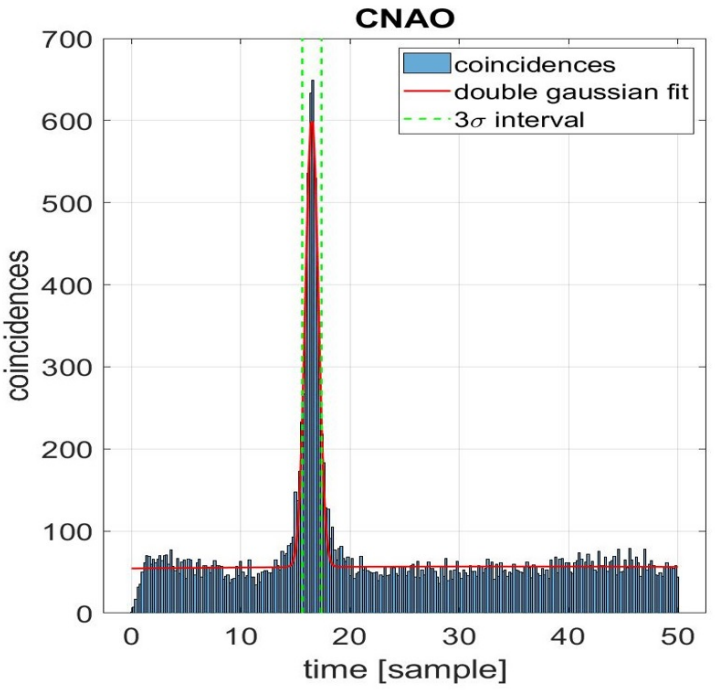

(a)

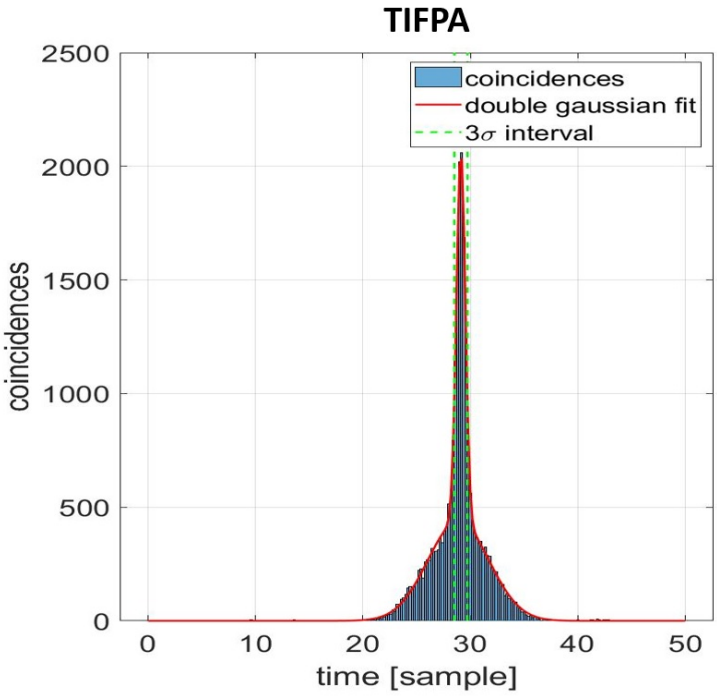

(b)

Fig. 4.18: The histogram of the time difference Δt for all the collected coincidences a) The experimental test conducted at CNAO, energy 77.6 MeV, distance 37 cm. b) The experimental test conducted at TIFPA, energy 182.8 MeV, distance 97 cm. The first method (3-sigma method) is applied to both histograms to statistically subtract false coincidence peaks. The green dashed lines represent the upper and lower limit of the interval(3σ). The coincidences within the 3σ interval are considered for the final fit.

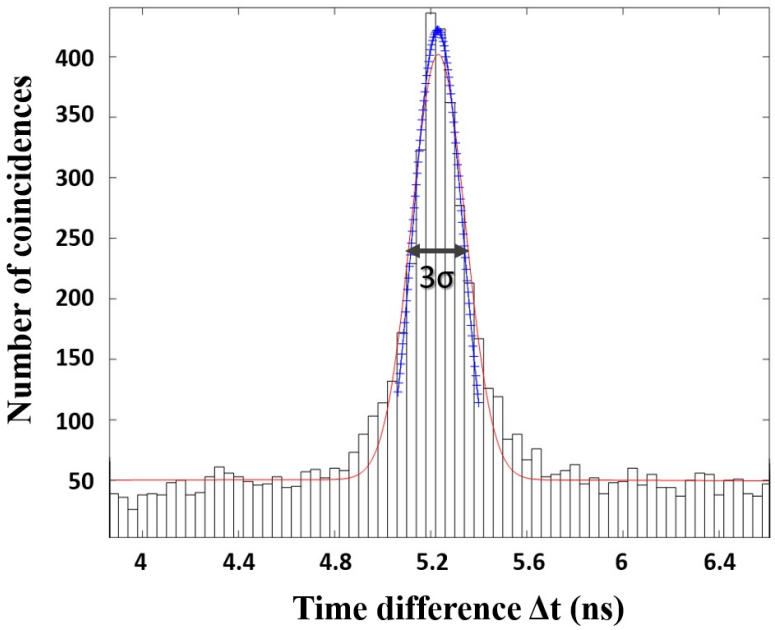

Fig. 4.19: *The zoom of Δt distribution on CNAO histogram. The red line shows the first fit (double Gaussian) and the blue line is the additional Gaussian fit for Δt values within 3σ, performed to estimate the final time difference Δt_{mean} value. In this case $\Delta t_{mean} = 5.229 \pm 0.003 ns$. [107]*

Referring to Figure 4.18, by applying the 3-sigma fit, a distortion of the coincidence peaks in the base of the histograms can lead to the less precise determination of the mean time difference Δt_{mean}.

4.5.2 Method 2 (second Gaussian method)

Let's go back to the first step (double Gaussian fit). In this step the different characteristics of beam in CNAO and TIFPA affected the shape of the second Gaussian (Fig. 4.18). In the second method, after statistical subtraction of the combinatorial background coincidences from the time difference Δt histogram, a single Gaussian fit was repeated (Figure 4.20).

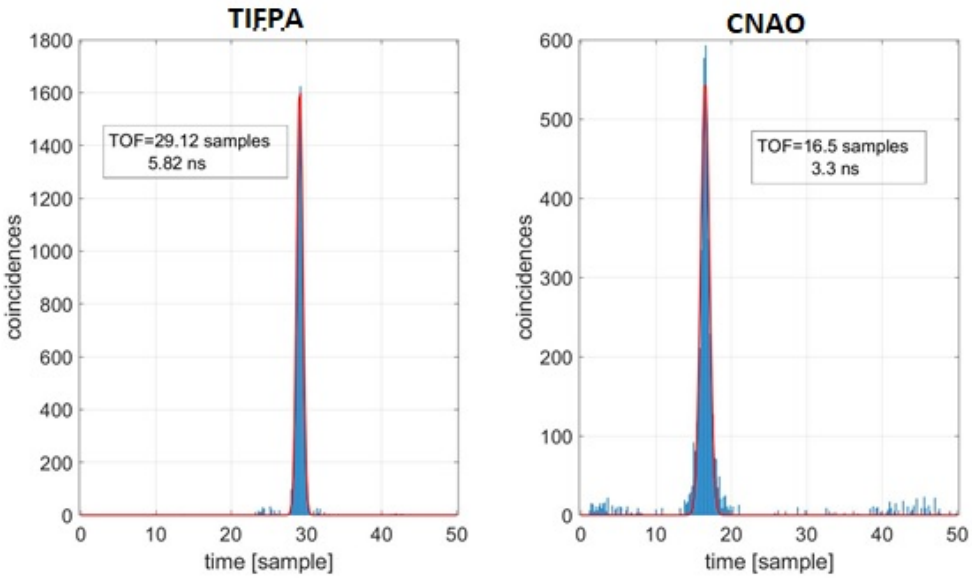

Fig. 4.20: *Second Gaussian method, final single Gaussian fit over the left coincidences after statistical subtraction of the combinatorial background coincidences from the time difference Δt histogram.*

The limitation of 3-sigma method is the false coincidences that are still present at the base of the main peak of the time difference histogram. In general, the difference between the results of two methods would not be appreciable on a nanoseconds scale. However, the statistical error on the average measured TOF is mostly of the order of few ps or even smaller, therefore a systematic effect related to the background subtraction can impact on the measured energy.

The Δt_{mean} value that was obtained from one of the two mentioned methods was used to determine the proton beam energy as described in the following.

4.6 The Energy Measurement Using the Time of Flight

The 2D projection of the telescope system for proton beam energy measurement using TOF technique is shown in Figure 4.21. The procedure of proton beam energy measurement is described briefly in the following.

The proton measured TOF at specific beam energy and distance between sensors d was defined as equation 4.3, where $offset$ is a constant time difference mainly due to the routing of the electronic chain and Δt_{mean} is the mean difference of the coincidence signals times of arrival in the two sensors which obtained as described in section 4.5.

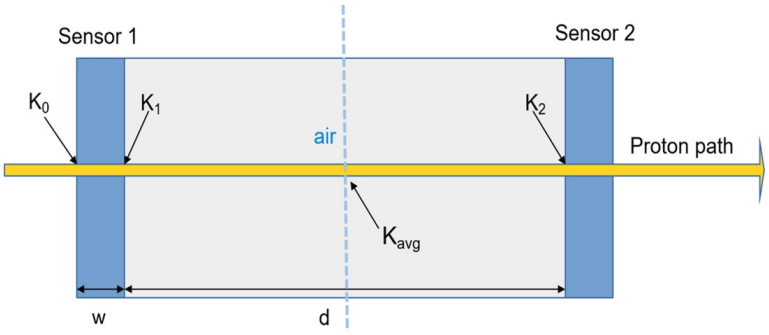

Fig. 4.21: *2D projection of the telescope structure made by sensors S1 and S2, with thickness w, at a specific distance d in air. K_0 is the proton kinetic energy which enters the telescope at the isocenter. The silicon thickness of S1 reduces the energy to K_1. Due to the air between two sensors the kinetic energy decreases to K_2 at the entrance of S2. K_{avg} is the average kinetic energy obtained from the TOF.*

Under the assumption of constant air stopping power $(\frac{S}{\rho})_{air}$ between the S1 and S2, the mean kinetic energy K_{avg} in the central position was determined from the average velocity v_{avg} equation 4.4 and the equation 4.5. Considering the energy lost in the S1, the proton beam energy at the isocentre K_0 for specific distance d between sensors with thickness w, was obtained as equation 4.7 , where $(\frac{S}{\rho})(MeV.cm^2/g)$ and $\rho(g/cm^3)$ are the mass stopping power and the density of silicon and air. To account for the mass stopping power in the air and the first sensor, the method proposed by [108] was used.

$$TOF = \Delta t_{mean} - offset \tag{4.3}$$

$$v_{avg} = \frac{d}{TOF} \tag{4.4}$$

$$K_{avg} = E_0 \left(\frac{1}{\sqrt{1 - (\frac{V_{avg}}{c})^2}} - 1 \right) \tag{4.5}$$

$$K_1 \approx K_{avg} + \left(\frac{S}{\rho}(K_{avg}) \right)_{air} . \rho_{air} . \frac{d}{2} \tag{4.6}$$

$$K_0 \approx K_1 + \left(\frac{S}{\rho}(K_1) \right)_{Si} . \rho_{Si} . w \tag{4.7}$$

To optimize the energy measurement procedure, the $offset$ and distance d in Equ.4.3 and 4.4 need to be determined accurately. To meet this goal, the system should be calibrated

in terms of $offset$ and distance d. Two system calibration approaches were investigated and are explained in chapter 6. The final result after applying the system calibration methods are reported in the result chapter.

Figure 4.22 represents the sequence of operations to obtain the proton beam energy. In this case, corresponding to the final setup at CNAO, the data acquired by digitizer from 16 channels of two sensors mounted on the telescope structure. The waveforms from S1 and S2 were analyzed via computational MATLAB tool that is described in chapter 5. The Δt_{mean} was extracted according to the histogram of coincidence signals and different arriving time. Finally, the proton beam kinetic energy was calculated using the equations 4.3 to 4.7 as function of Δt_{mean}, d, $offset$.

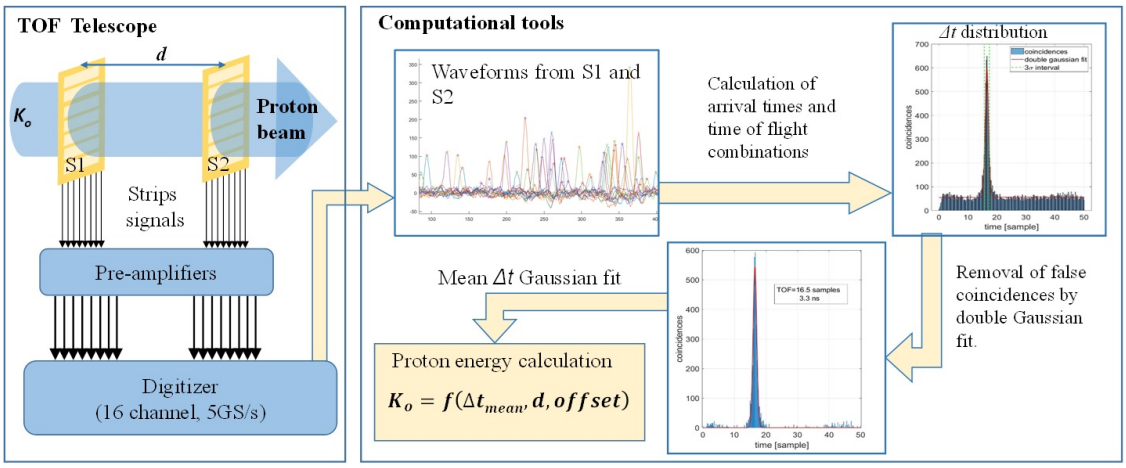

Fig. 4.22: *The chain of proton energy measurement. 16 waveforms from the two sensors which positioned at a specific distance from each other collected by the digitizer. The Δt_{mean} extracted from a Gaussian fit on the coincidence signals. Finally, the proton kinetic energy at isocenter is extracted from the measured TOF.*

Chapter summary

This chapter gave a review of the experimental measurements in proton therapy facilities (CNAO and TIFPA) to measure the proton beam energy using TOF technique and UFSDs. The experimental setup and all the requirements were presented and discussed. The chain of the coincidence signals identification , the TOF measurement, and the overall behaviour of the data was assessed. In addition, the review of the energy measurement from the TOF and related parameters was examined. In the following chapter, this acquired data will be used for the system calibration to find the optimized value of the proton energies.

Chapter 5

Reconstruction and analysis of wave forms of UFSD strips

> "Hell of simulation, which is no longer one of torture, but of subtle, maleficent elusive twisting of meaning..."
>
> Jean Baudrillard, Simulacra and Simulation

As presented in the previous chapter, in order to increase the number of signals in coincidence and the corresponding statistics and efficiency, the data will be read out from several strips (at most 8+8 channels). On the other side, due to the huge amount of data from 16 wave forms, developing the analysis program is essential.
To this purpose, a computational tool for timing has been developed using MATLAB software called "MoVeIT tool". The MoVeIT tool allows also to simulate the wave forms used to test the reconstruction analysis. To simulate the 16 waveforms, preliminary files are required: the simulation of protons passing through both sensors in different flight distances coming from GEANT4 [109] and the WEIGHTFIELD2 freeware used to shape the sensors peaks [110]. Finally, the TOF and proton energy were determined as mentioned in sec. 4.6. In this chapter we will present all the details about MoVeIT tool.

5.1 MoVeIT tool for wave forms simulation

5.1.1 GEANT4 simulation

The first input required for the signal simulation comes from GEANT4 simulation. The GEANT4 simulation was used a) to simulate the efficiency of coincidence accounting for the effect of multiple scattering in the first sensor and in air between the two sensors, b) to simulate the time difference accounting for the energy loss in silicon and in air. This input file contains all the information about interaction between each proton and detectors. GEANT4 simulations were performed for 10^6 protons with a specific Gaussian distribution of the flux with five energies (62, 105, 150, 180, 227 MeV), and for each energy, different distances between two sensors from 0.1 mm to 1000 mm. S1 was modeled as silicon sensor of 11 strips, positioned at 0,0 (isocenter). To simulate several positions for S2, the detector was modeled as a volume of sensitive air of the same size of S1 at 15 positions as shown in Figure 5.1 as red vertical lines, just to record the position of the hit of the protons if a detector was there. The main GEANT4 output is a matrix including the particle ID (a number that identifies each specific particle), the coordinates (x, y and z) at which particle is crossing each of detectors, energy and time of flight required to cover that distance from the position 0. The three coordinates are:

- z : the distance from the origin (isocenter, along the proton original direction);
- y : the position along the height of the detector;
- x : the position along the width of the detector.

By knowing the coordinates of particle and dimension of sensors, it is possible to find in which strip the proton is going through, depending on the sensors alignment. This allows to test the alignment procedure and check the systematic effect related to it. All the above details are the input for wave forms simulation using MoVeIT tool.

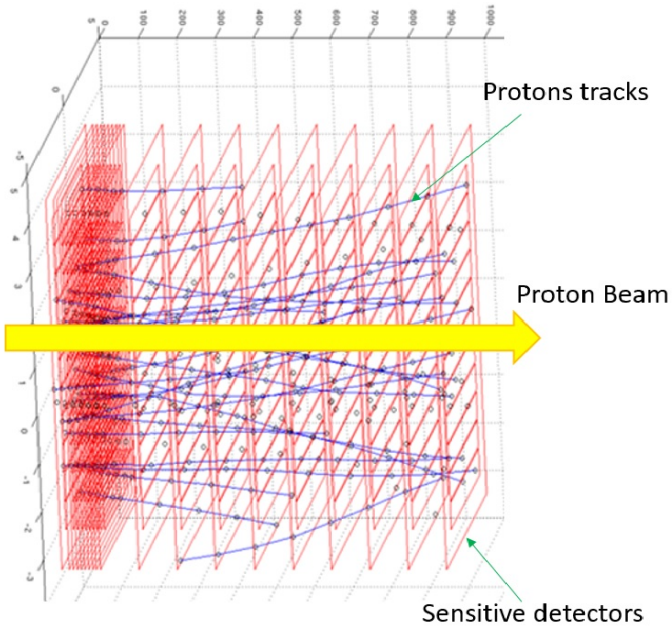

Fig. 5.1: *Simulated protons (blue curve) going through detectors at 15 different location (red vertical lines). The z-axis represents the distance of the detector from the isocenter at 0, while the y-axis goes along the height of the detectors. This is an example of one of the simulation conducted in GEANT4.*

5.1.2 WEIGHTFIELD2 simulation

The second input for wave form simulation is the shape of the signal peaks generated by UFSD sensors and read out amplifier. To this aim we applied the WEIGHTFIELD2 program. WEIGHTFIELD2 [111] [112] is a 2D simulation software for UFSD silicon detectors developed in Turin. It is based on an existing program called Weightfield, developed by HEPHY in Vienna, which is used to simulate the signal in a silicon detector with microstrip or pad geometry and has been extended to simulate the effect of the gain layer. This program is implemented in the C++ language and uses the ROOT graphical interface. The graphical interface allows the user to select simulation parameters such as the type of incident particle, sensor geometry and doping, depletion and bias voltages, the details of the output electronics, and to display drift and weighting potentials, current signals, and the voltage output (Figure 5.2).

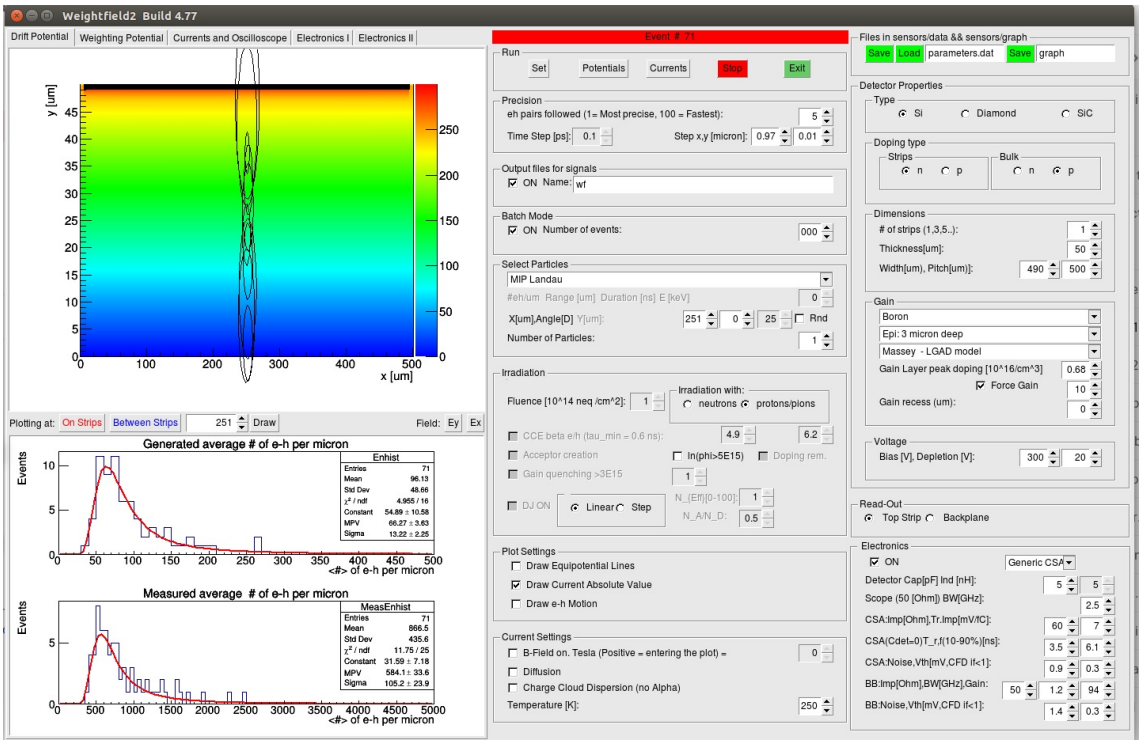

Fig. 5.2: *Interface of WEIGHTFIELD2 program to simulate the energy released by an incoming particle in silicon detector.*

Figure 5.3 shows an example of the charge production mechanism and current output provided by WEIGHTFIELD2 for a UFSD diode of 50 μm thickness and gain 10. When the ionizing particle crosses the depletion region, primary electron-holes pairs are produced and migrate toward the electrodes. The contribution of the primary holes (blue curve in Fig.5.3 right) in the current signal decreases while they are collected in the p+ electrode. The charge multiplication occurs while the primary electrons reach the high field region of the p+ gain layer. At this moment the additional electron-holes pairs are created. Both the primary and secondary electrons are collected by the n+ electrode giving a small contribution to the output current (red and pink curves). The contribution of the secondary holes to the current signal (light blue curve) increases until all the electrons reach the gain region and then it decreases while the holes migrate toward the p+ electrodes and are collected. The overall signal duration is a little more than 1 ns.

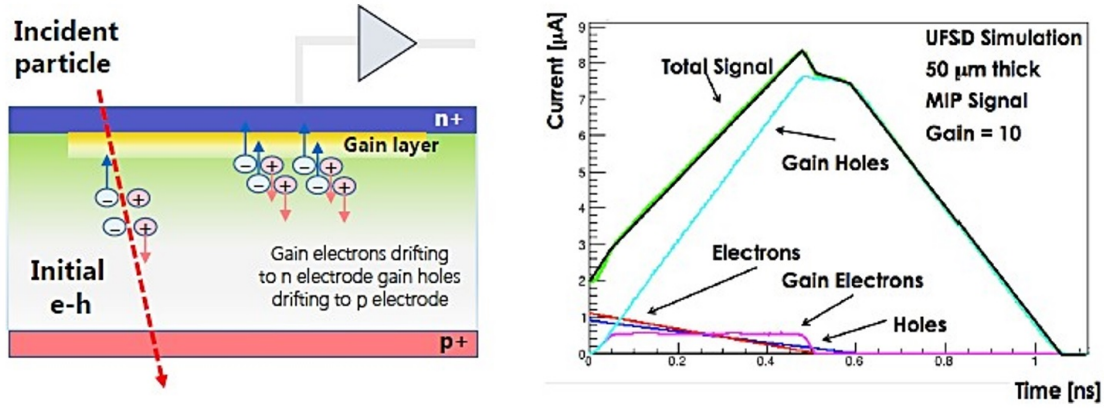

Fig. 5.3: *Left: charge migration inside a UFSD detector; Right: contribution of different carriers to the UFSD output current.*

A set of 1000 current signals was generated with a length duration of 2 ns using WEIGHTFIELD2. Fig. 5.4 shows the amplitude distribution histogram of these current signals normalized to the maximum amplitude. We simulated the particles crossing the device with Landau distribution of the particle energy where there are a lot of particles with low and medium energies and a few of them with high energy that creates the tail at very high energy in the Landau distribution. Those two signals that are very large, represent some particles that cross the sensor which belongs to that high energy tail of landau distribution. They generate higher signals but while the large majority of the particles are generating signals that are medium and low and it belongs to the first part of distribution around the most probable value.

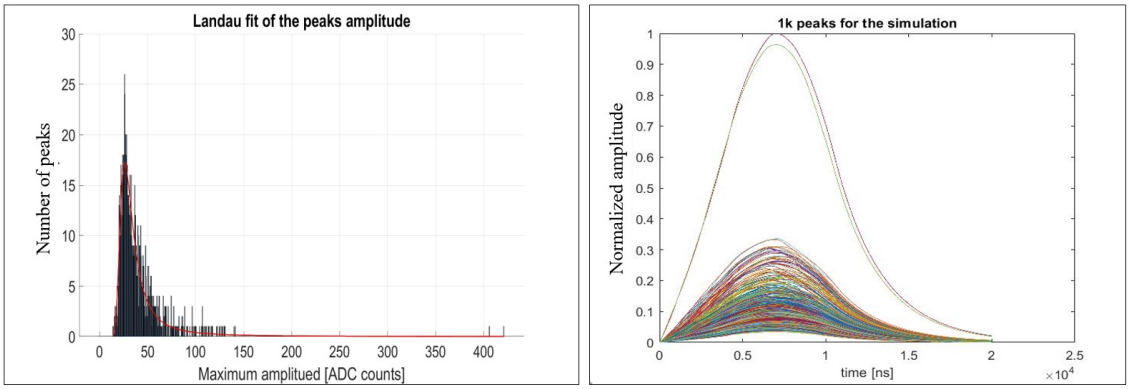

Fig. 5.4: *A set of thousand simulated peaks with WEIGHTFIELD2, histogram collecting the amplitude of each simulated peak, the red line is the Landau fit of these points (Left), normalized respect to the maximum amplitude (Right).The amplitude is expressed in ADC count of the CAEN digitizer.*

5.1.3 Wave forms simulation

MoVeIT tool was developed for wave forms simulation and for the analysis of the data obtained from simulation or experimental beam tests. All the required parameters for wave forms simulation and data analysis are defined in MoVeIT tool interface.

In order to generate a waveform, a pulse sequence according to the time structure of the real proton beam is generated sampling from a Poissonian time distribution. 16 base lines (8 per detector) are first generated by MoVeIT tool with a random noise distribution where peaks will later be added. Based on the proton beam energy and the distance between sensors selected from the interface of program, the corresponding GEANT4 output is selected and for any generated peak inside the pulse sequence, the MoVeIT tool selects from the file the proton which was passing through the S1 in that time and generates a peak in the waveform of the S1 channel modeled according to the WEIGHTFILED2 simulation and, if the selcted proton hits the sensor S2, the corresponding peak is added to the waveform of the the S2 channel. The difference between arrival time of the same proton in S1 (t_1) and S2 (t_2) i.e. the TOF and is also saved inside the program. All these steps are repeated to simulate the peaks corresponding to 10^6 protons that were used for GEANT4 simulation. Since there were 8+8 strips, a matrix of 64 TOF values and number of coincidence peaks, due to the combination of strips are saved. Finally, the proton beam energy was determined using the mean TOF and the procedure explained in section 4.6.

Figure 5.5 shows the screen shot of MoVeIT tool interface. The input files are included: Proton info file and Waves info file which call GEANT4 and WEIGHTFIELD2 outputs respectively. It also allows to choose properties such as position of sensors, noise level, time offset, pulse rate and number of events. The simulated waveforms window according to the number of event selected by user is shown in this part. Two output files contain 16 simulated wave forms (8 per detector), information of the TOF, number of coincidence peaks and the measured proton energy based on the equations described in section 4.6, and are saved for later analysis.

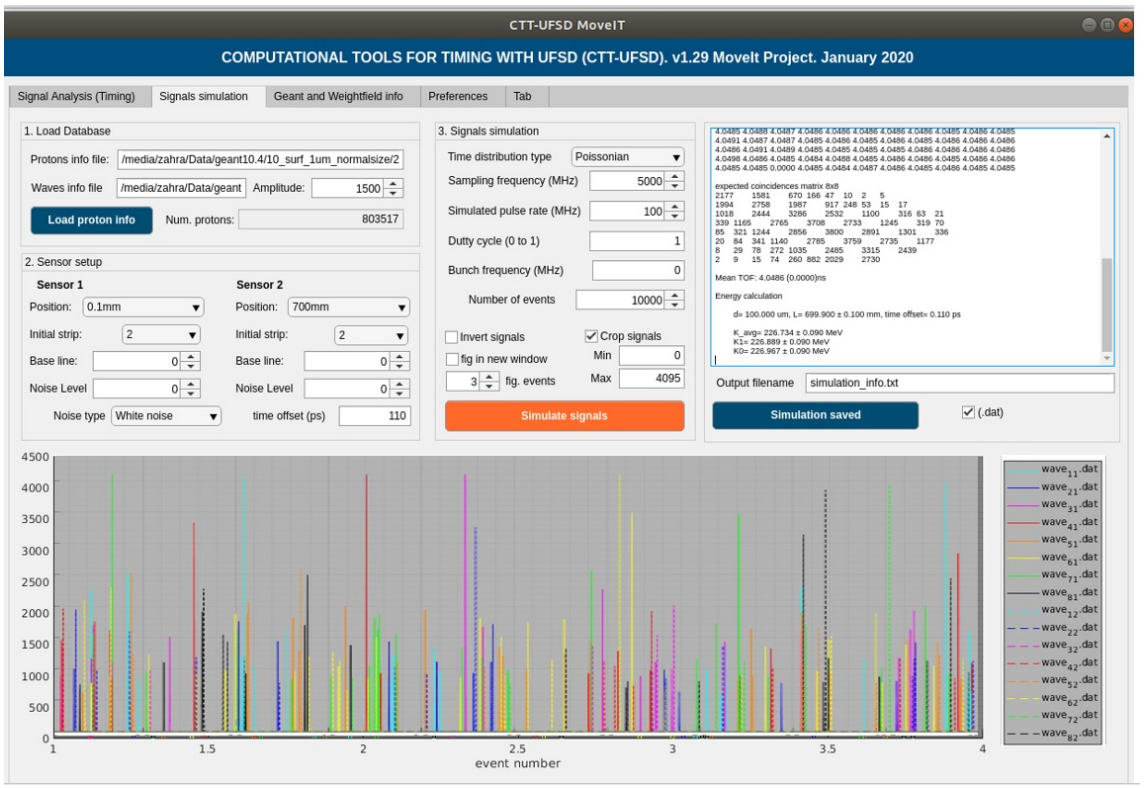

Fig. 5.5: *The screen shot of MoVeIT tool. The wave forms simulation for the proton beam energy 227 MeV, where the distance between sensors 700 mm and time offset 110 ps were defined. This simulation was done for 10000 events.*

5.2 MoVeIT tool for wave forms analysis

For any wave forms analysis we used the signal analysis part of the MoVeIT tool (Figure 5.6). The input files can be either the simulated wave forms or the wave forms which were collected by digitizer during the experimental measurement.

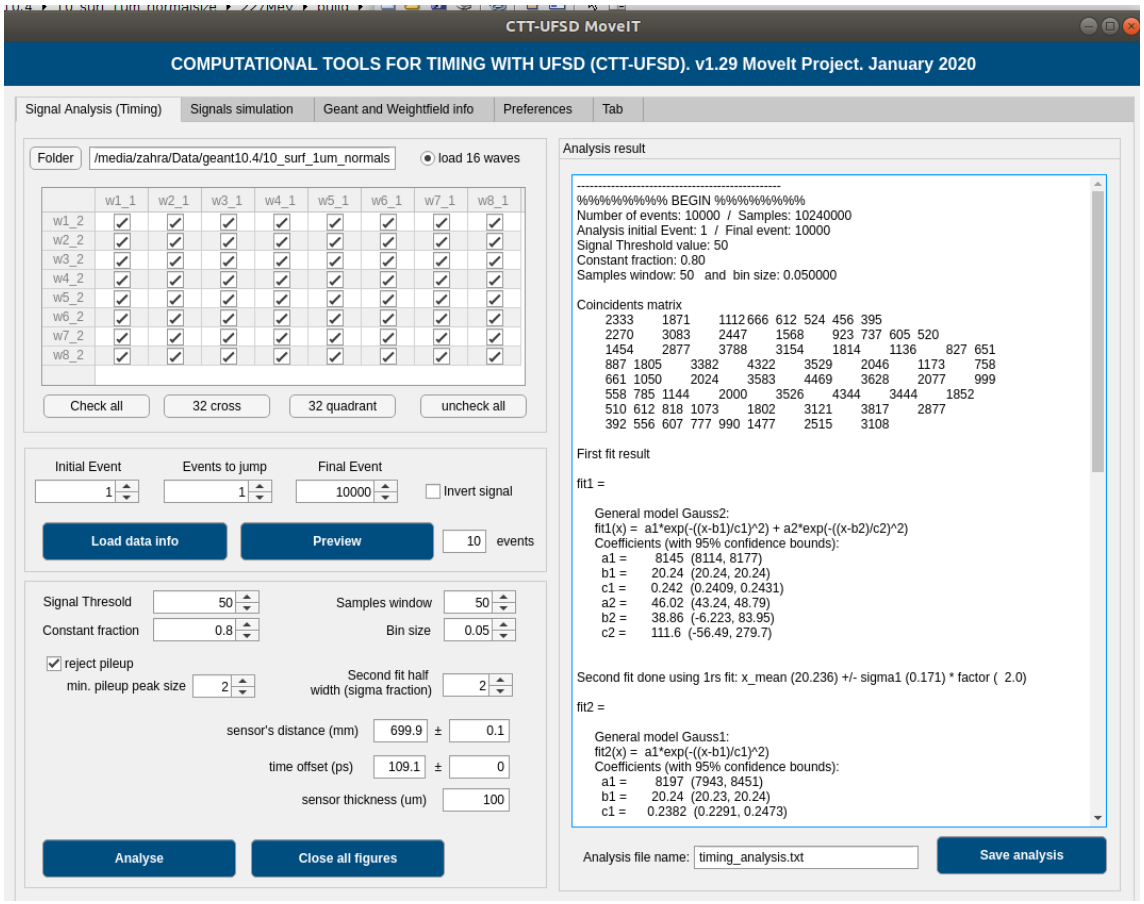

Fig. 5.6: *Interface of the analysis part of the MoVeIT tool.*

As depicted in Figure 5.6, a matrix is shown where the rows represent the channels of the first detector and the columns represent the strips of the second one. By checking the related boxes it is possible to define the combinations to be considered in the later analysis. In present thesis four coincidence combinations schemes were used for the wave forms analysis which are shown in Fig.5.7.

- All 64 combinations (Fig.5.7 a).
- 32 cross; due to the time synchronization issues in the digitizer (section 4.2.3) the data were read out from these combinations of strips (Fig.5.7 b).
- The facing strips; only the coincidence signals from facing strips were considered for the wave forms analysis (Fig.5.7 c).
- One combination; only the coincidence signals from one strip of each sensor (the same strip) were considered for the wave forms analysis (Fig.5.7 d).

After selecting the desired combination, the related wave forms are recalled and once a peak is detected in any strip of S1 the code checks if there is any coincidence peak in any strip of S2 and stores it. The procedure applied to identify the coincidence peaks was described in detail in section 4.4.

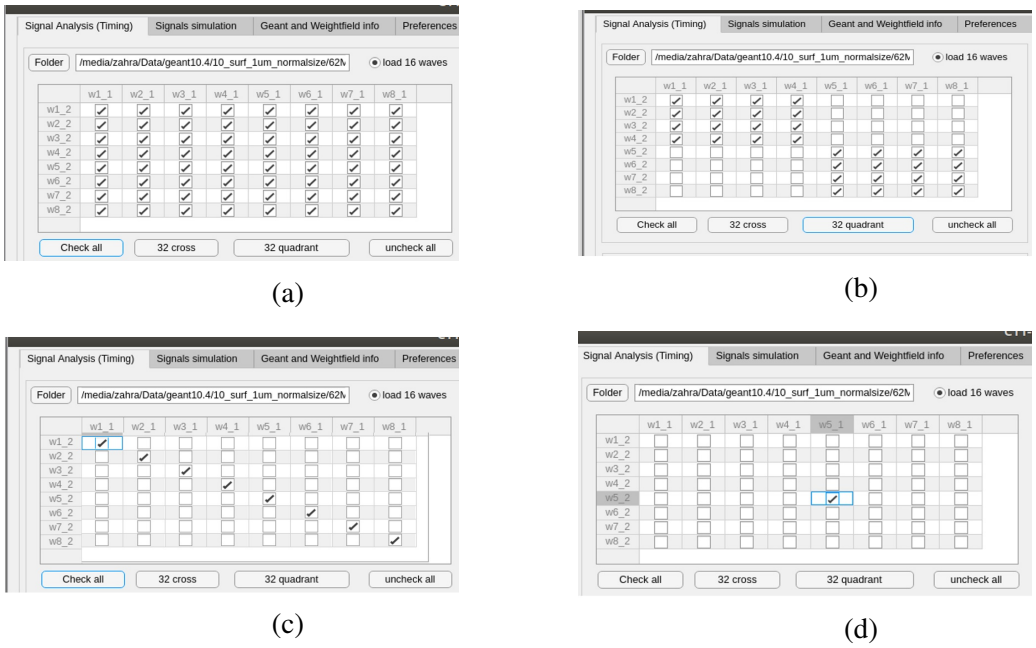

Fig. 5.7: *Different combinations of strips were defined by checking the related boxes in the MoVeIT tool interface to analysis the coincidence signals. a) 64 combinations, b) 32 cross combinations, c) facing strips combinations and d) one strip combination.*

Figure 5.8 shows an example of the distribution of number of coincidence signals for simulated wave forms (8+8 strips), where S2 was positioned at 40 cm (Fig. 5.8 a) and 100 cm (Fig. 5.8 b) and the sensors were irradiated with protons of 227 MeV energy. As expected, the largest number of coincidences are over the main diagonal region (the facing strips) and decreases going to the peripheral area. This behaviour indicates that the larger probability is the particle passing from the specific strip of S1 and reaching the same strip in S2.

When S2 is positioned at 40 cm, the maximum number of coincidences is 7000 Out of 10000 generated events, distributed around the main diagonal of matrix. When S2 is positioned at 100 cm, the diagonal pattern is less pronounced, and the number of coincidences reduces to 2500. In the larger distances such as 100 cm, divergence of the proton beam leads to broader coincidence signals distribution in the central area of the matrix. Therefore, to obtain accurate TOF (and consequently proton beam energy), it is essential to select the best combination that includes the maximum number of coincidences. All the

steps, from the coincidence signals identification to the proton beam energy measurement, described in chapter 4, were done using the analysis part of MoVeIT tool.

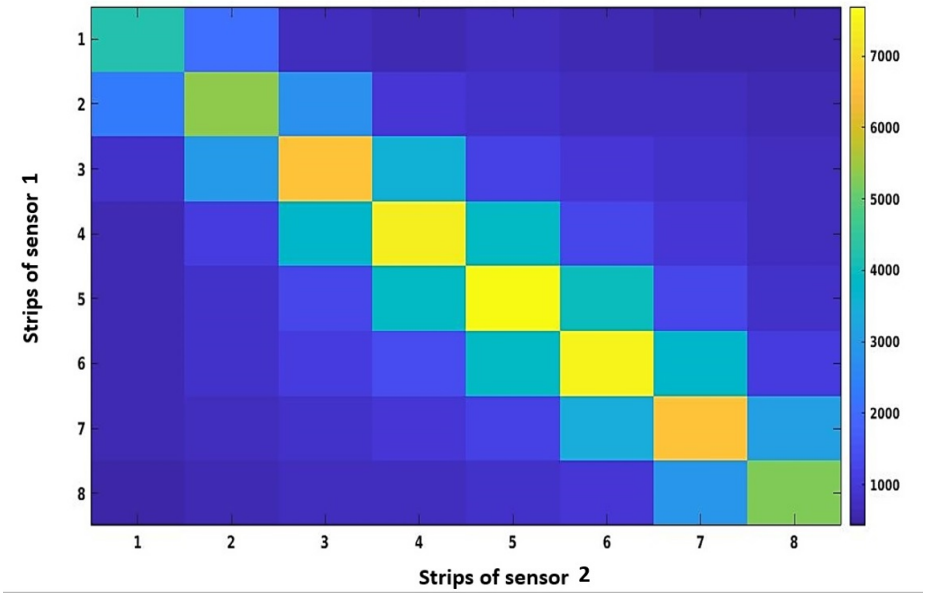

(a)

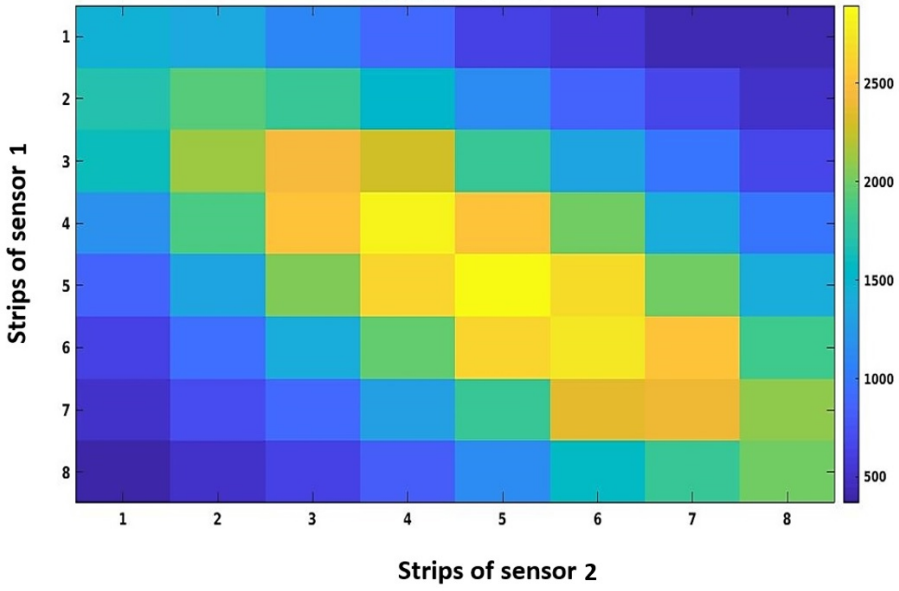

(b)

Fig. 5.8: *The distribution of coincidence peaks with S2 located at (a) 40 cm and (b) 100 cm and was irradiated with 227 MeV proton beam.*

In addition to signals simulation and signal analysis, two more parts have been developed inside the MoVeIT tool: 1) GEANT4 and WEIGHTFIELD2 info and 2) preferences.

1) GEANT4 and WEIGHTFIELD2 info section allows the user to change the positions of the sensors in X, Y and angle coordinates to evaluate the effect of the sensors alignment on the number of coincidence signals and accuracy of measured TOF without redoing the simulation by GEANT4 (Fig.5.9).

2) Preferences section allows the user to enter the digitizer specifications and other electronics information to obtain and process the waveforms during the experimental measurement in proton therapy centers.

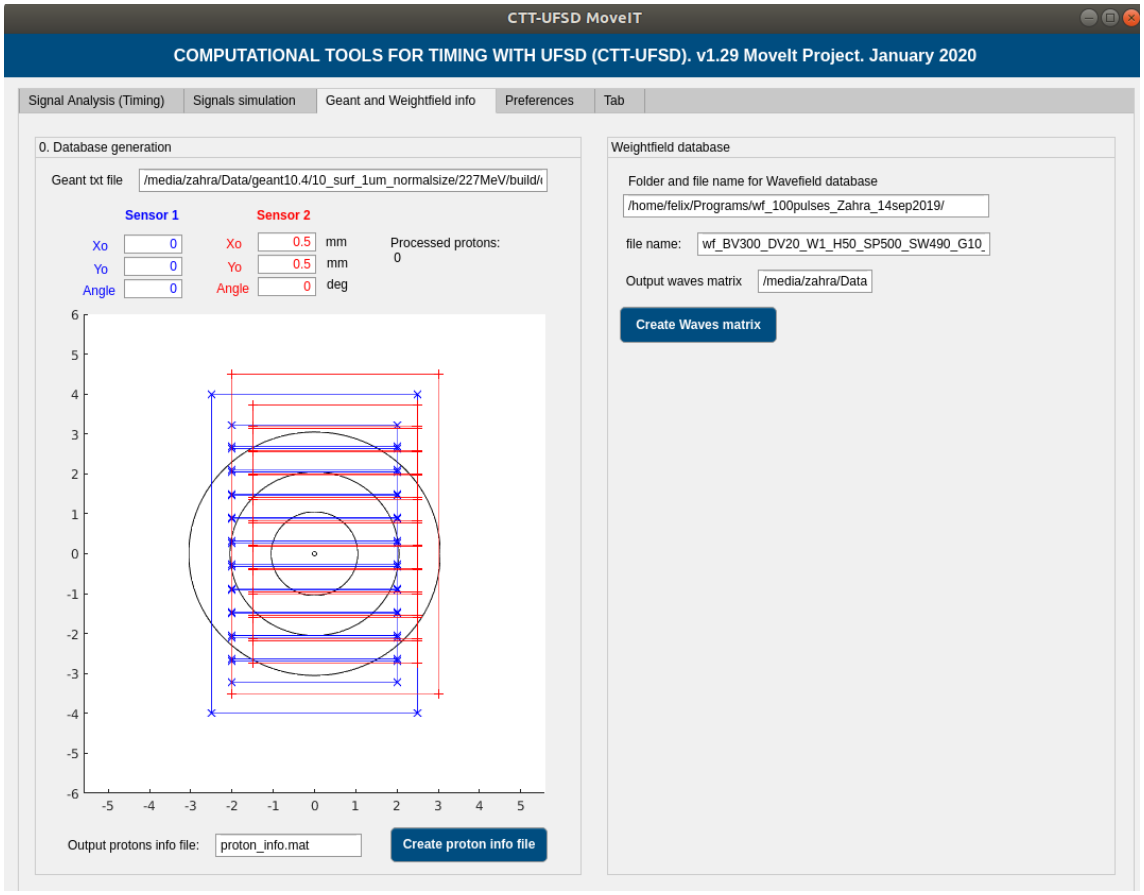

Fig. 5.9: *The interface of GEANT4 and WEIGHTFIELD2 info part of MoVeIT tool.*

Figure 5.10 presents the chain of the wave forms simulation using MoVeIT tool. This computational tool provides the possibility to simulate the wave forms according to the properties defined by the user.

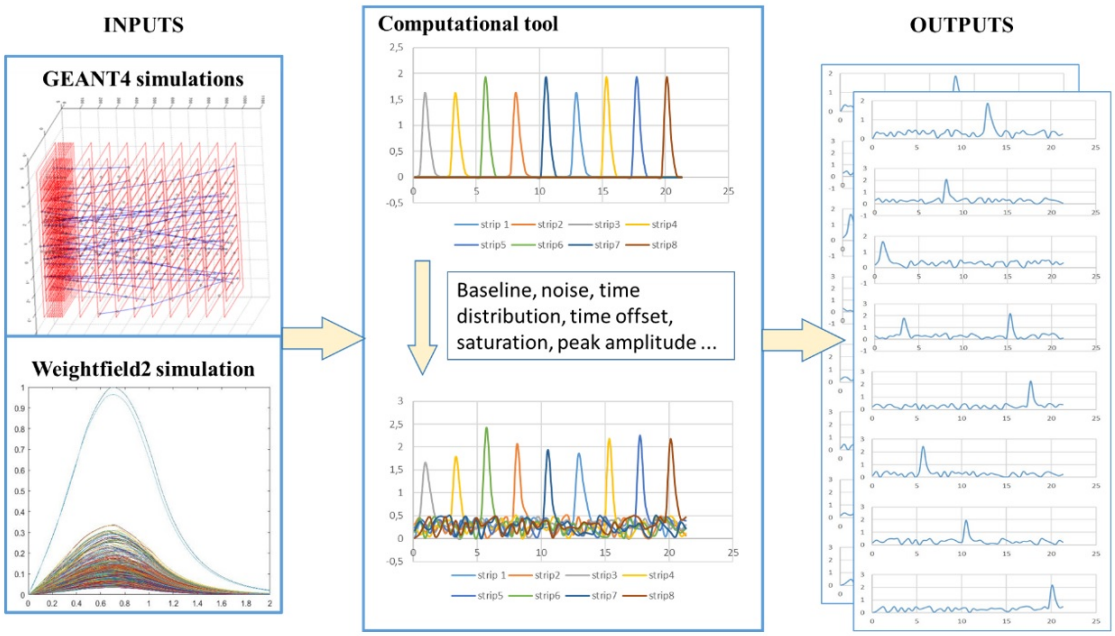

Fig. 5.10: *The procedure of simulating 16 wave forms from sensors (8 per sensor). All the properties of wave forms (Baseline, noise, etc.) defined by the user and incorporating with the required files from GEANT4 and WEIGHTFIELD2. The coincidence signals will be extracted from output files to obtain the TOF and consequently the beam energy measurement.*

Chapter summary

In this chapter the MoVeIT tool for wave forms simulation and analysis based on MATLAB software for measuring the proton beam energy using TOF technique was presented. The method of preparing the initial required files through GEANT4 and WEIGHTFIELD2 simulation programs were described. The explanation of all sections of MoVeIT tool and their capabilities was covered. Additionally, the interface of the program allows selecting options for wave forms simulation was presented. Furthermore, the examples of the distribution of number of coincidence signals for different distances between sensors were shown. All the possible strip combinations were presented and the data analysis to obtain the TOF and proton energy were discussed. These were the base to evaluate the systematic effect and the system calibration methods that were described in the next chapter.

Chapter 6

The systematic effects and the calibration approaches

> "Errors are not in the art but in the artificers."
>
> Isac Newton

The TOF approach relies on the identification of coincident signals. The main sources of uncertainty over the TOF measurement are the combinatorial error caused by multiple protons passing through the two sensors within the same TOF frame or hitting only one of the two sensors due to beam divergence, multiple scattering and misalignment of the sensors with respect to the beamline. Based on simulation studies, a good compromise between sensor size and travel distance must be chosen and a careful alignment system must be used to maximize the number of coincidences and keep the combinatorial error at acceptable levels.

In the previous chapters we described the method for the proton beam energy measurement using TOF technique. Furthermore we introduced the MoVeIT tool for wave form simulation and analysis. The MoVeIT tool was developed to validate the proton beam energy measurement method. As discussed earlier about the range limitation in clinic and the maximum acceptable error on the TOF, all the parameters which affect TOF accuracy should be evaluated.

This chapter will outline the evaluation of the systematic effects and introduce how they impact the TOF accuracy. An overview of the system calibration and two calibration methods will be presented and their characteristics will be given.

6.1 Simulation studies of systematic effects

The TOF measurement relies on the determination of coincidence signals. Thus, based on the simulation studies, a good choice of all parameters must be employed to maximize the number of coincidences and keep the combinatorial error at the acceptable levels. To meet this goal, many simulation studies were performed using MoVeIT tool which will be explained in the following.

6.1.1 Combination of strips

As mentioned earlier, signals from only one channel per detector were collected during the first and second experimental tests in CNAO and TIFPA. In the third experimental measurement, that was made in CNAO, we collected the wave forms from 16 channels (8 per detector), but due to the time synchronization issues in the digitizer (see section 4.2.3), only 32 cross combination (Fig 5.7b) and facing strip combination (Fig 5.7 c) were considered to analyze the data. In order to optimize the efficiency in the energy measurement, we need to choose the best combination of eight strips of sensors. It means we collect the data from 8 strips per detector but only the combinations with higher coincidences possibility should be considered. To this aim a number of 16 wave forms simulations were performed for proton of 227 MeV and 62 MeV, and distance between sensors of 40 cm and 100 cm for both energies were used. All the simulations were performed for 10000 events. The number of coincidence signals and the proton energy at isocenter K_0 were extracted and compared.

Fig 6.1 presents an example of the different combinations of strips which were simulated using energy of 62 MeV and distance of 40 cm and 100 cm. The number of coincidences is normalized to the number of coincidences of single strip combination.

The interaction of the proton beam with S1 leads to a deviation from the initial path, and together with the divergence of the proton beam along the path determines the decrease the number of coincidences in case facing strips combinations compared to the 32 cross combination.

In the ideal case, if all the 64 combinations were used the maximum efficiency of the system would be obtained. Therefore, because of the larger statistics, we would obtain the

most accurate measured beam energy in this combination.

Figure 6.2 shows the measured proton energy for different combinations in different distances. Considering the error bar for each combination it can be observed that there is no significant difference in result using the 3-sigma method and two Gaussian method to identify $\Delta tmean$.

Since the weight of the relative error of TOF in the energy measurement for large distance is much more than for the short distance, therefore there is a lower error on the measured energy at the large distance.

In addition, it is apparent that the largest error on the measured energy appears for the case with the minimum coincidences (facing strips and single strip combinations).

Although the number of coincidences in 32 cross combination is obviously different from 64, there is no significant difference between the measured energy and its error for this case. Therefore, due to the time syncronization issues in the digitizer, acceptable results can be obtained by using 32 combination instead of 64.

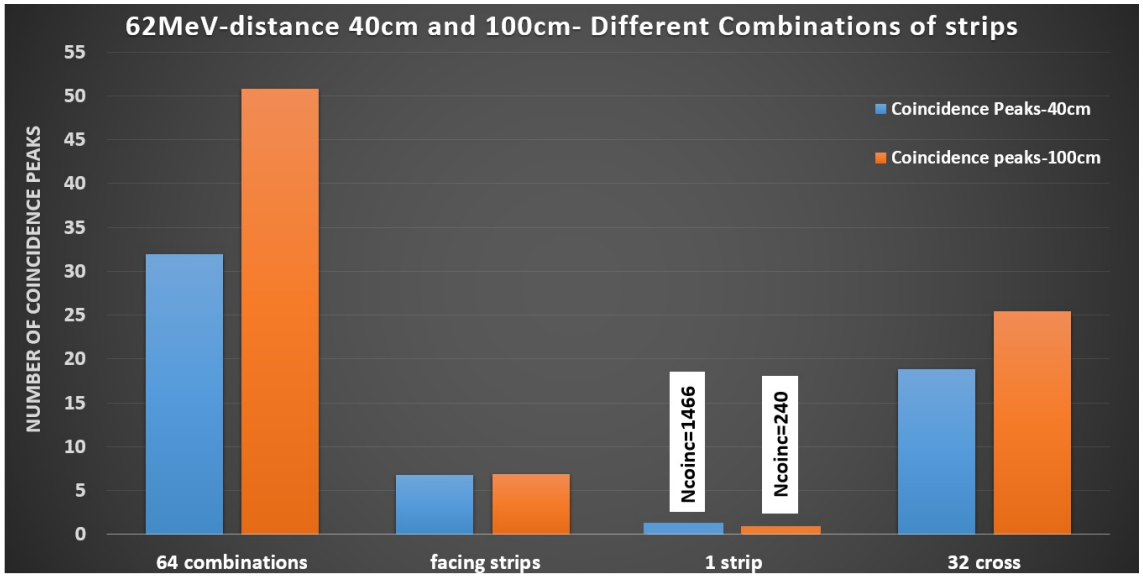

Fig. 6.1: *The number of coincidence peaks due to the different combinations of strips which are normalized to the single strip mode, for energy 62 MeV and distances of 40 cm and 100 cm.*

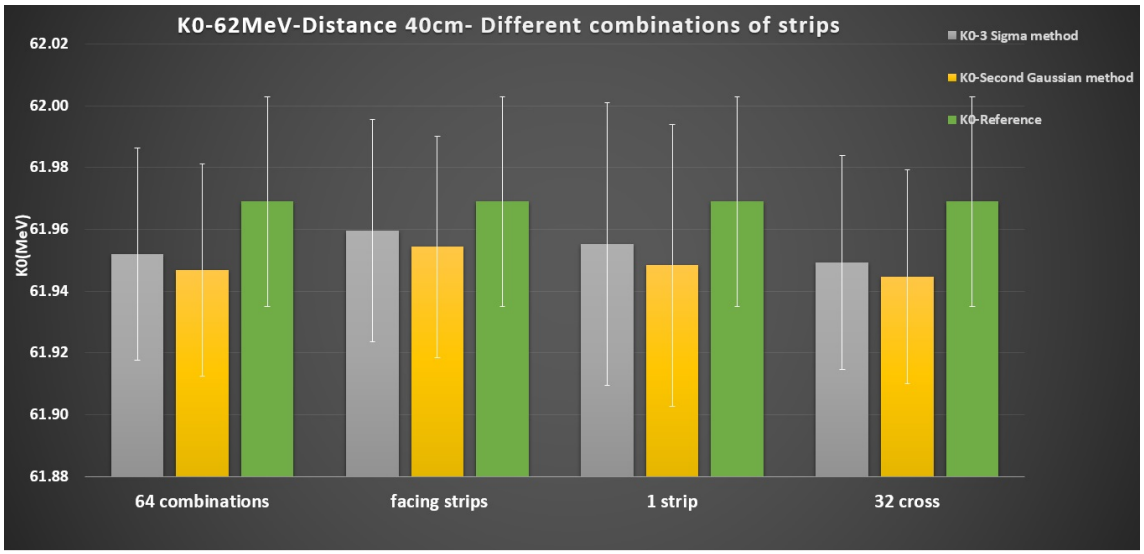

(a)

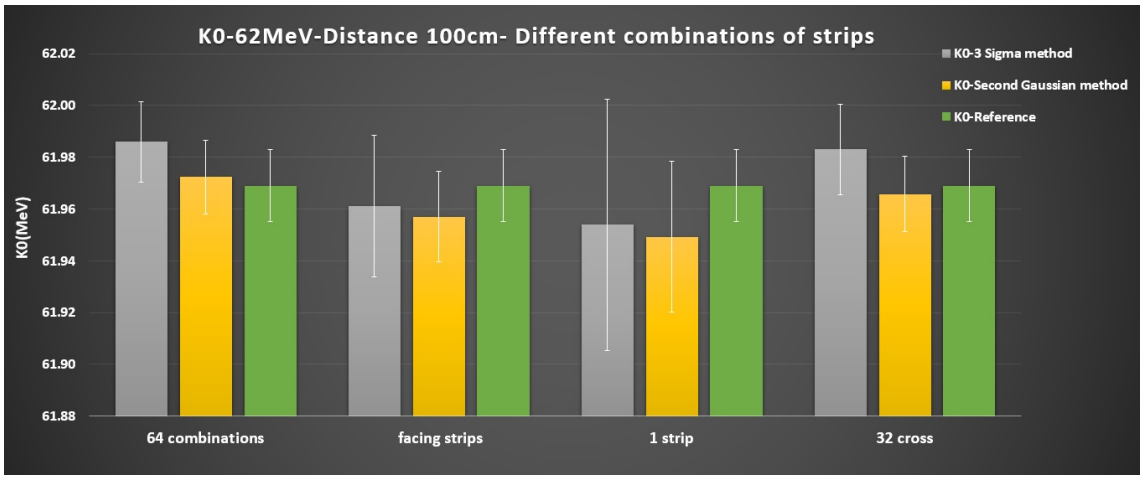

(b)

Fig. 6.2: *The measured energy using simulated wave forms for different combinations of strips at energy 62 MeV and distances (a) 40 cm and (b) 100 cm.*

6.1.2 The sensors alignment

One of the parameter which affects the system efficiency is related to detectors alignment. The two sensors must be located in the right alignment on the telescope with respect to the isocenter. The coordinate of sensors was determined by three axes: x, y and z. The z-axis represented the distance between two sensors d. Since the distance d directly affects the TOF and proton beam energy measurements and contributes to the systematic error, its effect was investigated in the system calibration approaches described in the following

sections. The length of the strips was in the direction of x-axis and their width was in the direction of y-axis. Also, a tilt of the S2 was introduced to check the effect of angular misalignment.

To evaluate the effect of the sensors misalignment on the efficiency of the system, the TOF, and consequently the measured proton beam energy, the different possible misalignment were evaluated using the MoVeIT tool simulation.

The possible misalignment were simulated as follows for 62 MeV and 227 MeV proton energy, and distance of 40 cm and 100 cm. These simulations were repeated for the possible combinations of strips as presented earlier (64 combinations, one strip combination and 32 cross combinations):

- The Reference alignment was defined as: $x = 0$, $y = 0$, $\theta = 0$.
- The S2 shifted vertically by one strip width, the coordinates were defined: $x = 0$, $y = 0.55\ mm$, $\theta = 0$.
- The S2 shifted vertically and horizontally by one strip width, the coordinates were defined: $x = 0.55\ mm$, $y = 0.55\ mm$, $\theta = 0$.
- The S2 was tilted by 3 degrees without any movement along the x and y axis, the coordinates were defined: $x = 0$, $y = 0$, $\theta = 3$.
- The S2 was tilted by 90 degrees without any vertically or horizontally movements, the coordinates were defined: $x = 0$, $y = 0$, $\theta = 90$.
- The S2 shifted vertically and horizontally by one strip width. Also the S2 was tilted by 90 degrees. The coordinates were defined: $x = 55\ mm$, $y = 0.55mm$, $\theta = 90$.

Figure 6.3 shows all the possible positions which were investigated to evaluate the effect of the sensors alignment on the system efficiency. The blue detector is S1 and the red one is S2. Looking at the 2D-Gaussian distribution of the simulated proton beam, the center of the circles show only the position of the beam relative to the sensors.

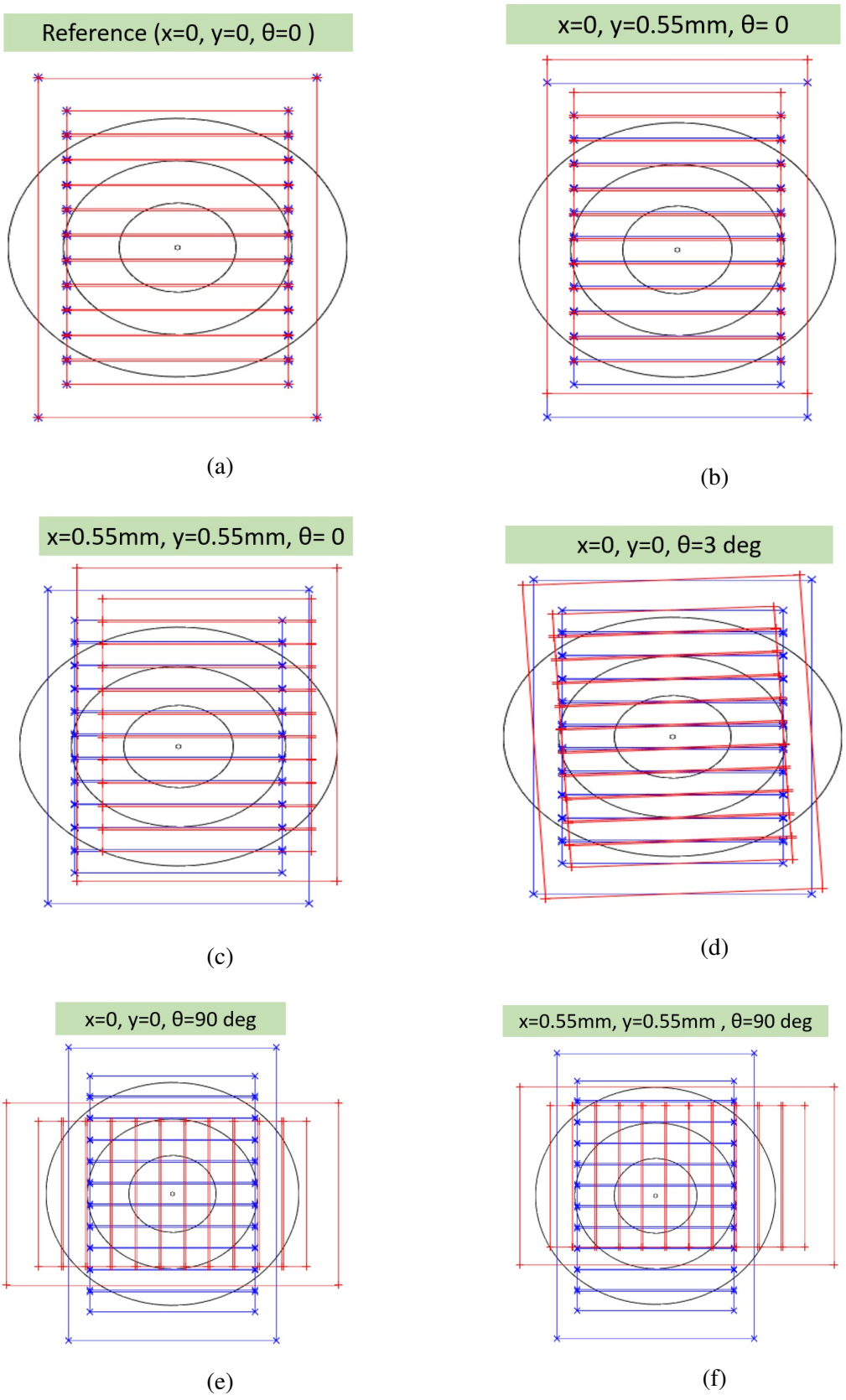

Fig. 6.3: *The different possible alignments which were evaluated using MoVeIT tool simulation. (a) is the reference coordinates and (b) to (f) indicate the possible misalignments with respect to the reference point. The blue detector is S1 and the red one is S2. The coordinates of each position are written in the green box on the top of it. The center of the circles corresponds to the simulated beam center.*

Figure 6.4 shows an example of the coincidence signals distribution in 64 combinations of strips for the possible alignments in case 62 MeV and 40 cm. Compared to the reference alignment (a), for 64 combinations there is no significant difference in the number of coincidences for all the possible alignments, apart from figures (e) (f), where the second sensor is rotated by 90 degrees.

Figure 6.5 shows the comparison of the number of coincidence signals, the TOF and the kinetic proton energy at isocenter K_0 with the reference position($x = 0, y = 0, \theta = 0$) for alignment simulation results from energy 62 MeV and distance 40 cm. To show the improvement of statistics, the number of coincidences was normalized to the number of coincidences of one combination.

In case 64 combinations the number of coincident signals is ~ 32 times and in cases 32 combinations ~ 19 times larger than in single strip mode (Fig. 6.5 a). Thus, as it is expected considering the increased statistics, the measured energy error in case of the single strip combination has the maximum error while there is no significant difference error in other combinations. In case 32 cross combinations, the efficiency is larger than half of what obtained with the 64 combinations (Fig. 6.5 b).

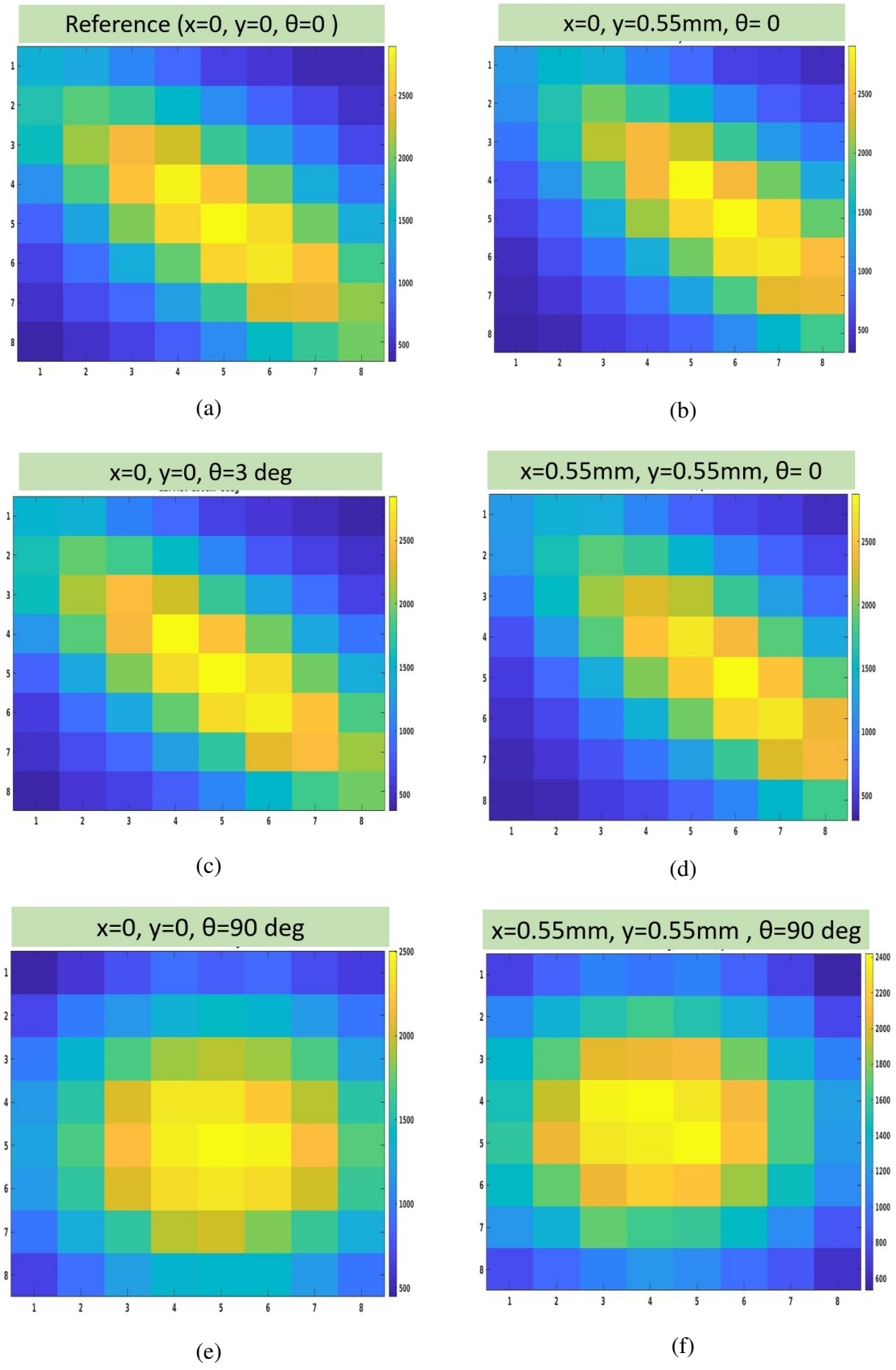

Fig. 6.4: *(a) to (f) are indicated the coincidence signals distribution of the possible alignments for energy 62 MeV and 40 cm distance.*

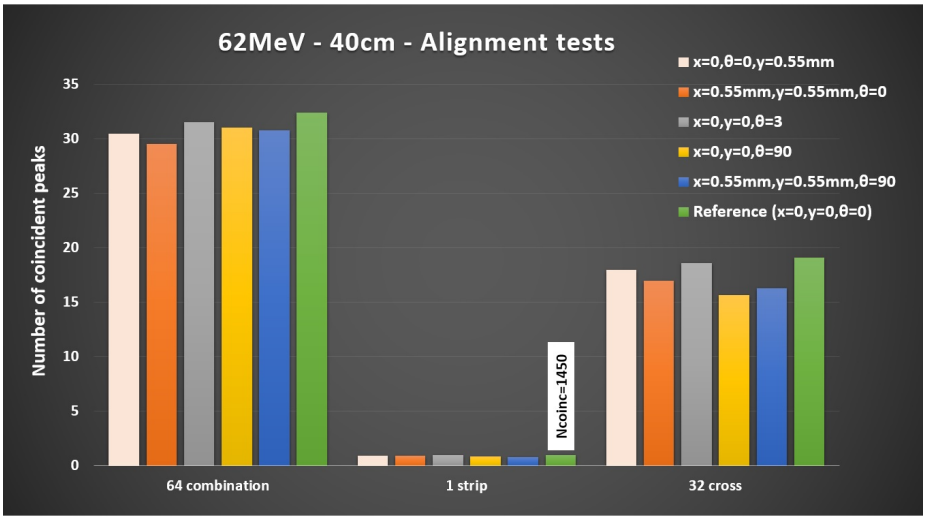

(a)

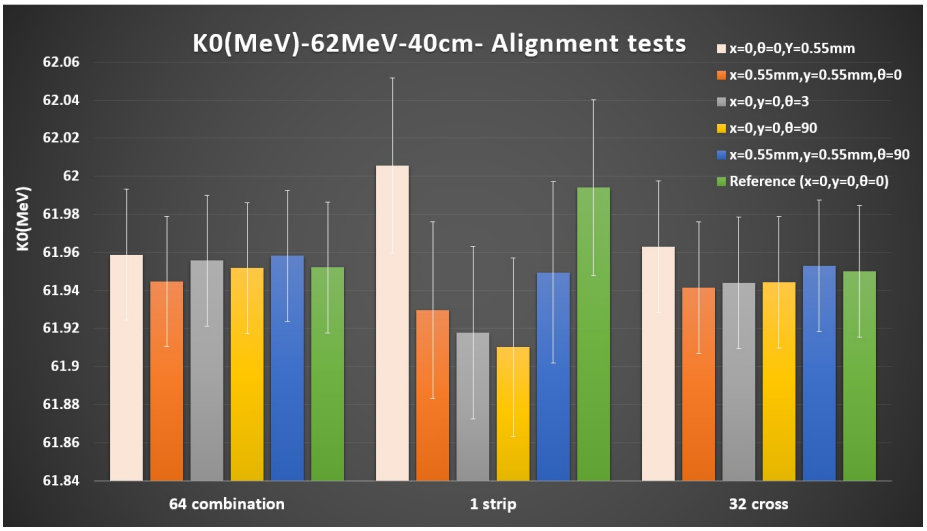

(b)

Fig. 6.5: The misalignment simulation results from energy 62 MeV and distance 40 cm. (a)The coincidence number for different combinations of strips normalized to the number of coincidence signals of one strip combination for all the possible misalignment. (b) The measured energy k_0 and related errors corresponding the data analysis of (a).

Figure 6.6 shows the same results of Fig.6.5 for distance 100 cm. At the maximum distance between sensors, there are a less effects due to the misalignment in all combinations. It can be explained by the fact that the protons scattered in S1 along the long distance will diverge in all the directions, making the efficiency less sensitive to the alignment. As Figure 6.6 b, the largest error on the measured energy in the single strip combination is due to the very small number of coincidences and lowest efficiency compared to the 64 and 32 combinations.

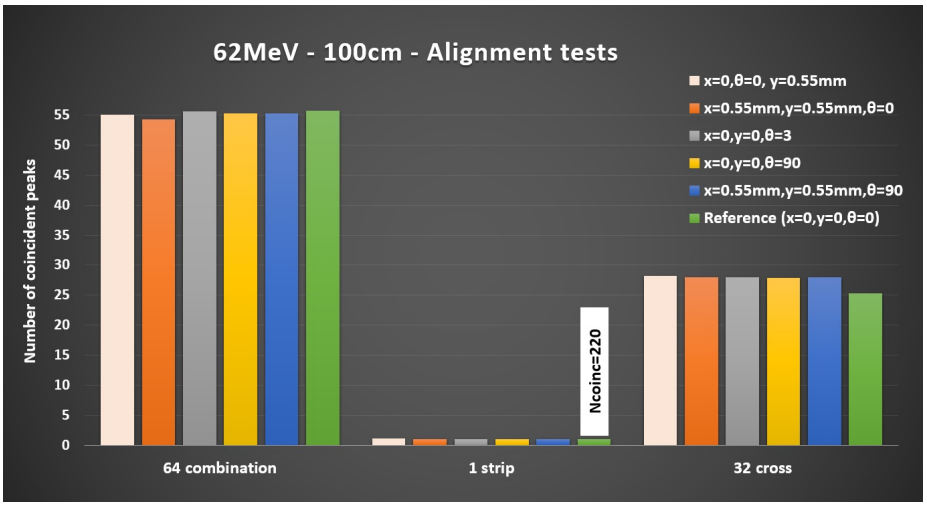

(a)

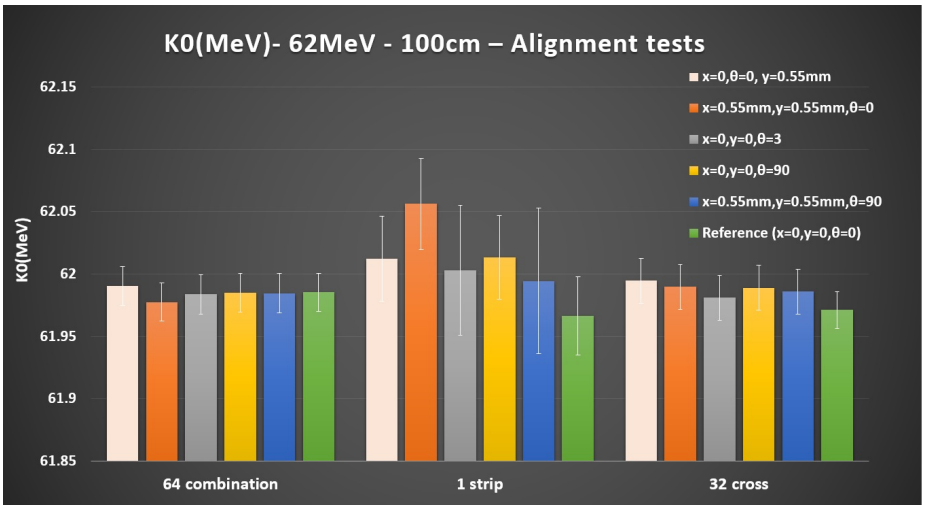

(b)

Fig. 6.6: The misalignment simulation results from energy 62 MeV and distance 100 cm. (a) The coincidence number for different combinations of strips normalized to the number of coincidence signals of single strip combination for all the possible misalignment. (b) The measured energy k_0 and related errors corresponding the data analysis of (a).

Fig.6.7 shows the effect of sensors alignment on the system efficiency for the proton beam energy 227 MeV and distance of 40 cm. As the proton beam energy is increased to the maximum value, the proton beam is less divergent than at the minimum energy of 62 MeV. Thus the number of protons which is passing through the sensors is larger and in particular for the shorter distance (40 cm) leads to a larger number of coincidences. If only 32 combinations are condsidered, tilting the second sensor by 90 degrees reduces the efficiency.

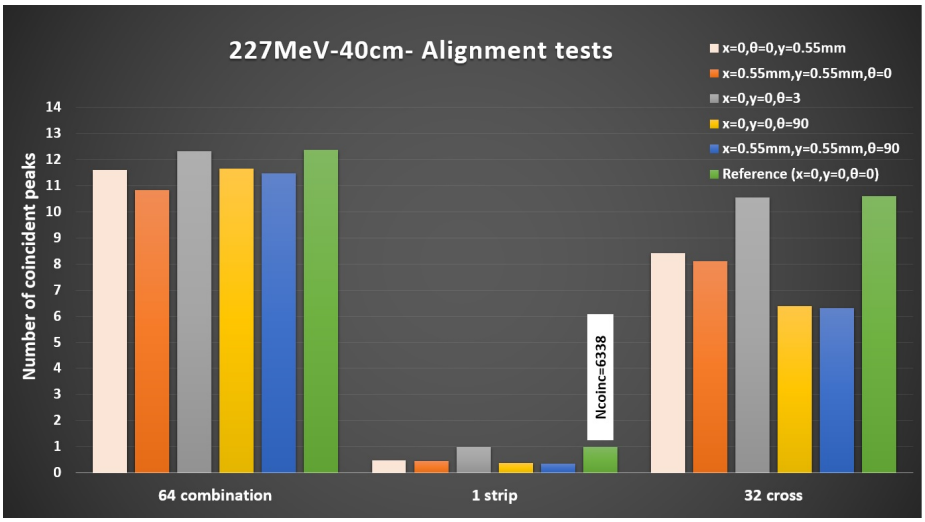

(a)

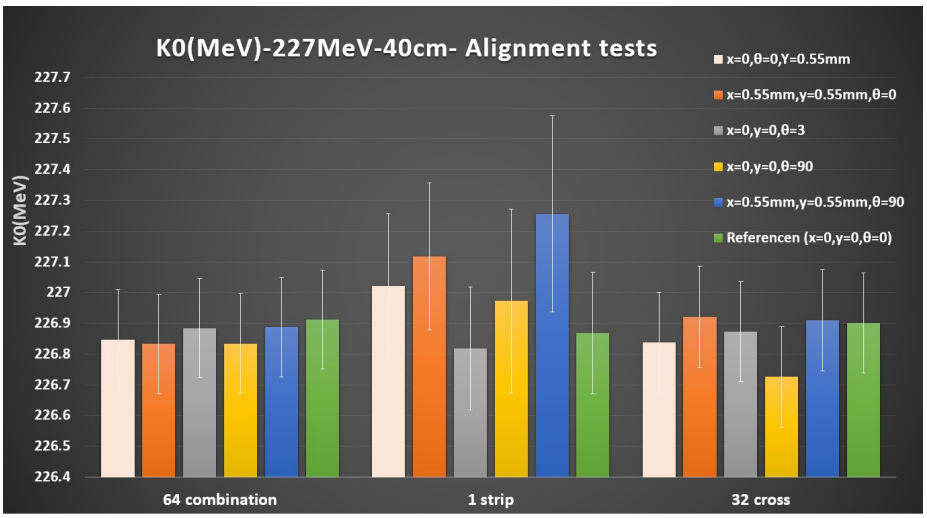

(b)

Fig. 6.7: The misalignment simulation results from energy 227 MeV and distance 40 cm. (a) The coincident number of different combinations of strips normalized to the number of coincident signals of one combination for all the possible misalignment. (b) The measured energy k_0 and related errors consider to the data analyzing of (a).

The same results of the energy 62 MeV for both distances 40 cm and 100 cm can be also observed in cases of energy 227 MeV (Figs. 6.7 and 6.8). Generally, based on the figures 6.5 to 6.8, the largest error on the measured energy can be observed in case one strip combination due to the lowest system efficiency. The fact that at the largest distance there are less effects caused by misalignment is due to multiple scattering which makes the perfect alignment of S2 less important than at 40 cm.

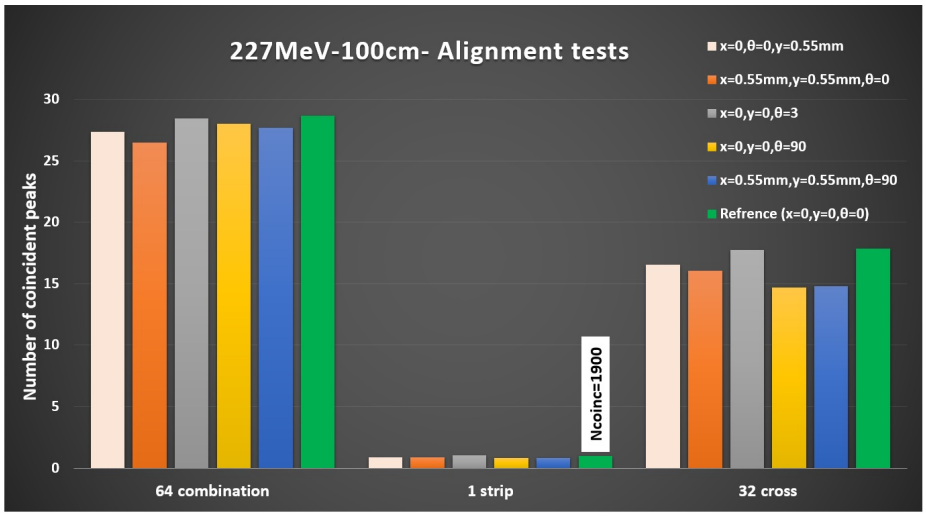

(a)

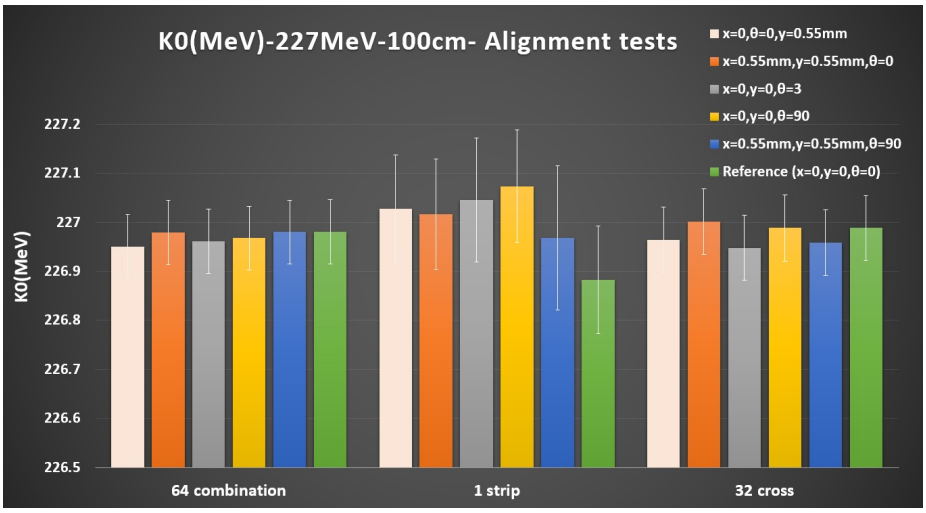

(b)

Fig. 6.8: The misalignment simulation results from energy 227 MeV and distance 100 cm. (a)The coincidence number for different combinations of strips normalized to the number of coincidence signals of one strip combination for all the possible misalignment. (b) The measured energy k_0 and related errors corresponding the data analysis of (a).

6.1.3 Effect of the proton beam flux

Increasing the flux beam, the number of particles which are passing through the sensors at the same time increases, and the pile-up effect and the false coincidences increase correspondingly.

As discussed in chapter 4, the TIFPA beam flux for energy 70 MeV - 228 MeV is $3.8 \times 10^6(p/s)$ - $2.3 \times 10^8(p/s)$ at 1 nA beam extraction current. The extraction current can be increased up to 320 nA, and the flux can scale consequently. At CNAO the flux ranges are between $10^9(p/s)$ and $10^{10}(p/s)$.

To examine the system efficiency in different flux beam, we performed the wave forms simulation using the MoVeIT tool simulations in terms of the proton beam energy and the distance between sensors d for the different proton beam flux from 100 MHz to 5000 MHz on the first sensor.

Figures 6.9 and 6.10 indicate the measured proton beam energy K_0 versus the beam flux as function of energy and distance. The largest error in the measured proton beam energy K_0 is observed at the energy 62 MeV at distance 40 cm. The reason is that moving from 40 to 100 cm two effects are observed, the decrease of statistics (increases the error) and the reduction of sensitivity to distance (reduces the error).

The larger value of measured energy K_0 for distance 100 cm and the lower error in these cases, referring the contribution of the relative error of TOF in the energy measurement for large distance than the short distance.

In this section we described the simulation studies about some possible variations of data taking conditions and their effect on the system efficiency to optimize our system in order to measured the TOF and the proton beam energy. In the next section, the system calibration due to the sources of errors will be represented.

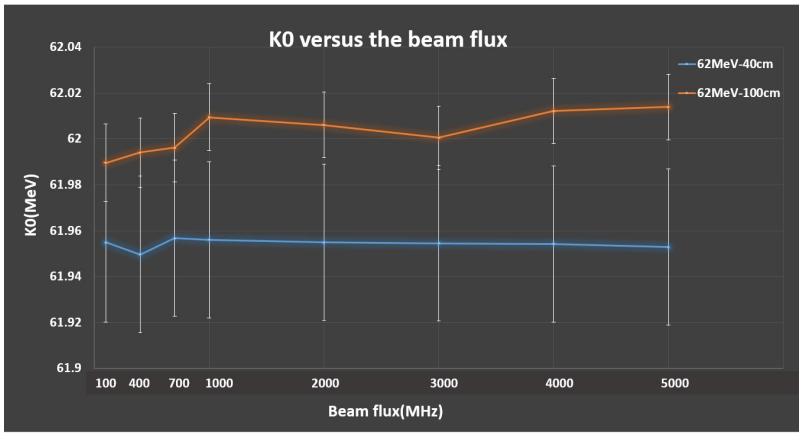

Fig. 6.9: *The measured proton beam energy K_0 versus the beam flux for energy 62 MeV and distances 40 cm and 100 cm.*

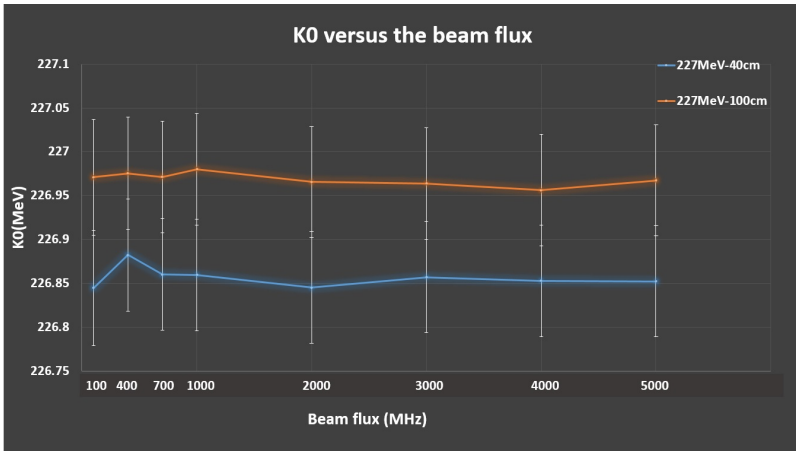

Fig. 6.10: *The measured proton beam energy K_0 versus the beam flux for energy 227 MeV and distances 40 cm and 100 cm.*

6.2 The system calibration

Considering the setup for the energy determination from TOF (sec. 4.2 , 4.6) and the different data taking conditions (sec. 6.1), the main sources of systematic errors for the setup used during the experimental tests at CNAO and TIFPA reside in the uncertainty of the distance between the sensors d and of the time $offset$ due to the signal routing of the electronic chain. Thus, these quantities need to be determined precisely by developing a calibration method. To this aim, the two possible system calibration approaches were developed. The details of each method were described in the following.

6.2.1 The relative calibration approach

For implementing the relative approach in the system calibration, it was assumed that set of energies were known with high precision (nominal energies) and could be used for the calibration. Using the measured TOFs, the system was calibrated through a global fit χ^2 minimization over the data (minuit function of ROOT[104]). Therefore, this approach calibrates the system using as input the nominal energies, and as output, the distances and time offset.

$$\chi^2(offset, d_j) = \sum_{ij} \left\{ \frac{(TOF_{ij} - offset) - TOF(K_i, d_j)^2}{\sigma_{TOF_{ij}}} \right\} \tag{6.1}$$

where K_i are the nominal energies reduced by the energy loss in the first detector and in half of the air gap, while $offset$ and distances d_j are the free parameters of the χ^2 minimization.

$$TOF(K_i, d_j) = \frac{(K_i + E_0)d_j}{c\sqrt{(K_i + E_0)^2 - E_0^2}} \tag{6.2}$$

In equation 6.2, E_0 is the proton mass energy at rest and c is the light speed. The process involves different values of d_j and $offset$, and the final results are the ones that minimize χ^2. The distances and the time offset can be then used in equations 4.3 and 4.4 to obtain the value of the unknown energies from the measured TOF values. This method were adopted for the analysis of the data acquired at CNAO and TIFPA, where the error on the energy values provided by the CNAO facility was very small, 0.1 MeV, while for TIFPA was 0.5 to 1 MeV.

6.2.2 The self-calibration approach

The self-calibration uses a set of Δt_{mean} obtained from measurements made at different sensor's distances and proton energies, and finds the best values of x_0 and $offset$ that minimize a specific square deviation equation. The method is based on the possibility of being able to move the S2 to other known distances with great precision, for example using a linear stage (see figure 6.11). In this case, the average proton velocity between two of these positions can be determined without the presence of systematic positioning errors or time offset. Figure 6.11 shows S1 positioned at $x = 0$, while S2 can be moved at positions x_0, $x_1 = x_0 + \Delta d_1$, $x_2 = x_0 + \Delta d_2$,..., $x_n = x_0 + \Delta d_n$ and the displacements Δd_1 , Δd_2, ..., Δd_n are well known using an encoder. However, the initial position x_0 for the S2 can be different for each experiment because it depends on how the board is assembled, on the

sensor thickness, tilt, and any positioning error.

Using the methodology described in section 4.6, for each distance between sensors $d_i = x_i$, the mean time difference Δt is related to the measured TOF by 4.3 ($\Delta t_i = TOF_i + offset$). In this case, there are two unknowns parameters, x_0 and $offset$, which are required to calculate the proton average velocity defined by equation 4.4. However, the average velocity can be calculated without knowing x_0 and $offset$ if two absolute positions of the S2, (x_i, x_j) and their respective mean arrival time $(\Delta t_i, \Delta t_j)$ are used, as shown in equation 6.3.

$$v_{avg_{i,j}} = \frac{x_j - x_i}{\Delta t_j - \Delta t_i} = \frac{(x_0 + \Delta d_j) - (x_0 + \Delta d_i)}{\Delta t_j - \Delta t_i} = \frac{\Delta d_j - \Delta d_i}{\Delta t_j - \Delta t_i} \tag{6.3}$$

All the Δd and Δt in equation 6.3 are well determined by measurement and, the difference of $(\Delta t_j - \Delta t_i)$ is equivalent to the difference of TOFs, removing $offset$ from the equation 6.4.

$$\Delta t_j - \Delta t_i = (TOF_j + offset) - (TOF_i + offset) = TOF_j - TOF_i \tag{6.4}$$

With the average velocity $v_{avg_{i,j}}$ between the position x_i and x_j is possible to calculate the average kinetic energy using equation 4.5. The proton kinetic energy after passing S1 can be then determined as a function of x_0 using equation 4.6. For the energy loss correction, the position where the average velocity was calculated $(x_i + x_j)/2$ is used, resulting in equation 6.5.

$$K_{1_{i,j}}(x_0) \approx K_{avg_{i,j}} + \left(\frac{S}{\rho}(K_{avg_{i,j}})\right)_{air} . \rho_{air} . \left(x_0 + \frac{\Delta d_j - \Delta d_i}{2}\right) \tag{6.5}$$

The value of x_0 can be determined through a system equation of $K_{1_{i,j}}$ calculated with different combinations of positions i, j (where $j > i$, and $i > 1$), but in that case, the time $offset$ would remain unknown. To determine x_0 and the $offset$, a specific approach is proposed. Using the $K_{1_{i,j}}(x_0)$, the values of the proton velocity after passing the first sensor $v_{1_{i,j}}(x_0)$ were calculated using the inverse of equation 4.5.
If Δt is measured at $n+1$ positions $(x_0, x_1 \ldots x_n)$ of the S2, a total of $m = \frac{(n+1)!}{[2!.(n-1)!]}$ values of $v_{1_{i,j}}$ could be calculated using the combinations of i, j (where $i = 0 \ldots n-1, j = 1 \ldots n$ and $j > i$).

Two positions i and j are used for the calculation of the proton velocity. With the calculated proton position the proton path is reconstructed that it is called k. Using the m values of $v_{1_{i,j}}$ calculated from the combinations of the second sensor position, the measured Δt_k and the well-known displacement Δd_k, we developed a self-calibration method looking

for the values of x_0 and the offset which minimizes a deviation squared of $(d_k - x_k)$ defined by equation 6.6.

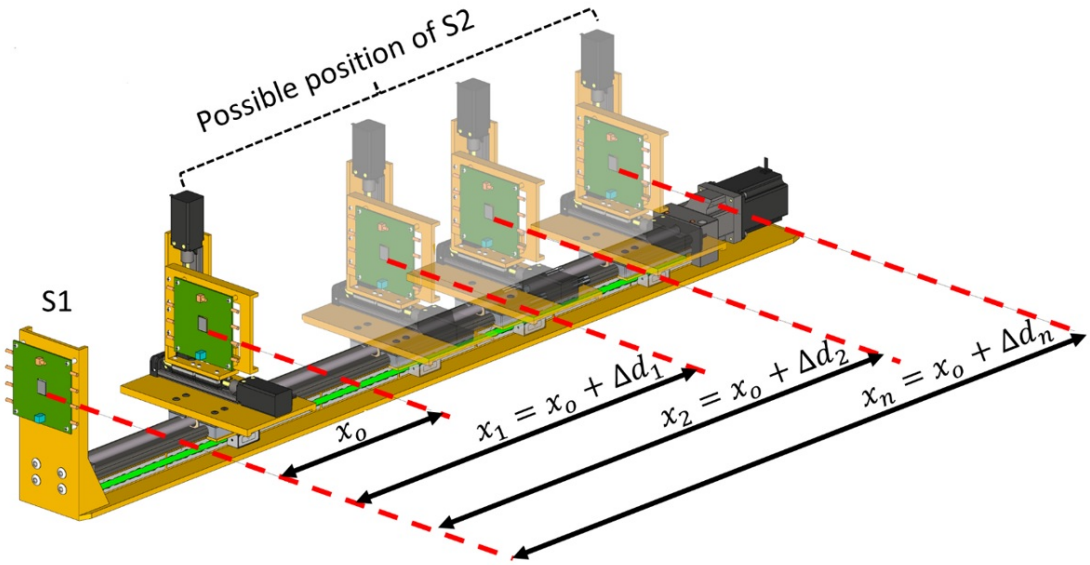

Fig. 6.11: *Schematic view of the mechanical device where the second sensor S2 is free to move from x_0 to x_n.*

$$dev^2(x_0, offset) = \sum_{k=0}^{n} \sum_{j>i}^{n} \sum_{i=0}^{n-1} \left(\frac{[v_{1_{i,j}}(\Delta t_k - offset)] - (x_0 + \Delta d_k)}{\sigma_{i,j,k}} \right)^2 \tag{6.6}$$

Where $\sigma_{i,j,k}$ is the error of d_k calculated using the $v_{1_{i,j}}$ and Δt_k. This deviation squared equation can be expanded if the measurement of the Δt_k and Δd_k are done with different proton energies $(K_{min} \ldots K_{max})$. The final equation for the minimization can be expressed as:

$$DEV^2(x_0, offset) = \sum_{E=K_{min}}^{K_{max}} dev_E^2(x_0, offset) \tag{6.7}$$

A program to perform the self-calibration and find the best values of x_0 and offset that minimize equation 6.7 was developed in Matlab.

6.3 Test and validation of the self-calibration approach with simulated data

The main problem with both of the calibration methods was the fact that it was necessary to know the beam nominal energies with high precision; in the relative method to do the global fit; and in the self-calibration method to compare the final measured energies with the nominal ones. A solution to bypass this restriction was the use of Monte Carlo simulation to obtain a well-known set of data for test and validation. To study the main sources of TOF uncertainty, simulations of waveforms were required.

In order to test and validate the self-calibration method, some simulations were done using MoVeIT tool for the proton energies between 62 MeV to 227 MeV, distances from 200 mm to 1000 mm, 0.100 mm thickness of S1 and a fixed time offset of 100 ps. Table 6.1 summarizes the measured Δt_{mean} (ns) for each simulation. These Δt_{mean} values were used to determine the proton beam energy based on the method which was described in section 4.6 and used as input for the self-calibration method. The calibration process should give back similar values of simulated x_0 distance and a time offset. The validation of the self-calibration approach can be performed checking the accuracy of the proton energy calculation at the isocenter using the calibration results. The results will be presented in the next chapter.

Table 6.1: Table of Δt_{mean} (ns) obtained from the analysis of signals simulations conducted at five energies, six positions and a fixed time offset of 100 ps. The uncertainty for all the times is 1 ps.

	Distance between sensors (x_i) [mm]					
Nominal K0 [MeV]	**199.9**	**299.9**	**399.9**	**599.9**	**799.9**	**999.9**
62	2,027 ns	2,993 ns	3,960 ns	5,896 ns	7,836 ns	9,778 ns
105	1,626 ns	2,391 ns	3,155 ns	4,684 ns	6,214 ns	7,745 ns
150	1,415 ns	2,074 ns	2,733 ns	4,051 ns	5,371 ns	6,689 ns
180	1,326 ns	1,939 ns	2,553 ns	3,780 ns	5,007 ns	6,235 ns
227	1,223 ns	1,786 ns	2,349 ns	3,474 ns	4,600 ns	5,726 ns

6.4 Test and validation of the self-calibration approach with the measurement data

In addition to simulated data, the self-calibration method was applied to the data acquired from the real proton irradiations carried out at CNAO and TIFPA facilities. These measurements were done with different beam energies (62 MeV to 227 MeV) using the experimental set-up shown in Fig. 4.4 and 4.6, where the S2 was moved to a set fixed positions on the positioning table (70 mm to 970 mm). All the collected waveforms were used to derive the proton kinetic energy at isocenter K_0 from the measured Δt_{mean} using the methodology described in section 4.2.

Table 6.2 summarizes the Δt_{mean} obtained for each combination of sensor distance and beam energy for CNAO and TIFPA. These data were acquired during the experimental test at CNAO and TIFPA with the setup described in chapter 4. To compare the results of self-calibration method with the relative method already published [107], we used the same data acquired at CNAO. We extended the dataset with data acquired at TIFPA which has a completely different beam time structure to benchmark the calibration method in a different environment. It should be noted that the nominal energy K_0 values were provided by the facilities. At CNAO the nominal energies were measured by measuring the range using a PeakFinder with an uncertainty of 0.1 MeV [87] while at TIFPA a Giraffe detector was used and the uncertainties are between 500 keV up to 1 MeV [91]. The data was previously calibrated using the relative calibration method which was used as a reference to compare with the self-calibration results. All these results are shown in the next chapter.

Table 6.2: CNAO and TIFPA Δt_{mean} as a function of the sensor distances used for the self-calibration method

CNAO		
Distance [mm]	**Nominal K_0 [MeV]**	**Δt_{mean}(error) [ns]**
70	58.9	0.764 (0.001)
	77.6	0.691 (0.001)
	103.5	0.624 (0.001)
	148.5	0.554 (0.002)
	226.1	0.492 (0.002)
370	58.9	3.725 (0.002)
	77.6	3.301 (0.002)
	103.5	2.921 (0.002)
	148.5	2.523 (0.001)
	226.1	2.161 (0.002)
670	58.9	6.699 (0.003)
	77.6	5.922 (0.002)
	103.5	5.231 (0.002)
	148.5	4.520 (0.002)
	226.1	3.863 (0.002)
970	58.9	9.666 (0.003)
	77.6	8.549 (0.003)
	103.5	7.548 (0.003)
	148.5	6.508 (0.002)
	226.1	5.557 (0.002)

TIFPA		
Distance [mm]	**Nominal K_0 [MeV]**	**Δt_{mean}(error) [ns]**
270	68.3	2.394 (0.001)
	98.5	2.024 (0.001)
	147	1.694 (0.001)
	182.7	1.556 (0.001)
	227.3	1.422 (0.001)
670	68.3	6.094 (0.002)
	97	5.208 (0.001)
	163	4.173 (0.001)
	182.7	3.992 (0.001)
	222.8	3.695 (0.001)
	227.3	3.664 (0.001)
970	68.3	8.882 (0.003)
	97	7.589 (0.001)
	147	6.352 (0.001)
	163	6.083 (0.001)
	182.7	5.824 (0.001)
	222.8	5.402 (0.001)
	227.3	5.363 (0.001)

Chapter summary

This chapter gave a concise overview of the evaluation of the systematic effects and the system calibration approaches. The different data taking conditions and parameters to optimize the TOF and energy measurement as function of the proton beam energy and distance between sensors were presented. The two system calibration methods were introduced and, finally, these calibration approaches were investigated in the simulated and measured data to validate the final design of system to measure the proton beam energy.

Chapter 7

Results

"Who are we? The answer to this question is not only one of the tasks but the task of science."

Erwin Rudolf Josef Alexander Schrödinger

7.1 The beam test at CNAO using pad sensors

The mean time difference Δt_{mean} measured with the procedure described in section 4.5 are shown in figure 7.1 for the five different beam energies and the four distances between the two sensors of the telescope used in the first CNAO test.

The Δt_{mean} values as a function of distance for each beam energy were interpolated linearly. The slopes of the interpolation lines increase with decreasing energy as they are proportional to the inverse of the velocity. The intercepts of the interpolation lines provide the time offset and proved to be independent of the energy, as expected considering that it is induced by differences in the routing of signals.

For irradiation times ranging between $\sim 3s$ (corresponding to $\sim$5200 coincident signals for d = 7 cm between the sensors and 58.9 MeV beam energy) and $\sim 9s$ (corresponding to $\sim$ 4700 coincident signals for d = 97 cm between the sensors and 226.1 MeV beam energy), the statistical error on the measured Δt_{mean} is of the order of a few ps and cannot be seen in the figure.

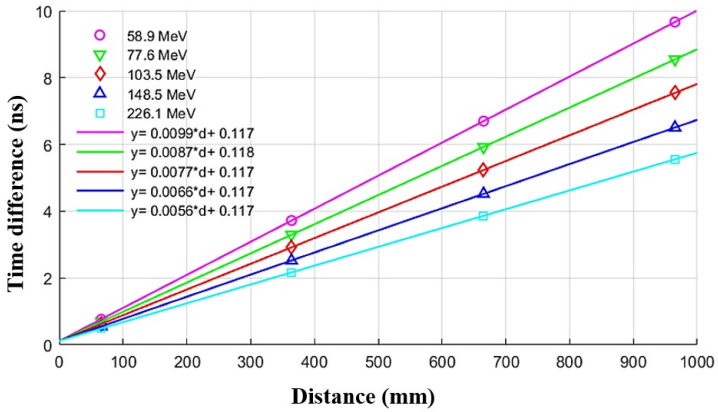

Fig. 7.1: *The measured mean time difference Δt_{mean} in the experimental measurement test at CNAO using pad sensors as function of distance for five proton beam energies (nominal values 58.9, 77.6, 103.5, 148.5, 226.1 MeV) and four distances between the two sensors (7, 37, 67 and 97 cm).*

7.2 The beam test at TIFPA using strip sensors

The mean time differences Δt_{mean} measured with the procedure described in section 4.5 are shown in figure 7.2 for the different beam energies from 68 MeV to 227.3 MeV and the three distances between the two strip sensors of the telescope used in the beam test at TIFPA. As obvious, the increase in energy decreases the Δt_{mean} and while the distance increases, the Δt_{mean} increases. These acquired results from CNAO and TIFPA were used to test and validate the calibration methods as described in sec. 6.2.

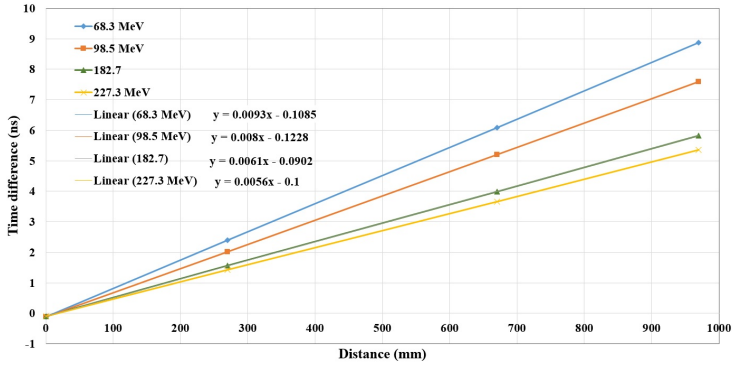

Fig. 7.2: *The measured mean time difference Δt_{mean} in the beam test at TIFPA using strip sensors as function of distance for proton beam energies from 68 MeV to 227.3 MeV and three distances between the two sensors (270, 670 and 970 mm).*

7.3 Relative calibration method

The relative calibration procedure (sec. 6.2) was applied to the acquired data from the first experimental test at CNAO to find the relative sensors distances values and $offset$ (see Table 7.1) . These parameters and related uncertainties, then were used to measure the Δt_{mean}, TOF and K_0 according to the equations in sec. 4.6. The corresponding results are reported in Table 7.2.

Table 7.1: *The obtained relative distances and offset from adopting the relative calibration method on the data acquired in the first test at CNAO.*

CNAO		
Parameter	**Value**	**Error**
$d1$ (mm)	65.78	0.33
$d2$ (mm)	364.02	0.42
$d3$ (mm)	665.10	0.46
$d4$ (mm)	965.15	0.49
$offset$ (ns)	0.117	0.003

The results are reported in table 7.2, where the uncertainties on the fit parameters and on Δt_{mean} were propagated to the results. The effective acquisition time and the total irradiation time are also reported in table 7.2. The effective acquisition time corresponds to the irradiation time acquired, stored and transmitted by the digitizer, i.e. approximately 0.4 % of the total irradiation time.

As Table 7.2, a precise and accurate energy measurement can be observed at the two largest distances. On the contrary there are the larger uncertainties and the deviations at the smaller distances. Moreover, referring to Figure 1.16, the obtained statistical error σ_{TOF} is compatible with the clinically acceptable accuracy in the beam energy for the distances 3 and 4, only partially compatible for distance 2 and not compatible for distance 1.

Table 7.2: List of the measured *ToFs* and energies with corresponding deviations and statistical errors, along with effective time of acquisition and total acquisition time. The considered distances and time offset (and relative errors) were provided by the Chi-Square minimization (Table 7.1), while 0.1 MeV was considered as error on the nominal energy values. The values related to the 103.5 MeV nominal energy are highlighted, as they represents the energy value not considered in the calibration method that can be used as an unbiased test point.Energy deviation is difference between the measured energy and the nominal one [107].

Distance (mm)	**Nominal Energy (MeV)**	**TOF (ns)**	σ_{TOF} **(ns)**	**Measured Energy (MeV)**	$\sigma_{E_{Measured}}$ **(MeV)**	**Energy Deviation**[a] **(MeV)**	σ_{Dev} **(MeV)**	**EAT** [b] **(ms)**	**TIT** [c] **(s)**
1 (65.78)	58.9	0.647	0.003	59.4	0.3	-0.5	0.3	1.11	3.42
	77.6	0.574	0.003	77.3	0.4	0.3	0.4	1.50	4.62
	103.5	***0.507***	***0.003***	***102.8***	***0.6***	***0.7***	***0.7***	***2.41***	***7.42***
	148.5	0.437	0.003	146.6	1.5	1.9	1.5	1.30	3.99
	226.1	0.375	0.003	218.1	3.2	8.0	3.2	1.19	3.67
2 (364.02)	58.9	3.607	0.003	58.7	0.1	0.2	0.3	2.27	6.99
	77.6	3.184	0.003	77.1	0.1	0.5	0.4	2.12	6.51
	103.5	***2.804***	***0.003***	***103.0***	***0.2***	***0.5***	***0.4***	***2.77***	***8.53***
	148.5	2.406	0.003	148.8	0.2	-0.3	0.5	3.31	10.18
	226.1	2.044	0.003	228.4	0.6	-2.3	0.8	2.89	8.89
3 (665.10)	58.9	6.582	0.004	59.0	0.1	-0.1	0.1	2.34	7.20
	77.6	5.805	0.003	77.6	0.9	0.0	0.1	2.14	6.60
	103.5	***5.114***	***0.003***	***103.6***	***0.1***	***-0.1***	***0.2***	***2.78***	***8.55***
	148.5	4.403	0.003	148.3	0.2	0.2	0.2	2.56	7.88
	226.1	3.746	0.003	226.4	0.4	-0.3	0.4	2.93	9.01
4 (965.15)	58.9	9.549	0.003	59.2	0.0	-0.3	0.1	2.43	7.48
	77.6	8.432	0.004	77.6	0.1	0.0	0.1	2.21	6.81
	103.5	***7.431***	***0.004***	***103.3***	***0.1***	***0.2***	***0.1***	***2.62***	***8.07***
	148.5	6.390	0.003	148.3	0.2	0.2	0.2	2.99	9.21
	226.1	5.440	0.003	226.0	0.3	0.1	0.304	3.01	9.25

[a] Difference between the nominal energy and the measured one
[b] Effective acquisition time (ms)
[c] Total irradiation time (s)

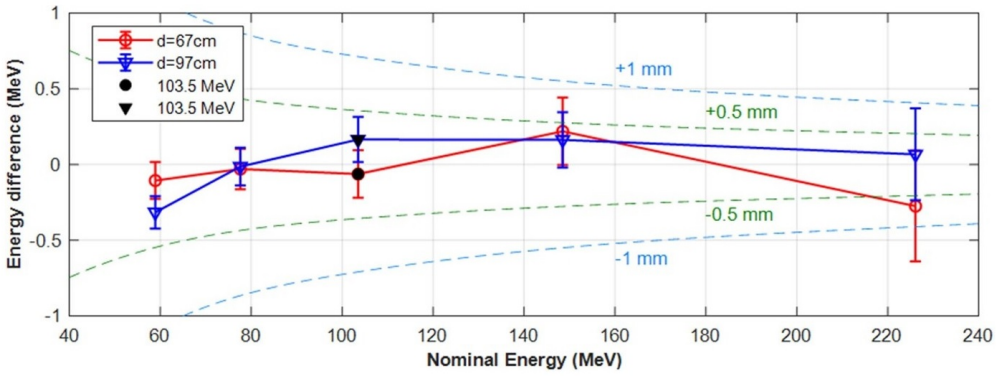

Fig. 7.3: *Deviations between the nominal and the measured energy for the 5 different energies (58.9, 77.6, 103.5, 148.5, 226.1 MeV) at 2 distances (67 cm in red and 97 cm in blue). The test point at 103.5 MeV is marked in black. The dashed lines delineate the correspondent deviations in water range (within 1 mm in light blue and 0.5 mm in green).*

The deviations between measured and nominal energies for the beam tests at 67 and 97 cm distances and for the five considered energies are reported in Figure 7.3. It is observed that the energy differences are always smaller than 0.5 MeV. One of the proton beam energy (103.5 MeV) was not considered in the calibration method and was used to independently test the calibration results. The error of the test point (i.e. 103.5 MeV) is $\sim$ 150 keV for both considered distances. From the clinical point of view, the corresponding range deviation in water is important parameter for the evaluation of the detector and method accuracy. Therefore, all the proton energies were converted into the water range using the Bragg-Kleman rule [113, 114] and ICRU-49 data [50] as reported by [49]. The corresponding differences between nominal and measured beam energy as the water range for 67 cm and 97 cm are shown in Figure 7.3. The range differences are within half millimetre for the lower energies and within one millimetre for the maximum energy, in accordance with the clinical requirements.

7.4 Self-calibration method

7.4.1 Test and validation with simulated data

As mentioned, the self-calibration was performed using simulated data thorough MoVeIT tool. Table 7.3 summarizes the seven cases which are the most significant combinations of the Δt_{mean} reported in table 6.1, and the self-calibration results for x_0 and $offset$. The goal was to find an arrangement to apply and validate the methodology with the least input data

as possible. Figure 7.4 shows an example of the self-calibration output for case 1, which uses all the simulated data. The x_0 and $offset$ outputs were reported as the coordinates of the minimum residue, and their iteration search steps were reported as the error, see table 7.3.

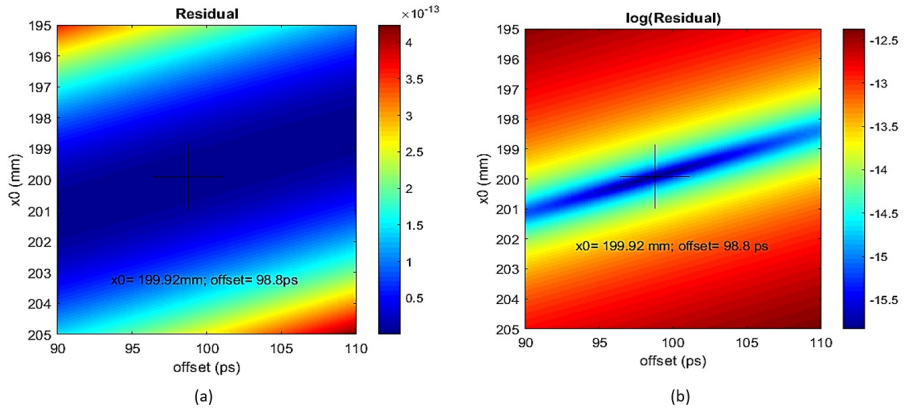

Fig. 7.4: *Self-calibration of the simulated data, case 1. a) Square weighted residual distribution. b) Distribution of the residual logarithm for better visualization of the minimum location. The expected x_0 is 199.90 mm and $offset$ equal to 100 ps.*

Table 7.3: Self-calibration of simulated data for different Δt_{mean} combinations. The errors for the x_0^{rel} and offset determination were 0.01 mm and 0.1 ps respectively.

	Δt_{mean} **used for calibration**		**Calibration results**	
Case	**Distances** x_0,x_1,... ,x_n **[mm]**	**Nominal** K_0 **[MeV]**	x_0^{rel} **[mm]**	$offset$ **[ps]**
1	**200**, 300, 400, 600, 800, 1000	62, 105, 150, 180, 227	199.92	98.8
2	**200**, 300, 400, 600, 800, 1000	62, 227	199.98	97.9
3	**200**, 300, 400, 600, 800, 1000	62,150,227	199.99	97.8
4	**300**, 400, 600, 800, 1000	62,227	300.01	98.0
5	**300**, 400, 600, 800, 1000	62,150, 227	300.06	97.4
6	**400**, 600, 800, 1000	62, 227	400.15	96.9
7	**400**, 600, 800, 1000	62,150,227	400.16	96.7

The expected value of x_0 for each case is the first position used (highlighted in bold) minus 0.100 mm thickness of sensor S1. For example, for case 1, x_0 would be 199.9 mm (200.0 mm minus 0.1 mm). To compensate the underestimation between 1% to 3% of the time offset used in the simulation, for all the cases, the initial position x_0^{rel} obtained in the calibration is slightly larger than the expected value. It is particularly interesting that there are no significant changes in the results if only the minimum and maximum protons energies are used during the calibration, while the positions number and limits do affect the time offset determination. Case 4 seems to be a good choice for calibration with a reduced number of input data (table 7.3).

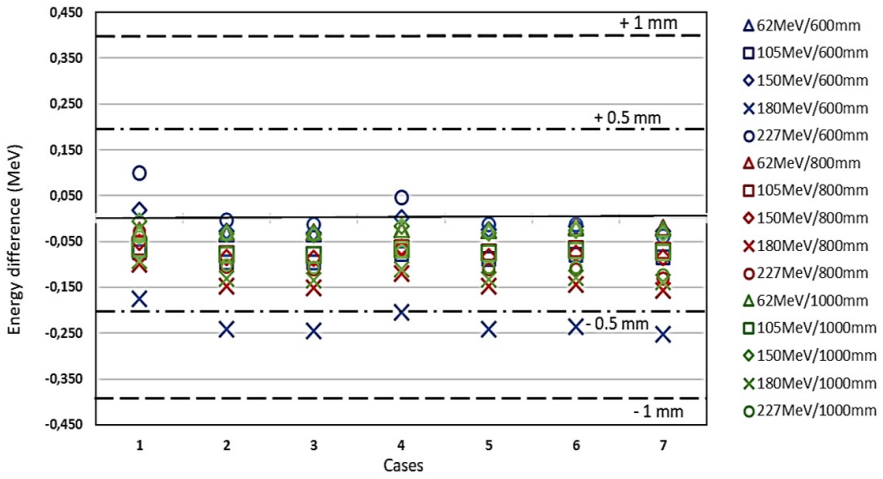

Fig. 7.5: *Difference between the nominal and calculated kinetic energy at isocenter K_0 for each distance and case adopting the self-calibration method.*

To estimate the accuracy of the self-calibration results, the proton energies at the isocenter (K_0) were calculated for each case using equations 4.3 to 4.7. The distance d for each position was considered as $d_n = x_0^{rel.} + \Delta d_n$, where $\Delta d_n = x_n - x_0$.
Figure 7.5 shows the difference between the simulated K_0 energies and the calculated for each case. Horizontal lines indicate reference levels of conversion from $\Delta K_0 = K_0^{nom.} - K_0^{cal.}$ into range difference ($\Delta R = R_{nom.} - R_{cal.}$) for 240 MeV protons (limit case). However, this conversion depends on the initial proton energy (K_0), as can be seen in Figure 7.6, where the ΔK_0 are shown together with ΔR curves as a function of the nominal energy for the three largest distances. Because the time offset resulted from calibration is slightly smaller than the simulated, the $TOFs$ will be larger as well as the calculated proton energies, resulting in the negative values seen in figure 7.5. It is noteworthy that for all the calibration combinations studied, the energy difference was under the limit required for 1mm of range uncertainty in water.

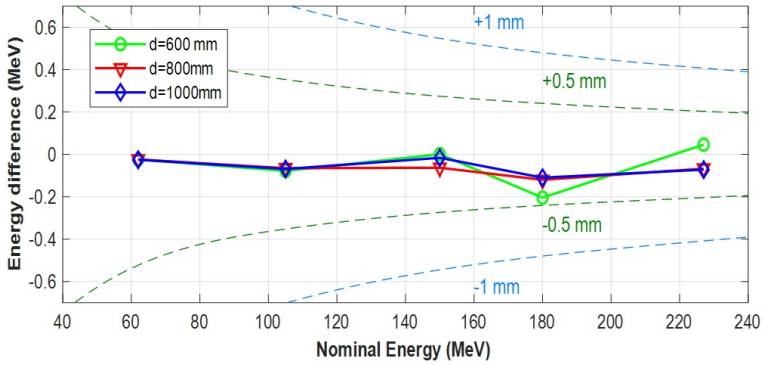

Fig. 7.6: *Energy difference* ($K_0^{nom.} - K_0^{cal.}$) *for the three largest sensors distances, using the calibration result from Case 4.*

7.4.2 Application to experimental measurements

The self-calibration was applied to experimental data acquired at the CNAO and TIFPA proton therapy centers. Table 7.4 shows the distance and offset results obtained using both the relative and self-calibration methods. The output of the relative method consists of an offset value and distances equal to the number of positions used for the calibration, in this case, four and three distances for CNAO and TIFPA respectively. On the other hand, for the self-calibration method, the output is only the $offset$ and the first distance value: x_0. The remaining distances are calculated as $x_n = x_0 + \Delta d_n$, where Δd_1, Δd_2 and Δd_3 are equal to 300 mm for CNAO and TIFPA and Δd_1 and Δd_2 are 400 mm and 300 mm respectively for TIFPA. Table 7.4 shows that the parameters obtained with both methods are in agreement if errors are considered. It should be noted that the offset value obtained for the TIFPA measurements was negative. This was due to a different arrangement of the sensor's cables connected to the digitizer input.

Table 7.4: Relative calibration and self-calibration results for CNAO and TIFPA Δt_{means}. The numbers in parenthesis are the errors.

CNAO		
Parameter	**Relative**	**Self-calibration**
d1 (mm)	65.78 (0.33)	65.93 (0.01)
d2 (mm)	364.02 (0.42)	365.93 (0.01)
d3 (mm)	665.10 (0.46)	665.93 (0.01)
d4 (mm)	965.15 (0.49)	965.93 (0.01)
$offset$ (ps)	117 (3)	115 (1)

TIFPA		
Parameter	**Relative**	**Self-calibration**
d1 (mm)	271.78 (2.12)	269.86 (0.01)
d2 (mm)	671.14 (2.16)	669.86 (0.01)
d3 (mm)	972.09 (2.19)	969.86 (0.01)
$offset$ (ps)	-106 (13)	-98 (1)

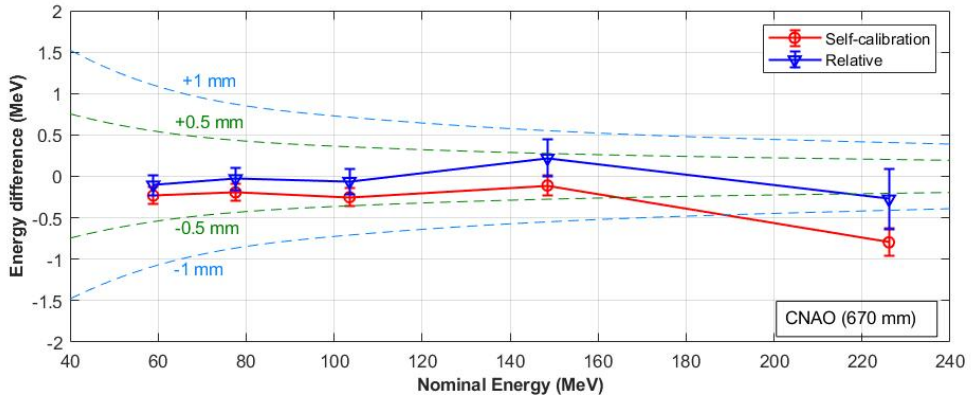

(a)

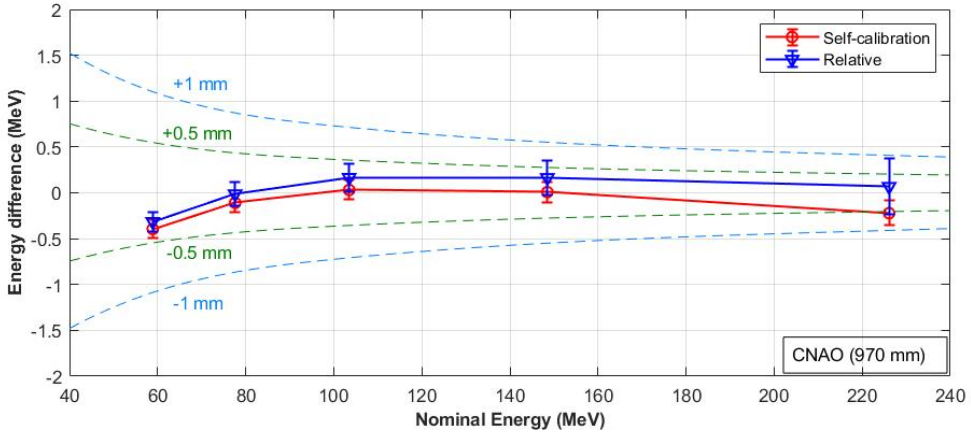

(b)

Fig. 7.7: *Comparison of the deviations between the CNAO nominal and the measured energies calculated using the Relative and self-calibration methods, for a sensor distance of 670 mm (a) and 970 mm (b). The dashed lines delimit the ranges difference between 0.5 mm and 1 mm.*

The calibration results were also evaluated by calculating the proton energy for the two largest distances used during the data acquisition (670 mm and 970 mm) and comparing them with the nominal energy values reported by the facilities.
Figures 7.7 and 7.8 show the energy difference of the nominal minus the calculated energy for the two largest distances, the two calibration methods, and the two proton therapy centers.

As shown in Figure 7.7, lines representing uncertainties of 0.5 mm and 1 mm of range in water were added to the graph. It is observed that the energies calculated for CNAO using the self-calibration results are slightly higher than those obtained with the relative calibration. However, this difference is reduced if the distance between sensors is increased, as shown by the comparison between Figures 7.7 a and 7.7 b. Additionally, it should be

noted that to obtain results within the allowed range uncertainty we must use the distance of 970 mm between the sensors.

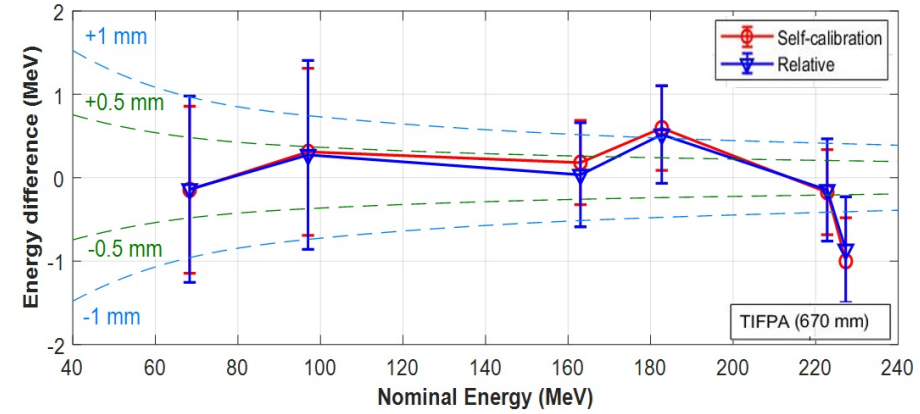

(a)

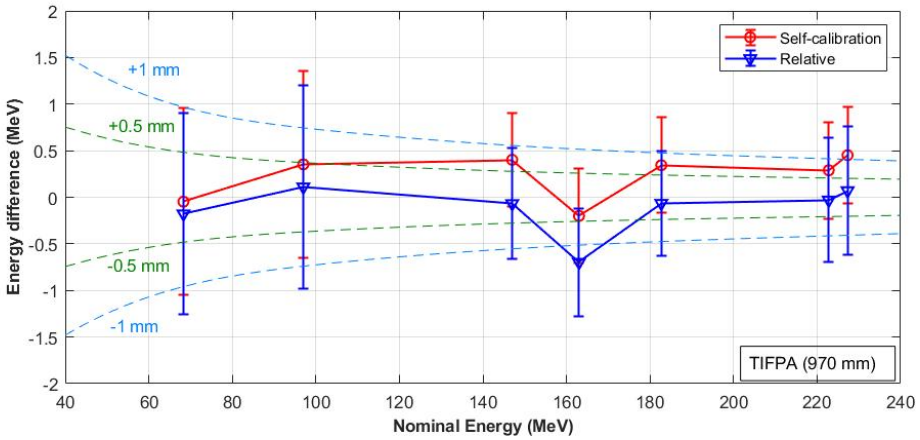

(b)

Fig. 7.8: *Comparison of the deviations between the TIFPA nominal and the measured energies calculated using the relative and self-calibration, for a sensor distance of 670 mm (a) and 970 mm (b). The dashed lines delimit a range difference of 0.5 mm and 1 mm respectively.*

In the case of TIFPA (Fig. 7.8), we have large error bars on the points. This was due to uncertainties in measuring the nominal energies using the Giraffe detector, with errors between 500 keV up to 1 MeV. In this case, the energy differences for the self-calibration were larger than for the relative approach due to the higher value of time $offset$. We should also note that only three positions were used to perform the self-calibration, while for CNAO four were used.

The studies done with simulations show that a decrease in the number of positions used for calibration worsens the determination of the $offset$ value. From figure 7.8, there are no

notable differences between the results with the relative and self-calibration methods, and the best results from the point of view of range uncertainties were found for the distance of 970 mm.

The main purpose of this part of present thesis was to propose and validate a calibration method for a TOF detector without having energies values to use as a reference. We determined using simulated data that the self-calibration approach could be a valid option to the relative calibration approach in cases where the nominal energies are not well known. The main limitation of the method is the need to know precisely the displacements between the second sensor distances used for the calibration, and the sensor must not suffer a change in its initial positioning. This condition can be fulfilled using a positioning system based on a computerized linear stage such as that shown in Fig.6.11. The studies carried out with computer simulations showed that using four positions and at least the minimum and maximum energies of the protons, it is possible to perform a precise and accurate calibration of the system.

Despite this, the method was applied to the two groups of experimental measurements previously carried out at CNAO and TIFPA. Those measurements were not specifically acquired to be used with the Self-calibration method, since the sensors were manually moved to each location, and systematic errors may have been introduced during the positioning. Additionally, the number of positions were different for each facility. However, the results show that the energy differences found permitted to be within the required limit of 1 millimeter of range uncertainty when the measurement is made at the largest distance between the sensors (970 mm).

The use of the large distance has the advantage of being able to estimate the time of flight with the lowest self-calibration uncertainties, but on the other hand, the number of coincidences between the sensor's peaks decreases drastically. This problem forces us to study the best system configuration depending on the desired application. For example, for a quality control system, the number of coincidences can be increased by raising the acquisition time. Another option would be to increase the proton flux being careful with the pile-up production that ends up reducing the efficiency of the system. An alternative solution can be to increase the digitizer acquisition efficiency limited actually to 0.4% (the effective acquisition time corresponds to the irradiation time acquired, stored and transmitted by the digitizer). Further studies will be necessary to increase the system efficiency to make it applicable for online proton energy measurements.

7.5 The beam test at CNAO using 8+8 strips configuration

The mean time difference Δt_{mean} measured with the procedure described in section 4.5 are shown in figure 7.9 for the three different beam energies and the two distances between the two sensors of the telescope used in the third CNAO test for 8+8 strips configuration.

Similar to the result from the first test at CNAO using pad sensors (Fig. 7.1), the slopes of the interpolation lines increase with decreasing energy, as they are proportional to the inverse of velocity. The intercepts of the interpolation lines provide the time $offset$ and proved to be independent of the energy, which is mainly induced by differences in the routing of signals.

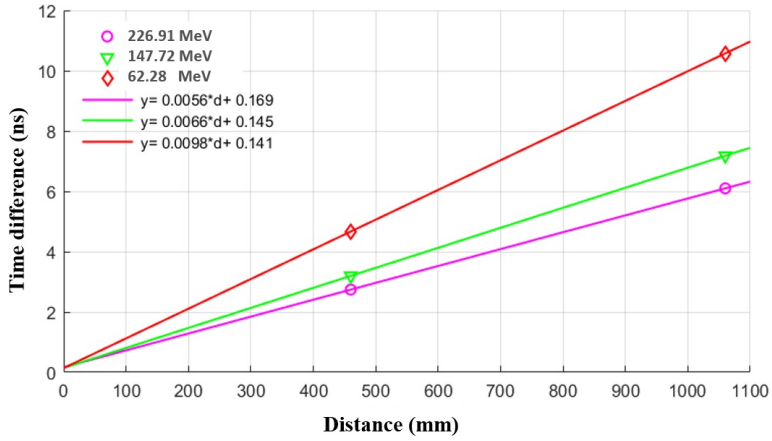

Fig. 7.9: *The measured mean time difference Δt_{mean} in the experimental measurement test in CNAO using the 8+8 strips configuration as function of distance for three proton beam energies (nominal values 62.28, 147.72, 226.91 MeV) and two distances between the two sensors (460 mm and 1060 mm).*

An example of signal analysis using MoVeIT tool from the data acquired in the experimental test conducted at CNAO using 8+8 strips configuration is shown in Figure 7.10. In this case the combination 32 cross was selected for analysis, the proton beam energy was 147.72 MeV and the S2 was located in 1060 mm distance from the S1. The maximum number of coincidences spread in the main diagonal of matrix and specially around the middle strips (Fig.7.10 a). The distribution of the time differences and related error are indicated in Fig. 7.10 b and 7.10 c. This configuration for strips combination was selected because of the digitizer acquisition problem (section 4.2).

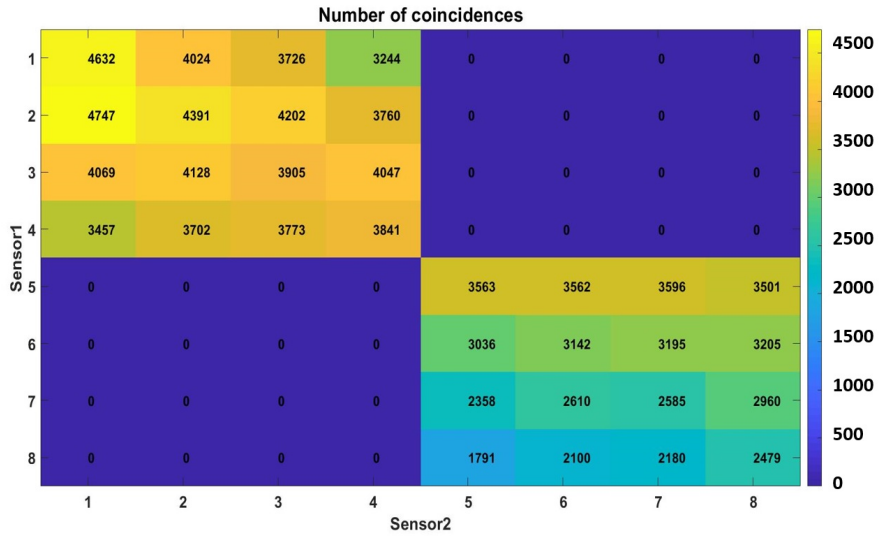

(a)

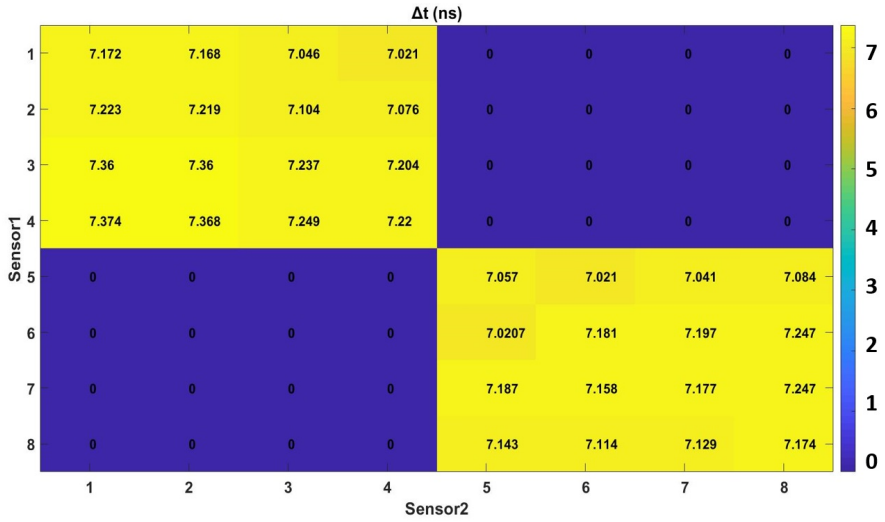

(b)

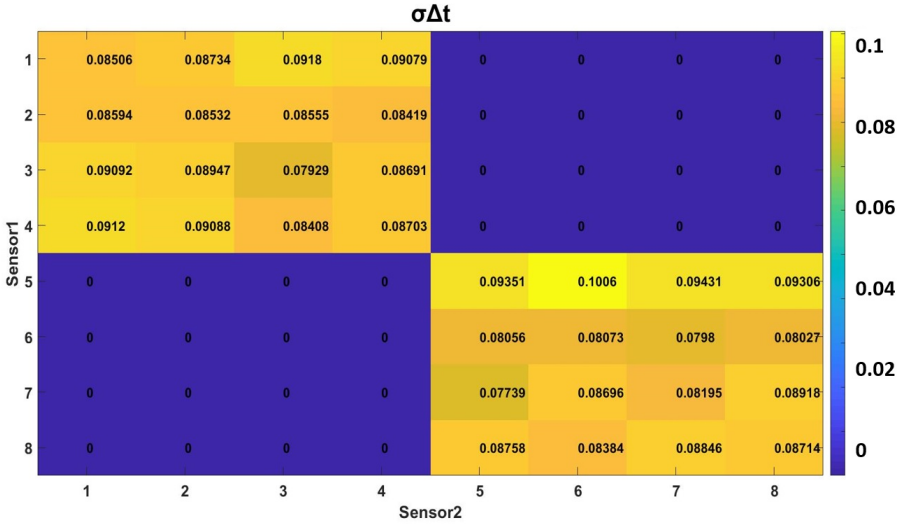

(c)

Fig. 7.10: *Example of the signal analyzing using MoVeIT tool from the data acquired in the experimental test conducted at CNAO, energy beam 147.72 MeV and distance 1060 mm. (a) distribution of the number of coincidences, (b) the time differences (ns), and (c) the related time differences error.*

The last test at CNAO was performed to evaluate the system efficiency and preliminary results using 8+8 strips configuration. Since the proton beam test was done just for two distances (460 mm and 1060 mm), the acquired data are not enough for applying the calibration methods. Hence, we have to examine more numbers of distances of detectors in our future studies.

Chapter summary

This chapter summarized results of proton beam energy measurement using UFSDs for proton beam tests at CNAO and TIFPA . The chapter also covered aspects of applying the absolute and self-calibration approaches for calibrating the system in terms of distance between two sensors and time offset. Additionally, the energy deviation using calibration methods in terms of range in water for both data from CNAO and TIFPA were compared. In the last section, the preliminary results using 8+8 strips combination were presented.

Chapter 8

Conclusions and future perspectives

> "We're doing a lot of research in proton therapy to change the way we deliver the beam."
>
> Harald Paganetti

This thesis is focused on the study of UFSD sensors for beam monitoring in charged particle therapy. The UFSDs are the innovative thin silicon detectors based on LGAD technology that allow for excellent time resolutions and very short signal duration, which are necessary to perform the measurement at the high fluxes of the particle beam.

The evaluation of the beam energy is one of the most important parameters in particle therapy. The small deviations of this quantity lead to deviations of the particle range, which could alter the dose distribution in the patient. Furthermore, the online measurement of the particle beam energy is a basic requirement for the development of new dose delivery techniques employing fast energy modulation systems for irradiating moving targets.

The measurement of the TOF as a well-known technique to determine the energy of particle can be performed independent of beam temporal structure. This method was never implemented to date for measuring the energy of a high-intensity clinical beam.

This work reports the results of tests performed at the Italian hadron therapy facilities (CNAO and TIFPA) using UFSD sensors to measures the TOF of protons to determine the beam energy. The work has been subdivided as follows.

The UFSDs characterizations were performed in the Laboratory of Innovative Silicon Sensors in the Physics Department of the University and INFN of Turin. The measurements

were performed with two setups: the probe station for investigating the electrical properties, and the Transient Current Technique Setup (TCT) to exploit the signal induced in the device by a pulsed laser. Based on the laboratory characterization, the most promising strip sensors were selected to test with therapeutic proton beams, to characterize their behavior in a realistic environment.

Measurements in CNAO and TIFPA were performed at different beam energies, covering the entire clinical energy range (60–230 MeV), and at four increasing distances from few centimeters up to 1 m. A model, considering the energy loss in the sensors and in the air, was developed and used to determine the beam energy at the isocenter from the measurements.

Numerous simulation studies were performed by developing a reconstruction and analysis tool, to evaluate the impact of different data-taking conditions, and the systematic effects on the measured TOF and beam energy. According to the results, generally, the largest error on the measured energy could be observed in case one strip combination due to the lowest system efficiency and number of coincidence signals. In addition, the protons scattered in S1 along the long distance will diverge in all the directions, making the efficiency less sensitive to the alignment. However, despite the clear decrease in the number of coincidences in the case 32 cross combination compared to 64, there was no significant difference in the amount and error of the measured energy. Thus, considering the delay between the two groups of channels in our digitizer, it is expected that acceptable results could be obtained using the 32 cross combination, which was confirmed by the results of the last beam test in CNAO.

Since the main source of uncertainties in the measured energies are distance and the time $offset$ between the readout channels, the system must be calibrated to determine these quantities experimentally. Relative calibration relies on the knowledge of the values of nominal energies, provided by the facilities. Its main limitation was the necessity of nominal energies estimation with high precision and accuracy. With the self-calibration method proposed in this work, it is possible to determine the proton energies within the required clinical accuracy (< 1 mm) without the need any external parameter to use as a reference.

The energies determined with the both calibration approaches were compared to the nominal values of CNAO and TIFPA. In the case of TIFPA, due to high uncertainties in measuring the nominal energies provided by the facility, the energy differences for the self-calibration were larger than for the relative approach due to the higher value of time $offset$. There were no notable differences between the results with the relative and

self-calibration methods, and the best results from the point of view of range uncertainties were found for the distance of 970 mm. It should also note that only three positions were used to perform the self-calibration, while for CNAO were used four. In case of CNAO, the self-calibration results were slightly higher than those obtained with the relative calibration. However, this difference was reduced if the distance between sensors was increased. Additionally, it was found that, for distances between sensors of 67 cm and 97 cm, both the deviations from the nominal values and the statistical errors on the measured quantities are of few hundreds of keV.

The results of this work demonstrated that using UFSD sensors, the clinical proton beam energy could be achieved with good accuracy in a few milliseconds and with a minimal perturbation of the beam. The main limitation of the self-calibration method is the need to know precisely the displacements between the second sensor distances used for the calibration, and the sensor must not suffer a change in its initial positioning. This condition can be fulfilled using a positioning system based on a computerized linear stage such as that shown in Figure 8.1, which was designed and produced in university of Turin and is ready to be used for the next beam test at hadron therapy center. Nonetheless, the simple system presented here, with upgraded positioning system to ease the calibration procedure, can find immediate application for the quality controls performed daily after regular maintenance of a clinical accelerator.

During the test at CNAO, six seconds of irradiation with protons at $5 \times 10^8 ps^{-1}$ intensity, were necessary to collect the required statistics to keep the maximum acceptable statistical error below the aforementioned tolerance. However, the system development should proceed towards the future goal of the energy measurement during treatment, ideally within the spot duration (ranging from tens of ms to hundreds of ms), and therefore a reduction of the irradiation time is needed to obtain the required accuracy is mandatory. It is worth noticing that the effective acquisition time used in the test is of 2–3 ms and that digitizer dead time ($\sim 600\mu s$) was the main bottleneck to set the needed irradiation time to collect the proper statistics. On the other side, UFSD3 sensors have been designed and produced and allow the simultaneous acquisition of several channels (thanks to a dedicated readout electronics under development), enlarging the sensitive area and, consequently, the statistics collection of coincident proton signals.

No degradation of sensor performances were recorded during the tests, studies dedicated to radiation hardness and reproducibility were not yet performed and will be investigated in the future.

We are far from the clinical implementation of this system because the efficiency of the system is very low. It means that TOF detectors measure only a small part of irradiation beam while the beam is changing fast. Moreover, we have to consider the time of processing and analyzing the acquired data (that now we are doing offline).

To implementing this method during the treatments, several improvements are required such as: increasing the area of the sensors, reducing the dead time of the acquisition system and correction algorithms for pile-up effects at therapeutic fluxes, which would considerably increase the complexity of the system.

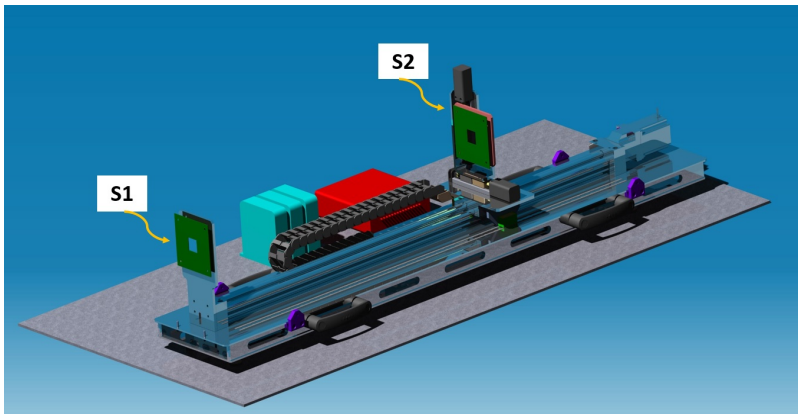

(a)

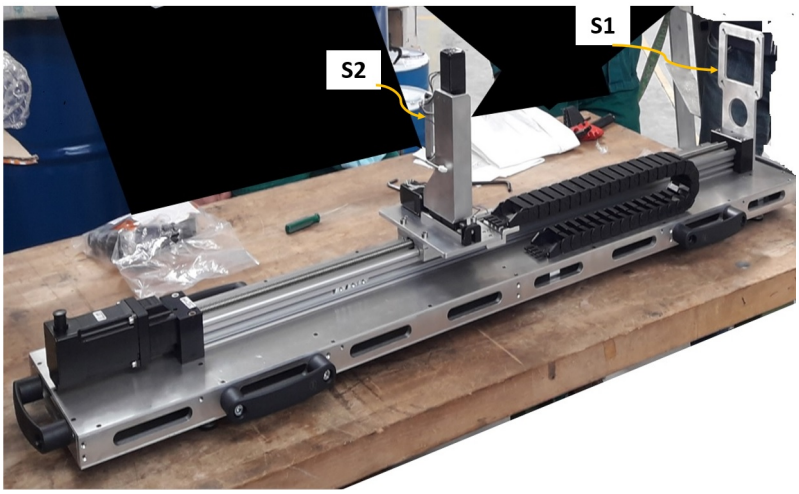

(b)

Fig. 8.1: *The future positioning system based on a computerized linear stage where the second sensor S2 is free to move from x_0 to x_n, designed and produced in University of Turin. (a) designed prototype, (b) produced prototype.*

References

[1] The European Federation of Organisations for Medical Physics Policy Statement Nr. 2, "The Roles, Responsibilities and Status of the Clinical Medical Physicist," 1984.

[2] S. Christofides et al., " Recommended Guidelines on National Schemes for Continuing Professional Development of Medical Physicists" , The European Federation of Organisations for Medical Physics Policy Statement No. 10.1, Physics Medica, vol. 23, no. 1, pp 7-11, 2016.

[3] https://www.flickr.com/photos/alfredoliverani/3011806205/in/set-72157607021899105/.

[4] https://www.ebay.com/itm/France-Henri-Becquerel-Cancer-Stamp-New-N-749-MNH-1946-B4-/143118500021.

[5] https://colnect.com/it/stamps/stamp/34395-Marie_Curie_1867-1934_Pierre_Curie_1859-1906-Centenario_della_scoperta_del_radio-Principato_di_Monaco.

[6] Robert R. Wilson, "Radiological Use of Fast Protons" , Radiology, vol. 47, no. 5, pp. 487–491, 1946.

[7] http://www.ptcog.ch/.

[8] Charlie Ma and Tony Lomax, "Proton and Carbon Ion Therapy," Edited by C.-M. , Taylor & Francis Group CRC Press, 2013.

[9] https://www.ptcog.ch/index.php.

[10] F. H. Attix, " Introduction To Radiological Physics and Radiation Dosimetry ", WILEY-VCH Verlag GmbH '& Co. KGaA, 2004.

[11] H. Paganetti, " Proton Therapy Physics ", Taylor & Francis Group CRC Press, 2011.

[12] W. R. Leo, "Techniques for Nuclear and Particle Physics Experiments", Springer, 1994 – Book.

[13] J. M. Verburg, "Reducing Range Uncertainty in Proton Therapy ", Department of Radiation Oncology, Harvard Medical School and Massachusetts General Hospital, Boston, MA, United States, 2015.

[14] U. Weber , G. Kraft, “Design and Construction of a Ripple Filter for a Smoothed Depth Dose Distribution”, Phys. Med. Biol. 44, , 2765-2775, 1999.

[15] E. Ford, “ Primer on Radiation Oncology Physics Video Tutorials with Textbook and Problems ”,ISBN 9781138591707 Published May 21, 2020 by CRC Press.

[16] A. Kaiser et al., “Proton Therapy Delivery and Its Clinical Application in Select Solid Tumor Malignancies”, J. Vis. Exp., vol. 144, no. e58372, pp. 1–12, 2019.

[17] S. Ahmed (Author), “Physics and Engineering of Radiation”, first edition, ISBN-9780120455812.

[18] T. Elsasser and M. Scholz. “Cluster effects within the local effect model”, Radiat Res, 167(3):319-329, Mar 2007.

[19] M. Scholz, A. M. Kellerer, W. Kraft-Weyrath er, and G. Kraft. “Computation of cell survival in heavy ion beams for therapy. The model and its approximation”, Radiat Environ Biophys , 36(1):59-66, Feb 1997.

[20] G. Laczko, V. Dangendorf, M. Kraemer, D. Schardt, K. Tittelmeier, “High Resolution Heavy Ion Track Structure Imaging”, Nucl.Instrum.Meth. , A535:216-220,2004.

[21] International Atomic Energy Agency and the International Commission on Radiation Unit, “Relative Biological Effectiveness in Ion Beam Therapy”, Technical report series no 461.

[22] P. Peschke, “Clinical Radiobiology, molecular and cellular basic”, ESTRO Course 2013 on “Radiotherapy with Protons and Ions”, Pavia, Italy.

[23] William T. Chu, “ Overview of Light-Ion Beam Therapy ” , Columbus-Ohio, ICRU-IAEA meeting, 18-20 March 2006.

[24] T. F. DeLaney, H. M. Kooy (editors), “Proton and Charged Particle Radiotherapy”, first edition (2007), ISBN: 9780781765527.

[25] https://www.ansto.gov.au/research/facilities/national-research-cyclotron.

[26] https://radiologykey.com/particle-accelerators/.

[27] http://webs.mn.catholic.edu.au/physics/emery/hsc_quanta_continued.htm.

[28] https://cerncourier.com/a/therapeutic-particles/.

[29] https://www.itnonline.com/article/introduction-current-radiation-therapy-treatment-planning-systems.

[30] T. Kanai, “Spot scanning system for proton radiotherapy,” Medical Physics, 7(4): p. 365, 1980.

[31] Belgian Health Care Knowledge Center Report 235, “Hadron therapy in children – an update of the scientific evidence for 15 paediatric cancers,” 2015.

[32] T. Haberer et al., “Magnetic scanning system for heavy ion therapy, ” Nuclear Instruments and Methods in Physics Research Section A: Accelerators, Spectrometers, Detectors and Associated Equipment, 330(1–2): p. 296-305, 1993.

[33] https://www.google.com/search?q=active+scanning+proton+therapy.

[34] S. Braibant et al., “ Particles and Fundamental Interactions: An Introduction to Particle Physics, Undergaduate Lecture Note in Physics ”, DOI 10.1007/978-94-007-2464-8 1, Springer Science+Business Media B. V.2012.

[35] M. Pullia, “Status report on the Centro Nazionale di Adroterapia Oncologica (CNAO),” EPAC 2008 - Contrib. to Proc., pp. 982–984, 2008.

[36] International Atomic Energy Agency, “Cyclotron Produced Radionuclides: Principles and Practice,” 2008.

[37] “ Advances in Particle Therapy : A Multidisciplinary Approach”, Edited by M. Dosanjih and J. Bernier, Taylor & Francis Group CRC Press, 2018.

[38] L. Badano, O. Ferrando, T. Klatka, et al. “Laboratory and in-beam tests of a novel real-time beam monitor for hadrontherapy,” IEEE Trans Nucl Sci, 52, p. 830, 2005.

[39] S. Braccini, G. Pitta, M. Donetti, et al. “MATRIX: an innovative pixel ionization chamber for on-line beam monitoring in hadrontherapy Advanced technology and particle physics,” World Scientific, p. 677, 2006.

[40] S. Braccini, “An innovative strip ionization chamber for on-line monitoring of hadron beams” Proceedings of the international conference of the Particle Therapy Co-Operative Group (PTCOG), Zurich, p. 44, 2006.

[41] S. Rana, G. Larson, Y. Zheng, “ Dosimetric impact of number of treatment fields in uniform scanning proton therapy planning of lung cancer,” Journal of Medical Physics, Vol. 39, No. 4, pp. 212-218, 2014.

[42] S. Giordanengo et al., “The CNAO dose delivery system for modulated scanning ion beam radiotherapy,” Med. Phys. vol. 42, no. 1, January, pp. 263-275, 2015.

[43] S. Giordanengo, “Design, implementation and test of the hardware and software for the Fast Control of the Dose Delivery System of Centro Nazionale di Adroterapia Oncologica (CNAO),” Tesi del Dottorato di Ricerca in Scienza ed Alta Tecnologia, XXII ciclo, Università degli Studi di Torino, a.a. 2007-2009.

[44] S. Giordanengo et al., “Design and characterization of the beam monitor detectors of the Italian National Center of Oncological Hadron-therapy (CNAO)”, Nucl. Instr. Meth. A 698 202-207 (2013).

[45] A. Ansarinejad et al., “The on-line detectors of the beam delivery system for Centro Nazionale di Adroterapia Oncologica (CNAO)” , Nuclear Physics B (Proc. Suppl.) 197 (2009) 185–189.

[46] T. Sothmann et al., "Real time tracking in liver SBRT: comparison of CyberKnife and Vero by planning structure-based γ-evaluation and dose-area-histograms," Phys. Med. Biol., 61(4), 2016.

[47] H. Paganetti, "Range uncertainties in proton therapy and the role of Monte Carlo simulations," Phys. Med. Biol., vol. 57, no. 11, 2012.

[48] http://physics.nist.gov/PhysRefData/Star/Text/PSTAR.html.

[49] M. Krim et al., "Method for range calculation based on empirical models of proton in liquid water: Validation study using Monte-Carlo method and ICRU data.," Int. J. Sci. Eng. Res., vol. 8, no. 3, pp. 728–735, 2017.

[50] ICRU 49. "Stopping Power and Ranges for Protons and Alpha Particles," Int Comm Radiat Units Meas Rep No 49. 1993.

[51] G.F. Knoll, " Radiation Detection and Measurement," Third Edition, John Wiley & Sons, New York, 2000.

[52] F. Hartmann, " Silicon tracking detectors in high energy physics," Nucl.Instr.Meth.A 666, pp. 25-46, 2012.

[53] https://i.stack.imgur.com/3u71Y.png.

[54] S. Vasile ; P. Gothoskar ; R. Farrell ; D. Sdrulla, " Photon detection with high gain avalanche photodiode arrays," IEEE Transactions on Nuclear Science, vol.45 (3), 1998.

[55] B. Dologoshein, "Silicon photomultipliers in particle physics: possibilities and limitations," The Science and Culture Series — PhysicsInnovative Detectors for Supercolliders, pp. 442-456, 2004.

[56] https://www.sense-pro.org/lll-sensor/sipm.

[57] S. Gundacker , A. Heering A. "The silicon photomultiplier: fundamentals and applications of a modern solid-state photon detector," Phys Med Biol ;vol. 65, no. 17:17TR01, 2020. doi: 10.1088/1361-6560/ab7b2d. PMID: 32109891.

[58] A. D. Guerra et al., "Advantages and pitfalls of the silicon photo multiplier(SiPM) as photo detector for the next generation of PET scanners," Nucl Inst Methods Phys Res A., vol. 17, 223–226 , 2010.

[59] Semiconductor Components Industries, LLC, " Introduction to the Silicon Photomultiplier (SiPM)," July, 2018-Rev. 7. www.onsemi.com.

[60] V. Sola et al., " A First FBK production of 50 μm ultra-fast silicon detectors ," Nucl Inst Methods Phys Res A. ,:360–8, 2019.

[61] N. Cartiglia, et al., " Design optimization of ultra-fast silicon detectors," NIM A, vol. 796, pp. 141-148, 2015.

[62] Cartiglia et al. " Beam test results of a 16 ps timing system based on ultra-fast silicon detectors ," Nucl.Instr.Meth. , A 850 , 83-88, 2017.

[63] H. F.-W. Sadrozinski, " Exploring charge multiplication for fast timing with silicon sensors," 20th RD50 Workshop, Bari, Italy, May 30 – June 1, 2012.

[64] https://www.hamamatsu.com/eu/en/index.html.

[65] F. Cenna et al., "TOFFEE: a full custom amplifier-comparator chip for timing applications with silicon detectors," Journal of Instrumentation, vol. 12, 2017.

[66] https://www.tifpa.infn.it/projects/move-it/.

[67] R. Padilla et al., "Effect of deep gain layer and Carbon infusion on LGAD radiation hardness," JINST vol.15, P10003, 2020.

[68] F. Carnesecchi, " Experimental study of the time resolution for particle detectors based on MRPC, SiPM and UFSD technologies ," Ph.D. thesis, Università di Bologna, 2018.

[69] Z. Galloway et al., "Properties of HPK UFSD after neutron irradiation up to 6e15 n/cm^2," NIMA, vol. 940, pp. 19-29, 2019.

[70] https://www.synopsys.com/silicon/tcad.html.

[71] M.Ferrero et al. " Developments in the FBK production of ultra-fast silicon detectors," In IEEE Nuclear Science Symposium and Medical Imaging Conference, 2017.

[72] O. Hammad Ali, " Characterization and test of LGAD strip silicon detectors to count the number of protons of therapeutic beams," Universita degli studi di Torino, PhD Thesis, 2020.

[73] https://www.keysight.com/en/pc-2111602/b1505a-power-device-analyzer-curve-tracer-series?nid=-32851.0.00&cc=IT&lc=ita&cmpid=zzfindb1505a.

[74] H.F.W. Sadrozinski, A. Seiden, N. Cartiglia, " 4-Dimensional Tracking with Ultra-Fast Silicon Detectors," Reports on Progress in Physics, Volume 81, Number 2, 2017.

[75] https://www.tek.com/keithley.

[76] https://www.ni.com/it-it/shop/labview/labview-details.html.

[77] W. Maes, K. De Meyer, R. Van Overstraeten, " Impact ionization in silicon: A review and update," Solid-State Electronics 33 (1999) 705–718.

[78] http://www.wafer2chip.com/.

[79] https://cividec.at/electronics-C2-HV.html.

[80] M.Garcia et al, " The Transient Current Technique: laser characterization of silicon detectors," CERN DT training seminar, CERN, 2017.

[81] https://www.nktphotonics.com/lasers-fibers/product/pilas-picosecond-pulsed-diode-lasers/.

[82] M. Ferrero et al., " Radiation resistant LGAD design," Nuclear Inst. and Methods in Physics Research, A vol.919, p:16–26, 2019.

[83] Y. Zhao et al., " Comparison of 35 and 50 μm thin HPK UFSD after neutron irradiation up to $610^{15} neq/cm^2$," Nuclear Instruments and Methods in Physics, Vol.92, Pages 387-393, 2019.

[84] M. Ferrero et al., "Developments in the FBK Production of Ultra -Fast Silicon Detectors," 2017 IEEE Nuclear Science Symposium and Medical Imaging Conference (NSS/MIC), Atlanta, GA, 2017, pp. 1-5, doi: 10.1109/NSS-MIC.2017.8533035.

[85] M.Ferrero "Development of Ultra Fast Silicon Detector for tracking in 4 dimensions," Universita degli studi di Torino, Physics department, Ph.D. thesis, 2020.

[86] S. Rossi, "The status of CNAO," Eur. Phys. J. Plus, vol. 126, no. 8, pp. 1–39, 2011.

[87] A. Mirandola et al., " Dosimetric commissioning and quality assurance of scanned ion beams at the Italian National Center for Oncological Hadrontherapy," Med Phys. vol. 42, no. 9, pp. 5287–300, 2015.

[88] S. Rossi, " The National Centre for Oncological Hadrontherapy (CNAO): Status and perspectives," Physica Medica vol.31, pp. 333-351, 2015.

[89] https://protonterapia.provincia.tn.it/.

[90] https://iba-worldwide.com/.

[91] F. Tommasino et al., " Proton beam characterization in the experimental room of the Trento Proton Therapy facility," Nuclear Inst. and Methods in Physics Research, A, vol. 869, pp. 15-20, 2015.

[92] F. Tommasino, " Experimental Cave at Trento CPT: status update," RDH/IRPT meeting, Rome, Feb 2016.

[93] DT1470ET - CAEN - Tools for Discovery [Internet]. [cited 2020 Aug 14]. Available from: https://www.caen.it/products/dt1470et/.

[94] CIVIDEC Instrumentation - CVD Diamond Technology applications [Internet]. [cited 2020 Aug 14]. Available from: https://cividec.at/electronics-C2.html.

[95] DT5742 - CAEN - Tools for Discovery [Internet]. [cited 2020 Aug 14]. Available from: https://www.caen.it/products/dt5742/.

[96] https://www.caen.it/products/a2818/.

[97] https://www.caen.it/products/caen-wavedump/.

[98] https://physics.nist.gov/PhysRefData/Star/Text/PSTAR.html.

[99] J. Jokinen, J. Keinonen, P. Tikkanen, A. Kuronen, T. Ahlgren, and K. Nordlund, "Comparison of TOF-ERDA and nuclear resonance reaction techniques for range profile measurements of keV energy implants," Nucl. Instruments Methods Phys. Res. Sect. B Beam Interact. with Mater. Atoms, vol. 119, no. 4, pp. 533–542, 1996.

[100] W. A. Worstell et al., "First results developing time-of-flight proton radiography for proton therapy applications," Proc. SPIE 10948, Med. Imaging 2019 Phys. Med. Imaging, vol. 109480, no. March, p. 2511804, 2019.

[101] A. Airapetian et al., "The time-of-flight technique for the HERMES experiment," Nucl. Instruments Methods Phys. Res. Sect. A Accel. Spectrometers, Detect. Assoc. Equip., vol. 540, no. 2–3, pp. 305–310, 2005.

[102] Robert F. Pfaff, J. E. Borovsky, and david T. Young, " Measurement Techniques in Space Plasmas_ Particles," the American Geophysical Union, 1998.

[103] A. Rizzo et al., "A compact Time of flight detector for space applications : The LIDAL system," Nucl. Inst. Methiods Phys. Res., vol. 898, no. November 2017, pp. 98-104, 2018.

[104] A. Vignati et al., "Innovative thin silicon detectors for monitoring of therapeutic proton beams: Preliminary beam tests," J. Instrum., vol. 12, no. 12, 2017.

[105] https://www.mathworks.com/products/matlab.html.

[106] S. Giordanengo et al. , " Clinical performance of the dose delivery system at the Italian national center for oncological hadrontherapy," Romanian Reports in Physics, Vol. 66, No. 1, P. 30–38, 2014.

[107] A. Vignati et al. "A new detector for the beam energy measurement in proton therapy: a feasibility study ," Phys. Med. Biol, vol.65, Nov. 2020, DOI: 10.1088/1361-6560/abab58.

[108] H. M. Tawfeek et al., "Investigations into the Proton Stopping Power of Human Body," J. Chem. Biol. Phys. Sci., vol. 5, no. 4, pp. 4345–4354, 2015.

[109] S. Agostinelli et al., "GEANT4 - A simulation toolkit," Nucl. Instruments Methods Phys. Res. Sect. A Accel. Spectrometers, Detect. Assoc. Equip., vol. 506, no. 3, pp. 250–303, 2003.

[110] F. Cenna et al., "Weightfield2: A fast simulator for silicon and diamond solid state detector," Nucl. Instruments Methods Phys. Res. Sect. A Accel. Spectrometers, Detect. Assoc. Equip., vol. 796, no. October, pp. 149–153, 2015.

[111] http://personalpages.to.infn.it/ cartigli/Weightfield2/Main.html.

[112] F. Cenna, et al., Weightfield2: " a fast simulator for silicon and diamond solid state detector," NIM A 796, 149-153, 2015.

[113] T. Bortfeld. "An analytical approximation of the Bragg curve for therapeutic proton beams," Med Phys. 1997;24(12):2024–33.

[114] BS. Ishkhanov . The atomic nucleus. Moscow Univ Phys Bull, 67(1):1–24, 2012.